# An Investigation of Magnetic Storm Effects on Total Electron Content over South Africa for Selected Periods in Solar Cycles 23 and 24

by

**Valentino Patrick van de Heyde**

A thesis submitted in partial fulfillment of the requirements of the degree of Magister Scientiae in the Department of Physics, University of the Western Cape



**Supervisor:** Prof. C.P. Price, Department of Physics, University of Alaska Fairbanks (UAF)

**Supervisor:** Dr. D. M. Moeketsi, Centre of High Performance Computing (CHPC), Council for Scientific Industrial Research (CSIR)

**Co-Supervisor:** Prof. R. Lindsay, Department of Physics, University of the Western Cape (UWC)

**December 2012**

# Abstract

## An Investigation of Magnetic Storm Effects on Total Electron Content over South Africa for Selected Periods in Solar Cycles 23 and 24

**Valentino Patrick van de Heyde**

**MSc Thesis, Department of Physics, University of the Western Cape,**

**Private Bag X17, Bellville, 7535**

The development of regional ionospheric Total Electron Content (TEC) models has contributed to understanding the behavior of ionospheric parameters and the coupling of the ionosphere to space weather activities on both local and global scales. In the past several decades, the International Global Navigation Satellite Systems Service (GNSS) networks of dual frequency receiver data have been applied to develop global and regional models of ionospheric TEC. These models were mainly developed in the Northern Hemisphere where there are dense network of ground based GPS receivers for regional data coverage. Such efforts have been historically rare over the African region, and have only recently begun. This thesis reports the investigation of the effect of mid-latitude magnetic storms on TEC over South Africa for portions of Solar Cycles 23 and 24. The MAGIC package was used to estimate TEC over South Africa during Post Solar Maximum, Solar Minimum, and Post Solar Minimum periods. It is found that TEC is largely determined by the diurnal cycle of solar forcing and subsequent relaxation, but effects due to storms can be determined.



**December 2012**

# Keywords

**An Investigation of Magnetic Storm Effects on Total Electron Content over South Africa for Selected Periods in Solar Cycles 23 and 24**

By

**Valentino Patrick van de Heyde**

Solar Activity

Geomagnetic Storms

Ionosphere

Total Electron Content

Global Navigation Satellite Systems

MAGIC

Global Positioning Systems

Disturbance Storm Time

# Author's Declaration

I, Valentino Patrick van de Heyde, declare that

# "An Investigation of Magnetic Storm Effects on Total Electron Content over South Africa for Selected Periods in Solar Cycles 23 and 24"

is my own original work, and that I have not previously in its entirety or in part submitted it at any university for a degree, and that all the sources I have used or quoted have been indicated and acknowledged by means of complete references.



**Valentino Patrick van de Heyde** **Date: December 2012**

# Acknowledgements

Firstly, I would like to thank the Almighty above our God, Lord and Savior Jesus Christ, who has given me the strength, determination and will power each step of the way of this research study.

I am thankful to the following organizations and individuals (not in any particular order), for without their guidance, assistance, advice, friendship and motivation this Masters Thesis would have been near impossible to complete.

- My supervisor, Prof. Channon Price of the Physics Department of University of Alaska, Fairbanks (UAF), for coming to my rescue in my time of need, for your constant guidance, support and motivation, your efforts is truly appreciated.

- My supervisor, Dr. Daniel Moeketsi of the Centre of High Performance Computing (CHPC), CSIR for motivation, support and introducing me into the world of space weather physics research.

- My co-supervisor, Prof. Robert Lindsay, of the Department of Physics, University of the Western Cape (UWC), co-supervisor of this research study, your guidance, fruitful discussions and encouragements is much appreciated.

- To, Dr. Eduardo Pradere of the NOAA Space Weather Prediction Centre, USA, for discussions and guidance, but most importantly granting the MAGIC application for academic research use.

- The National Research Foundation (NRF) & Inkaba yeAfrica project for their continuous financial support.

- The UWC Physics Department Staff (Academic and Technical) for giving me the academic foundation, an office and access to the internet to pursue a research project.

- The International Centre of Theoretical Physics (ICTP) for my acceptance into the 2nd Satellite Navigation Science and Technology Workshop in Trieste, Italy from 6-23 April 2010.

- To Trignet (Mowbray, Cape Town) for the GPS data.

***Very special thanks to the following:***

Firstly I would like to give a special thanks to My Rock and the Love of my Life, Jenne-Lee, thank you for your continuous support, motivation, prayers and unconditional love during this research study, and always putting a smile on my face.

To my colleague and friend, Mornay van Rooyen, for your constant motivation, support and prayers.

To my (late) father and mother, Josef and Denise van de Heyde, thank you for your support, love, financial assistance during undergraduate studies and shaping me into the person I am today.

To my brother, Lorenzo van de Heyde, Thank you for showing an interest in my research.

My UWC friends and colleagues (Natasha, Lyndlle, Carmen, Angela, Clive, Razia, Abdul, Nazley, Joash, Prof. Arendse and Dr. Muller) thank you for your support and discussions.

My friends Sadick, Leon and Graeme thank you for your motivation and support.

To Petrus and Natasha November for your support and keeping me in your prayers, much appreciated.

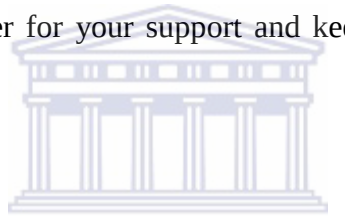

# Dedication

This thesis is devoted in caring and loving memory to my late Father and Hero

**Joseph Johannes van de Heyde**
**(04 July 1960 - 18 November 2011)**

and grandmother

**Minnie Jaftha**
**(08 July 1939 - 18 August 2008)**

and to the joy of my life, my son

**Sashton Valentino van de Heyde**
**(03 December 2009)**

**Table of Contents**

# LIST OF ACRONYMS

| | |
|---|---|
| ΔTEC | Difference TEC Time Series |
| CME | Coronal Mass Ejections |
| CONUS | Continental US |
| CORS | Continuously Operating Reference Stations |
| CSIR | Council for Scientific and Industrial Research |
| Dst | Disturbance Storm Time |
| DoD | (US) Department of Defence |
| EM | Electromagnetic |
| ESA | European Space Agency |
| EU | European Union |
| EUV | Extreme Ultraviolet |
| FORTE | Fast Onboard Recording of Transient Events |
| GAIM | Global Assimilation of Ionospheric Measurements |
| GNSS | Global Navigation Satellite Systems |
| GLONASS | Global Orbiting Navigation Satellite System |
| GPS | Global Positioning System |
| GSD | Global Systems Division |
| HartRAO | Hartebeesthoek Radio Astronomy Observatory |
| HF | High Frequency |
| IEA | Ionospheric Equatorial Anomalies |
| IGS | International GNSS Service |
| IRI | International Reference Ionosphere |
| IMF | Interplanetary Magnetic Field |

| | |
|---|---|
| IOC | Initial Operational Capability |
| IOV | In-Orbit Validation |
| Kp | Planetarische Kennziffer |
| LEO | Low Earth Orbits |
| MIDAS | Multi-Instrument Data Analysis System |
| MCS | Master Control Station |
| MEO | Medium Earth Orbits |
| NGDC | (US) National Geophysical Data Center |
| NGS | (US) National Geodetic Survey |
| NNs | Neural Networks |
| NOAA | (US) National Oceanic and Atmospheric Administration |
| OCS | Operational Control System |
| RINEX | Receiver Independent Exchange Format |
| RMS | Root Mean Square |
| RTEC | TEC Reference Time Series |
| SABIM | South African Bottomside Ionospheric Model |
| SADC | Southern African Development Community |
| SAST | South Africa Standard Time |
| SWPC | (US) Space Weather Prediction Centre |
| SPS | Standard Positioning Service |
| TEC | Total Electron Content |
| TECU | TEC Units |
| US | United States of America |
| UT | Universal Time |
| UNB-IMT | University of New Brunswick Ionospheric Modelling Technique |

| | |
|---|---|
| UTC | Coordinated Universal Time |

# LIST OF FIGURES

# LIST OF TABLES

# Chapter 1

# INTRODUCTION

## 1.1 Background Research

One of the first studies of the ionospheric parameter called Total Electron Content (TEC) was conducted with the use of geostationary radio beacon satellites employing the Faraday rotation technique (Garriot, et al., 1960; Titheridge, 1973; Davies, 1980). These TEC measurements were mostly obtained from either a single frequency or a ground based network of instruments, e.g. ionosondes. Subsequently, with the decline of the extraordinary experiments on the Faraday satellites, the arrival of the Global Navigation Satellite Systems (GNSS) such as the United States (US) Global Positioning System (GPS) in the last 30 years, has provided a unique opportunity for the science community to study the spatial and temporal characteristic behaviour of the ionosphere (Schaer, 1999; Yizengaw, et al., 2005, etc.) among other applications, such as commercial and defence usage. Numerous research studies have gone into ionospheric research and have proven that the use of the dual frequency L1 (1575.42 MHz) and L2 (1227.60 MHz) signals transmitted by the GNSS and received by the network of GPS receivers distributed worldwide and locally provides an exceptional opportunity to determine higher resolution spatiotemporal ionospheric TEC at a local and worldwide level (Klobuchar, 1991; Jakowski, 1996; Komjathy, 1997; Mannucci, et al., 1998; Schaer, 1999; Meggs, et al., 2004). These ionospheric studies, especially the modelling of TEC, play a big role in understanding how electromagnetic (EM) waves propagate from the satellites in space to the receivers on the ground. As EM waves (for example, GPS signals) move through the ionosphere from space, they experience time delays and phase advances due to the interaction with free electron gas, and in general the net effect of the signal delay is directly proportional to the integrated free-electron density (TEC) along the signal path and inversely proportional to the square of the frequency of propagation (Misra and Enge, 2006). So with the help of GNSS the ionosphere can be studied to effectively provide corrections for single frequency navigation, surveillance and communication systems.

The magnitude of TEC is very variable and depends on numerous factors such as local time of studied area, geographical location, season and solar activity cycle of the Sun (Jakowski, et al., 1999; Fedrizzi, et al., 2001). Studies conducted about a decade ago (Jakowski, et al., 2001, 2002) illustrate that TEC observation with the use of GNSS can add to space weather monitoring. The latter mentioned studies were primarily conducted using a densely distributed GPS data network in the Northern Hemisphere. However, studies over any African regions are still rare.

Ionospheric studies over South Africa have been ongoing for more than sixty years, starting after World War II, with ionosonde installations in Cape Town, Johannesburg and Grahamstown (Hewitt, et al., 1947; Wadley, 1949). In the 1960's another instrument, named the Relative Ionospheric Opacity meter plus the Antarctic-based Southern Hemisphere Dual Array Network presented scientists with further opportunities for ionospheric research over South Africa. A more detailed description on local TEC research over South Africa is discussed in Chapter 3.



## 1.2 Aim of the Project

The main aim of this thesis is to investigate the effect of mid-latitude magnetic storms on TEC over South Africa for portions of Solar Cycles 23 and 24. The latter will be done with the use of a package called MAGIC which converts GPS data into maps of TEC. Subsequently, the ionospheric TEC maps which show the spatiotemporal representations of TEC over South Africa are analyzed.

## 1.3 Thesis Overview

This thesis is divided into five chapters and the overview is as follows:

**Chapter 1** consists of the thesis research description, followed by a statement of the intention of the project and ends of with an overview of thesis.

**Chapter 2** comprises the theoretical background of the Sun, the solar cycle, the Earth's ionosphere and its structures, and the theory of propagation and effects of EM waves such as

GNSS signals. These topics outline the basis for this work. In addition, important satellite missions such as the GNSS constellations, which consist of US GPS, GLONASS, COMPASS and GALILEO, are briefly discussed as related to this work.

**Chapter 3** is devoted to the description of the local and global ionospheric modelling techniques using GNSS used locally and abroad, MAGIC ionospheric modelling, Kalman Filtering Assimilation technique, the physics behind MAGIC based on the propagation of radio waves in the ionosphere, and finally a concise discussion on MAGIC for TEC calculation and GNSS networks over South Africa.

**Chapter 4** of the thesis focuses on the discussions of the observations of TEC patterns during Post Solar Maximum, Solar Minimum, and Post Solar Minimum periods over South Africa as estimated by the MAGIC package.

**Chapter 5** includes a final discussion and summary off the research study as well as proposed future work using MAGIC as a package or research tool.

# Chapter 2

# THE SUN, EARTH IONOSPHERE AND GNSS

## 2.1 Introduction

In this chapter the focus will be on the theoretical background of the Sun, the solar cycle, the Earth's ionosphere and its structures, and the theory of propagation and effects of EM waves such as GNSS signals. These topics outline the basis for this work. In addition, important satellite missions such as the GNSS constellations, which consist of US GPS, GLONASS, COMPASS and GALILEO, are briefly discussed as related to this work.

## 2.2 The Sun, solar cycle and Earth's magnetic field



In the Milky Way galaxy, the Sun is one of roughly one billion stars; there is an average distance of 1AU (1AU = $1.49 \times 10^8$ km) between Earth and the Sun, which is planet Earth's nearest star. The Sun's radius is approximately 0.005 AU and it is completely made up of gas (92.1% Hydrogen, 7.8 % Helium and minute percentages of other light elements (Moldwin, 2008). Its rotation period is about 27 days, but since the Sun is a gaseous body rather than a solid body, diverse portions of the Sun rotate at dissimilar rates. The rotation rates decrease with latitudinal displacement from the equator; there is a differential rotation period of ~ 25 days at the equator and ~ 31 days at the polar regions (Schunk and Nagy, 2009). The solar structure of the Sun comprises of several layers, namely the interior which entails the core, radiative layer and convection layer, and the atmosphere that consists of the photosphere, chromosphere and corona.

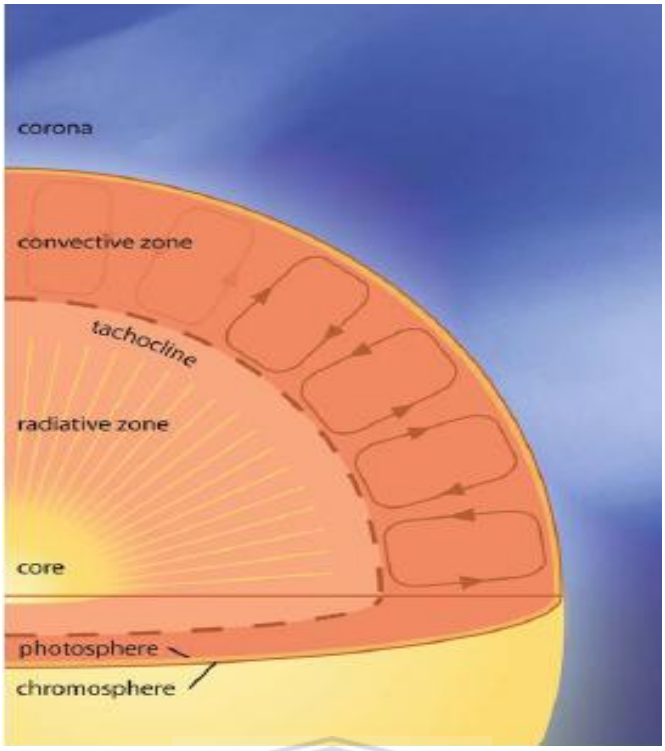


**Figure 2.1:** The Solar structure (from Vita-Finzi, 2008).

A graphical representation of the Sun's solar structure can be viewed in Figure 2.1. The visible solar dark spots of rough circular shape on the surface of the photosphere that is cooler than their surroundings are called sunspots (Vita-Finzi, 2008; Lang, 2009). Sunspots continuously change positions and are regions of intense magnetic fields on the photosphere of the Sun. The total number of sunspots varies during the Sun's quasi-periodic cycle (the "solar cycle") of ~ 11 years. The solar cycle is the periodic change in the Sun's activity (includes changes in the levels of solar radiation) and appearance (visible changes in the number of sunspots and other visible appearances). For this study, the time periods used for Solar Cycles 23 and 24 can be viewed in Table 4.2 of thesis. Several solar observatories have observed and kept daily records of the number of sunspots on the Sun since the 1800's (Moldwin, 2008).

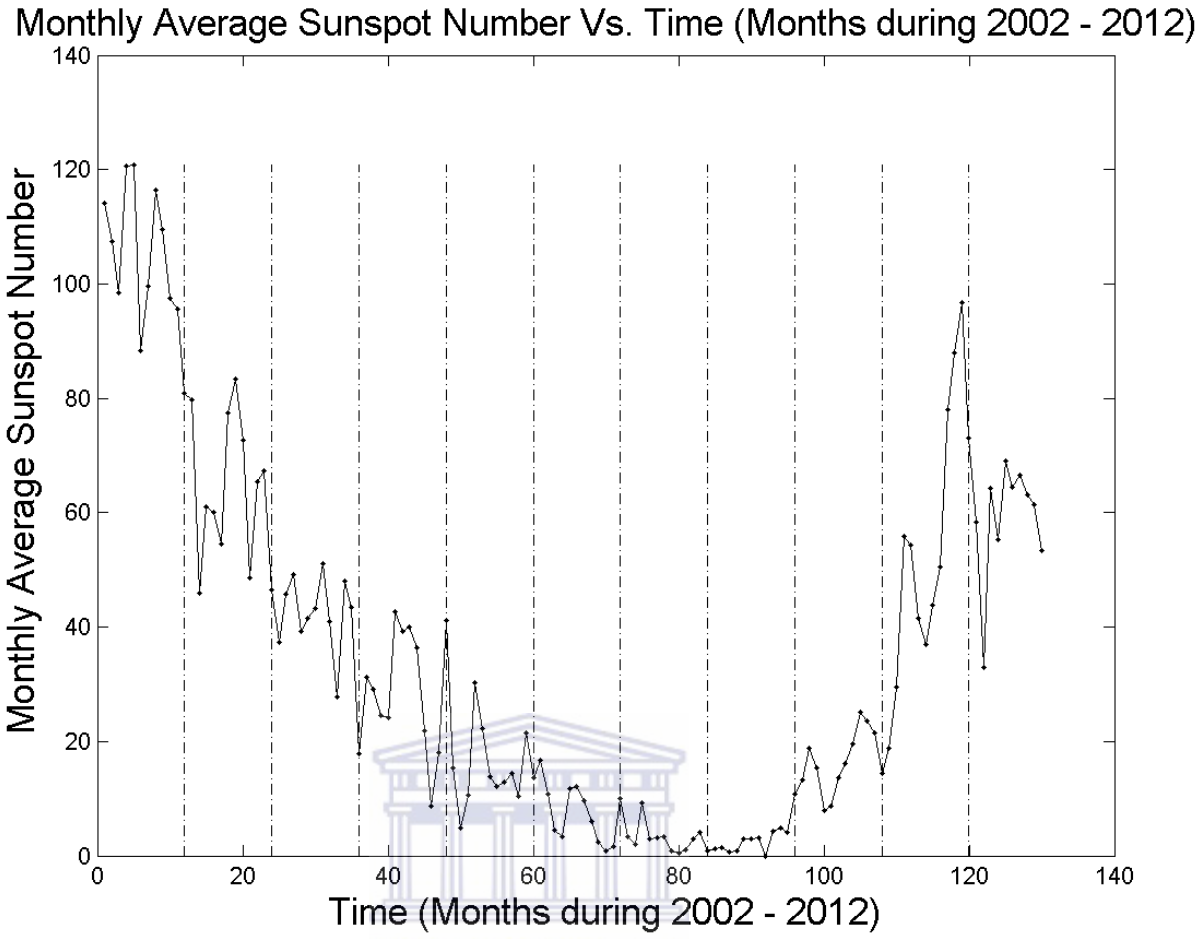


**Figure 2.2:** Graph of Monthly Average Sunspot Number from 2002 up to October 2012 (data sourced from www.ngdc.noaa.gov). The dash line marker represents a year.

In Figure 2.2, it is shown that the monthly sunspot data recorded from 2002 up until October 2012. The pattern of the quasi-periodic, typically 11 year duration solar cycle begins with a period of fewer and smaller sunspots (the "solar minimum"), followed by a period of more and larger sunspots called (the "solar maximum"), and back to the solar minimum (Lang, 2009).

The Sun loses mass by constantly emitting corpuscular (minute particle) radiation, in the form of charged atoms and sub-atomic particles, known as plasma, from the corona (Moldwin, 2008). The plasmatic atmosphere of the Sun constantly blows away from its surface to maintain equilibrium (Parker, 1958; 1963). This occurs because coronal particles have temperatures over 1 million degrees Kelvin, and thus have velocities great enough to escape the Sun's gravitational pull (Moldwin, 2008). These escaping energetic particles (protons, electrons and heavier ionized elements), termed the solar wind, allow the corona to

expand into space (Parker, 1958; 1963, Biermann, 1961). The solar wind expands radially, moves supersonically away from the Sun and extends distantly into interplanetary space as a large, teardrop-shaped cavity, termed the heliosphere. The charged particles in the solar wind are flux-trapped, and their inertia carries away some of the Sun's magnetic field, which becomes the interplanetary magnetic field (IMF). The direct interaction between the IMF and the Earth's magnetosphere results in the dayside cusp or cleft. It is normally in the range of 2° to 4° wide and situated at the geomagnetic latitude 78° to 80°, close to local noon. The phenomenon is characterized by an enhancement in electron densities at all altitudes.

The radial movement of the solar wind against the Earth's magnetic field leads to the creation of a large magnetic plasma region surrounding Earth, called the magnetosphere (Walker, 1989; Otto, 2005; Vita-Finzi, 2008; Moldwin, 2008). Since the solar wind is moving supersonically, a shock wave is formed around the magnetosphere, called a bow shock, where the solar wind slows down to subsonic speeds. The dayside portion of the magnetosphere is compressed, and subsequently the solar wind flow is diverted around the magnetosphere, generates the Earth's magnetotail.

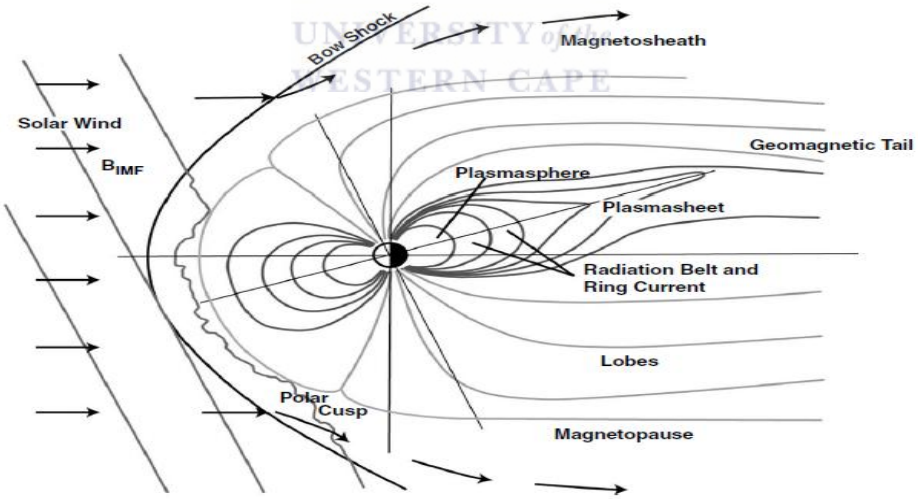


**Figure 2.3:** A cross section of the Earth's magnetosphere with North on top and the Sun on the left, showing how the solar wind interacts with the magnetosphere (from Moldwin, 2008).

The latter description of the magnetosphere is depicted in Figure 2.3. The Earth's magnetic field is a key factor in the formation of the ionized region of the upper atmosphere, which will be discussed in the next section. It is useful to use geomagnetic coordinates (latitude and longitude) to illustrate and model the ionized upper atmospheric region (Komjathy, 1997). A first approximation of the Earth's magnetic field is that of a uniformly magnetized sphere.

The orientation of the dipole is defined by an axis, and the two positions where the axis of the dipole best fits the geomagnetic field cross the Earth's surface at a point known as (the) austral (south) and boreal (north) dipoles (North and South geomagnetic poles). The intersection of the plane through the Earth's centre that is perpendicular to the dipole axis and the Earth's surface is called the geomagnetic equator. The dip latitude (measured from the geomagnetic equator) is frequently used to portray the Earth's magnetic field. In discussing this topic, the poles are referred to as dip poles, i.e. locations where the geomagnetic field is vertical to the Earth surface, and the dip equator is where the geomagnetic field is horizontal. The reader is referred to Tascione (1988), McNamara (1994), and Davies (1990) for a more in depth discussion of the Earth's magnetic field, and relationships between geographic, geomagnetic and dips latitudes.

## 2.3 The Earth's Ionosphere

### 2.3.1 The Ionosphere

The Earth's atmosphere has five layers, and one of these layers is a partially-ionized region in the upper atmosphere, called the ionosphere, which is found from approximately 60 km above the surface of the Earth, after the neutral atmosphere layer, to approximately 1000 km (Fernandez, 2004). It was first called the Kennelly-Heavyside layer, the upper conducting ionized layer and the ionized upper atmosphere (Hunsucker and Hargreaves, 2003). The term ionosphere was first proposed by Sir Robert Watson-Watt in a letter addressed to the United Kingdom Radio Research Board, but only appeared in the literature in 1929 (Shunk and Nagy, 2009). It was only in the period 1932-1934 when Watson-Watt, Appleton, Ratcliffe and other researchers used the term extensively in articles and books, having been used by Watson-Watt for several years prior to that (Komjathy, 1997; Hunsucker and Hargreaves, 2003). This region is in reality not a layer, but an electrified region within the Earth's upper atmosphere, where great concentrations of ions and free electron gas are found in abundance (Ahrens, 2008).

At approximately 1000 km above the Earth's surface, the partially-ionized region ends and the region called plasmasphere (or protonsphere) starts. The electron density distributions in the ionosphere and plasmasphere are variable, and thus the border between the two layers is

not clearly defined, being dependent on period of day, season and solar activity (Goodman, 2005). In this region the density of the neutral atoms is small and the positive ions are mainly protons, thus the terminology "protonsphere". The plasmasphere decays out at an altitude between 30,000-40,000 km above the Earth surface to a boundary between itself and the interplanetary plasma called the plasmapause (Komjathy, 1997; Moeketsi, 2007a). Electron densities of the plasmasphere thus drop drastically by an order of 1-2 magnitudes (Davies, 1990).

The formation of the major part of the ionosphere is mainly due to the interaction of solar EM radiation (solar EUV and X-ray intensity) with neutral atmospheric constituents (Davies, 1990; Goodman, 2005; Hanslmeier, 2007; Kelley, 2009), and so the peak electron densities in the ionosphere are found on the dayside. An additional contributor to the creation of the ionosphere is cosmic radiation, but to a less important degree. In the Earth's upper atmosphere, energetic photons incident from the sun interact with the neutral constituents (atoms and molecules), stripping negatively charged electrons from neutral atoms to form positively charged ions. The process described above is called *photoionization* (Cravens, 1997; Parks, 2004) and the reaction can be symbolized as



$$h\nu + M \rightarrow M^{+} + e^{-}$$

where $h\nu$ represents a quantum of energy ($h$ is Planck's constant = $6.62X10^{-34} Joules.\sec$ and $\nu$ is the frequency), $M$ is an atom or molecule and $e^{-}$ an electron.

The counteracting process of photoionization is called *recombination*, when ions and electrons combine to form neutral atoms. There are two types of recombination processes involved, namely radiative recombination and dissociative recombination (Kelley, 2009).

In the radiative recombination process the electrons unite directly with ions, changing them into neutral atoms. The emission of a photon is required to conserve energy and momentum,

$$O^{+} + e^{-} \rightarrow O + photon.$$

The dissociative recombination process consists of two phases. In the first phase, positive ions (e.g. $N^+$) interact with neutral molecules (e.g. $O_2$), replacing one of the atoms in the molecule and thus forming a neutral atom and a positively charged molecular ion, e.g.

$$N^+ + O_2 \rightarrow NO^+ + O.$$

In the second phase, electrons merge with the newly created molecular ion, creating two neutral atoms,

$$NO^+ + e^- \rightarrow N + O.$$

Dissociative recombinations have higher reaction rates then radiative recombination. This results in shorter lifetimes for molecule ions compared with atomic ions. In view of the fact that the molecular ions are much shorter-lived, once their production rate is reduced at night recombination quickly reduces the plasma concentration (Kelley, 2009). The reader is referred to Kelley (2009), Park (2004), Davies (1990) and Craven (1997) for a more in-depth discussion of these two processes.



The formation and properties of the ionosphere above a given location on the Earth depend heavily on the processes that occur in the Sun (solar activity), the position of the Sun relative to that location on Earth, the Sun's absolute energy output, variations of the Earth's magnetic field (geomagnetic field effect), the density and content of the atmosphere at different altitudes and geographical latitudes, and so on. The reader is referred to (Moldwin, 2008), (Brekke, 1997) and (Kelley, 2009) for a detailed description of the latter. At night time, the ionosphere does not completely disappear since the recombination time of ions and electrons (the average total time needed for an ion and electron to come back together to form neutral atoms) is related to the rotation rate of the Earth (Moldwin, 2008).

Since there are varying abundances of atmospheric molecular and atomic species throughout the neutral atmosphere, photoionization and recombination rates will also vary, resulting in different electron density concentrations at different layers of the ionosphere (Kelley, 2009). These layers (or regions) denoted by D, E, F1 and F2 and their structure, formation and composition from the lowest to the highest layer, will now be discussed briefly.

#### 2.3.1.1 D Layer

The lowest region of the ionosphere, called the D layer, extends from approximately 50-90 km above the Earth's surface. From this region the ionosphere extends in an upward path to the top of the Earth's atmosphere, implying that the majority of the ionosphere is in the thermosphere. In this layer the primary source of ionization are cosmic rays at this altitude (Davies, 1990; Komjathy, 1997; Moldwin, 2008). Thus there is a clear relationship of the D layer's electron density with a strong solar cycle variation (Komjathy, 1997). In theory the electron density in the D layer above mid-latitude regions increases monotonically with altitude, and an average number during daytime is ~ $10^{10}$ $m^{-3}$. Since the neutral density in this layer is high, the overall recombination rate is great. As a result, since photoionization only occurs when the Sun's background radiation is present, the D layer electrons are only present during the day at an altitude of about 60 to 70 km (Komjathy, 1997; Moldwin, 2008). Also, during night time the chances of electrons attaching to atoms and molecules to form negative ions are rather high, causing the D layer to completely disappear (e.g. Komjathy, 1997). At heights near and above 80 km, oxygen and nitrogen are mostly present and are ionized by X-radiation of wavelengths less than 1 nm (Ratcliffe, 1972).



#### 2.3.1.2 E layer

Above the D layer is the E layer, which ranges from an altitude of 90-140 km. Ionization in this layer results from low energy X-rays (1-10 nm) and ultraviolet (UV) solar radiation of molecular oxygen ($O_2$) (Moldwin, 2008; Opperman, et al., 2007a, 2007b), which result in electron densities showing distinct solar cycle, seasonal and diurnal variation (Komjathy, 1997). This layer's peak electron density is more than 100 times greater than the peak density in the D layer, since recombination occurs less at these high altitudes (Moldwin, 2008). Similar to the D layer, the E layer is also present during day time and decreases during night time to nearly zero electron density (Komjathy, 1997). The other sources for ionization (but not to a great extent) in the layer are particle precipitation at high latitudes, effects of neutral atmosphere motion, auroral electric fields and meteors entering the upper atmosphere (Moldwin, 2008). The reader is referred to (Moldwin, 2008) for a more in-depth discussion on the latter.

#### 2.3.1.3 F layer

The third, most dense, and predominant layer of all the electron density profiles in the ionosphere is called the F layer, starting from an altitude of ~140 km up until 1000 km, peaking at 300-400 km, depending on the level of solar activity. A typical representative daytime maximum electron density value is in the region of $10^{12}$ $m^{-3}$ (Hunsucker and Hargreaves, 2003). The region above the peak altitude is called the topside ionosphere and here the density gradually decreases and transitions into a magnetospheric region called the plasmasphere. The transitional zone between these two regions has a width in the range of 1000 km, and is marked by the transition from oxygen as the main ion in the ionosphere to hydrogen as the main ion in the plasmasphere (Moldwin, 2008). Thus the F layer stops where the ratio of oxygen ions to hydrogen ions drops below one. This layer can split into two sub layers, depending on the local time and geographical location (Fernandez, 2004).

##### 2.3.1.3.1 F1 layer



The sub layer ranging from 140-210 km is called the F1 layer. Throughout the winter, the F1 layer disappears; the solar zenith angle is higher than in summer, at which time the F1 layer is constantly present. During daytime the presence of the F1 layer is controlled by the zenith angle of the Sun. At night time the F1 layer disappears to unite with the F2 layer to structure the night time F layer (Opperman, et al., 2007a).

##### 2.3.1.3.2 F2 layer

The sub layer ranging from 210-1000 km is called the F2 layer, and contains the maximum electron density in the ionosphere, because of the combined effect of solar EUV radiation and the increase of neutral atmospheric density as the altitude decreases (Kelley, 2009). In terms of the propagation of high frequency (HF) radio waves this layer is considered to be the most critical layer in the ionosphere, and the most important parameter is the height maximum of the F2 layer (or hmF2). The height and electron density of this layer is greatly changeable, and large daily, seasonal and sunspot-cycle variations are combined with general unpredictable behaviour (Opperman, et al., 2007a). Unlike the F1 layer, which follows the solar zenith angle dependence, the F2 layer is high enough that there is no seasonal effect due

to the solar zenith angle (Komjathy, 1997). A descriptive image of the ionosphere can be seen in Figure 2.4.

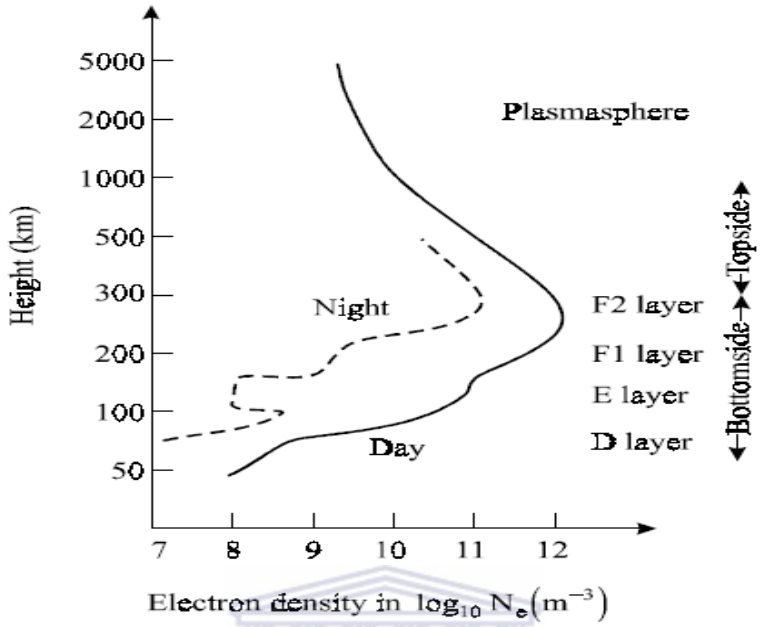


**Figure 2.4:** Illustration of a typical vertical profile of the ionosphere [from Davies (1990) and Komjathy (1997)].



## 2.4 Major geographic regions of the ionosphere

Generally the terrestrial ionosphere has three major geographical regions, namely the equatorial, the mid latitude, and the high latitude regions. The identification of these regions is based on the rather different properties according to their geomagnetic latitude (Hunsucker and Hargreaves, 2003). In the following sub section, the main characteristics of these three regions are illustrated (Figure 2.5) and described.

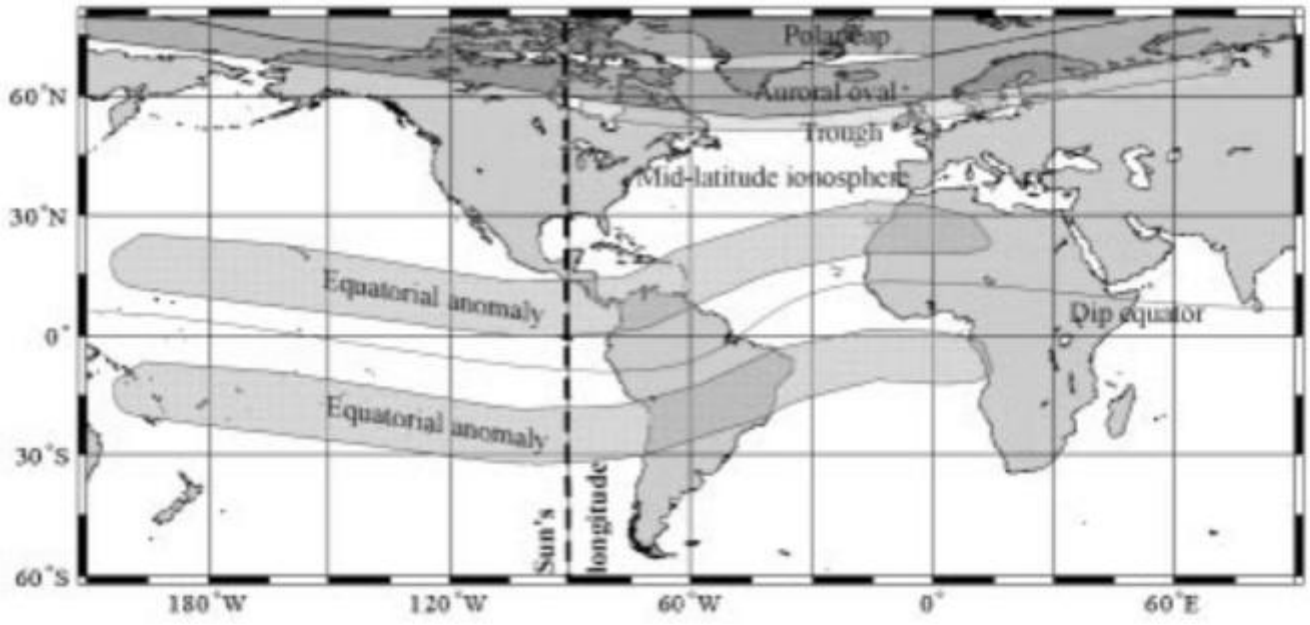


**Figure 2.5:** Geographic regions of terrestrial ionosphere (from Bishop, et al., 1991).



## 2.4.1 The equatorial region

The equatorial region of the ionosphere, occasionally referred to as the low latitude zone, extends to 20°-30° on either side of magnetic equator. It is strongly influenced by EM forces that arise due to the geomagnetic field which runs horizontally over the magnetic equator. This region is known for the high values of peak electron density with the utmost prominent amplitude and phase scintillation effects. Combining the effects of the high radiation level from the Sun and electric and magnetic fields of the Earth result in electrons rising up due to a horizontal electric field produced by the dynamic action in the E-region, and then moving along the horizontal lines of the magnetic field (Komjathy, 1997). The electrons will drift due to a combination of thermal diffusion and electrodynamic drift along the magnetic field lines to higher geomagnetic latitudes, causing a high concentration of electrons, termed ionospheric equatorial anomalies (IEA). This phenomenon, known as the fountain effect, results in the distortion of the general form of the ionosphere throughout the low latitude zone (Hunsucker and Hargreaves, 2003; Brekke, 1997).

### 2.4.2 The mid-latitude region

The mid latitude region is roughly between 35°-65° latitude in the north and the south, and is occasionally referred to as the temperate region. It is the region that has been explored the most completely and is best understood. This region has the smallest amount of variability and is the most undisturbed among the different ionospheric regions. In this region the ionization is almost entirely influenced by energetic solar EUV and X-ray emissions from the Sun, which result in ionization of the daytime ionosphere. Night-time ionization results from chemical recombination processes, which involve neutral atmosphere in addition to ionized species. The majority of ionospheric observations and studies have been done over this region, due to the fact that the majority of ionosphere sensing instruments have been established in countries situated in the mid-latitude region (Komjathy, 1997; Hunsucker and Hargreaves, 2003).

### 2.4.3 The high latitude region

In the equatorial region a strong current flows in the E-region, and the F-region is subject to electrodynamic lifting and the fountain effect. At high latitudes the situation is totally opposite. In this region the geomagnetic field runs virtually vertical, and this change leads to the existence of an ionosphere that is greatly more complex than that in the mid and low latitude zones. Motivation for this complex change is because the magnetic field lines connect the high latitudes to the outer part of the magnetosphere, which is determined by the solar wind and eventually leads to the charged particles descending to E layer altitudes.

However, whereas the ionosphere at mid latitude zones is linked to inner magnetosphere, which basically rotates with the Earth and is thus less responsive to external influence (Hunsucker and Hargreaves, 2003), the high latitude region is dynamic and thus circulates in a pattern that is primarily controlled by the solar wind but is also variable. Energetic particle emissions from the Sun are easily accessible in this region, which produces additional ionization, and thus this region can be affected by sporadic events that can degrade polar radio propagation. When these energetic particles collide with neutral atmospheric gases, local enhancements of electron densities result, as for example during auroral activity.

Auroral activity involves interactions between the magnetosphere, the ionosphere and the atmosphere. Auroral zones occur within the high latitude region, and their location depends

on the linkage with the magnetosphere. Characteristically auroral zones are relatively narrow rings located in the higher southern and northern geomagnetic latitudes. In general, the intensity and the position of the auroral oval results from the linkage with the magnetosphere and is related to geomagnetic perturbations (McNamara, 1991). Auroral phenomenon includes electrojets, which causes magnetic perturbations and also substorms, where the rate of ionization increases greatly due to the arrival of energetic electrons. These auroral zones are regions that are particularly complex for radio propagation (Hunsucker and Hargreaves, 2003). The geographical regions enclosed by the auroral rings are called the polar caps, and these regions are affected tremendously by solar flares and Coronal Mass Ejections (CME) causing the D region electron density enhancements (Komjathy, 1997).

## 2.5 Ionospheric Disturbances

Throughout this thesis, the term "ionospheric disturbance" is used to cover a broad selection of ionospheric conditions that depart from the usual or quiet state (Davies, 1990). It can result from solar disturbances that occur on the Sun, and from geomagnetic disturbances, which are triggered in more complex ways by events initiating from the Sun. These events affect the outermost geomagnetic field lines and compress the geomagnetic field causing geomagnetic disturbances (Komjathy, 1997). Thus, the set of ionospheric disturbances is associated either directly or indirectly with events on the Sun (Davies, 1990), and these will be discussed in the subsection.

### 2.5.1 Ionospheric Storms

Solar flares or CME result in the enhanced flux of intense energetic particles emitted by the Sun. These enhanced flux releases often generate enormous variations in the particle and EM radiation incident upon Earth and such variations can result in disturbances of the quiet time magnetosphere and ionosphere. The disturbances of the ionosphere are identified as ionospheric storms, which have a tendency to produce large disturbances in ionospheric density distribution and total electron content. These storms symbolize an extreme form of space weather, which has social and technological impacts on space borne and ground based technological systems (Davies, 1990).

### 2.5.2 Geomagnetic Storms

The amount of energy transferred into the magnetosphere from the Sun can increase quickly. Such rapid increases are often coupled with the impact of Earth with southward IMF from a CME. The southward IMF reconnects efficiently with the northward field of Earth (Moldwin, 2008). A geomagnetic storm results because of the large sudden change of energy flux that changes the solar wind dynamic pressure of the magnetosphere, which occurs when it is impacted by a CME or solar flare (Schunk and Nagy, 2009). These storms usually happen in conjunction with ionospheric storms and can be solar flares, coronal holes and sudden disappearing filaments (Komjathy, 1997).

Throughout the key phase of the storm, charged particles in the nearby plasma sheet of the Earth are energized and injected deeper into the inner magnetosphere, and this effect can be predominantly strong when the increased solar wind pressure is associated with an enormous southward IMF component. This phase is finally followed by the recovery phase (which can last for many days) and characterized by the occurrence of several possible powerful substorms (Schunk and Nagy, 2009).

The high latitude E region experiences major effects during geomagnetic storms, where particle precipitation in the cusp and aurora are a source of substantial ionization. The number of storms varies with the solar cycle of the Sun, and is a typically on the order of a few per month, where the quantity and intensity is most during solar maximum (Moldwin, 2008). Coupled in the midst of each storm is a fast brightening and growth of the entire auroral oval in both the northern and southern hemispheres.

### 2.5.3 Ionospheric scintillations

One of the first known space weather effects was fast, random fluctuations in the amplitude and phase of radio signals moving through the ionosphere. These fluctuations are termed scintillations, and they have considerable impact on the performance of satellite communication and navigation (Kitner, 2007; Wernik, et al., 2007). Such effects arise from radio frequency propagation through regions where small-scale irregularities in electron density exist. These regions can range in size from a few meters to a few kilometers, and they cause both refraction and diffraction of EM waves propagating through the ionosphere.

Scintillation is described by substantial spatial and temporal inconsistency, which depends on numerous factors, for instance signal frequency, local time, season, solar and magnetic activity and satellite zenith angle (Wernik, et al., 2007). The rapid phase variations, called phase scintillations, causes a Doppler shift in GPS signals and also contributes to rapid but small changes in ionospheric electron content (Skone, et al., 2000). A modification of up to 1 radian in phase is needed at 1.5 GHz to correct for problems in the GNSS receivers' tracking loop (Langley, 1996; Komjathy, 1997).

## 2.6 Magnetic Activity Indices

In the absence of direct measures of activity in the ionosphere and magnetosphere, the geomagnetic indices are used as proxies for the solar and geomagnetic disturbance levels. In turn, the majority of computational space weather simulations (empirical and physics based models) use geomagnetic indices to indicate the solar and geomagnetic disturbance levels. These magnetic indices were primarily intended to define discrepancies in the geomagnetic field, triggered by irregular current systems between the magnetosphere and ionosphere. Commonly these indices are derived from parameters which are monitored continuously with ground-based equipment. The space weather scientific community mostly makes use of the Kp, Ap and Dst indices, which are briefly described as follows (Rostoker, 1972; Davies, 1990).

### 2.6.1 Kp index

The Kp (planetarische Kennziffer) index is a quasi-logarithmic local index of 3 hour range designed to measure the uneven discrepancies in the Cartesian components of the Earth's magnetic field (x, y, z), and is intended to give a universal measure of geomagnetic activity (Davies, 1990). Introduced by J. Bartels in 1938, it consists of single digits that start from 0 to 9 for every eight 3 hour intervals of a universal time day (UT). It is computed as the arithmetic mean of the K values calculated at the thirteen geomagnetic observatories that are situated between 48° to 63° North and South geomagnetic latitude. Thus, Kp is a mid-latitude geomagnetic index. A stable scale is adopted for each observatory but the scale differs from observatory to observatory.

The amplitude range called R ($R_{max}$ - $R_{min}$) measured in gammas (nano Teslas) is used to define a particular K value. Diverse R values correspond to diverse K values at different observatories, to make sure that a disturbed day at a mid-latitude observatory has more or less the same K value as that for an auroral observatory. As an example of the latter, the value of R for K = 9 varies from 1500 nT at Godhaven Greenland to 300 nT at Honolulu Hawaii (Davies, 1990). The Kp index has 28 grades from 0 (no activity) to 9 (major storm activity) with fractional parts expressed in a third of a unit (Komjathy, 1997). The Kp index is not particularly satisfactory for representing disturbances within the polar cap (Davies, 1990).

### 2.6.2 Ap index

The Ap index (or daily equivalent planetary amplitude) is a 3 hour index that is equivalent (linear) in range and is derived from the Kp index values. Some applications in space weather require a daily index, and the K sum is not suitable because of its quasi-logarithmic nature. The daily Ap index can be defined as the earliest occurring maximum 24 hour value, computed as an 8 point running average of consecutive 3 hour Ap indices through a geomagnetic storm event. It is distinctively coupled with the storm event (Davies, 1990). Since Ap is derived from Kp, it is also a mid-latitude geomagnetic index.



### 2.6.3 Dst index

The Disturbed Storm Time (Dst) index is an index that measures the intensity of a geomagnetic storm and the development of the ring current (Moldwin, 2008). Dst is expressed in nano Teslas and is derived from the average value of the horizontal component of the Earth's magnetic field measured hourly at a network of four near equatorial geomagnetic observatories. These observatories make this measurement possible due to averaging the horizontal component of the geomagnetic field from equatorial and mid latitude magneto-grams from the universal set-up of magnetometers. The Dst index value tends to a negative value since the Earth's field weakens (particularly during solar storms), due to increase in the strength of the ring current (Moldwin, 2008), which moves around the Earth in an easterly to westerly direction in the equatorial plane. The Dst index is a particularly useful index of storm strength since the strength of surface magnetic field at low latitudes is inversely proportional to the energy content of the ring current, which increases during geomagnetic storms.

Ring currents result from differential gradient and curvature drift of electrons and protons in the nearby Earth region, and its strength is coupled to the solar wind conditions. This is due to the presence of an electric field arising from magnetospheric convection, which in turn results from the interconnection between the southward IMF and the geomagnetic fields. Once the IMF moves in a northward direction and ring current recovers, the Dst index value gradually increases back to its quiet time level. Because the physics of the coupling between the ring current and ground-based magnetometers is well understood, the Dst index is a good proxy for mid-latitude geomagnetic activity (Davies, 1990).

## 2.7 Satellite Missions

Given that the main purpose of this thesis is to describe the disturbances of the ionospheric electron density over Southern Africa during geomagnetic storms, using data obtained from the GNSS network, this section will briefly discuss the different GNSS network systems that are presently in operation or are still in the planning phase.

### 2.7.1 Global Navigation Satellite System



The acronym GNSS (Global Navigation Satellite Systems) is a general term used for satellite navigation used within the International Global Navigation Satellite Systems Service (IGS) community. Initially GNSS were used to determine an object's location (position, velocity and altitude) by employing small electronic receivers to interpret time signals transmitted by radio along a line of sight from satellites. For the last 10 years, the number and types of military, commercial, scientific applications and research that utilize precise positioning and timing information has increased significantly. In the new age of GNSS, a very well known, widely used, fully operational and highly important satellite system is the US NAVSTAR GPS (Global Positioning System). In addition, the Russian satellite system, GLONASS, is in the process of being restored to full operation. The future European satellite system, GALILEO, which is in the deployment stage is scheduled to be fully functional and compatible with GPS in 2014. Finally, the People's Republic of China's satellite system, COMPASS (expanded from the Beidou system), is scheduled to become operational in 2020 (Gleason and Gebre-Egziabher, 2009).

Due to the instrumental limitation in receiving signals from GLONASS and GALILEO over Southern Africa, this research work will mainly focus on GPS, and thus discussions will be more in depth on GPS and less so for the other three satellite systems. The prospective installation of GNSS receivers over the Southern Africa Development Community (SADC) region by Hartebeesthoek Radio Astronomy Observatory (HartRAO) would aid in the reception of signals from all of the GNSS constellations (Moeketsi, 2007a).

## 2.7.2 Global Positioning System

The US NAVSTAR Global Positioning System (GPS) is a constellation of 24 or more worldwide satellite based radio-navigation systems that provides accurate location of objects globally and is operated by the US Department of Defence (DoD). Even though GPS is owned and operated by the US DoD and was developed first and foremost for defence applications, it is presently used widely in both the defence and civilian communities in most countries (Knight, 2000). In 1978 the first operational GPS satellite was launched, and until 1985 a total of 11 Block I satellites were launched. Four years later, in 1989 a new type of satellite, the Block II satellite, was developed and was also launched. In 1993 the constellation of systems was fully operational with 30 (24 active and 6 on standby) satellites orbiting Earth. The GPS system consists of three system segments (space segment, the control segment and the user segment), and this is the most suitable way of also describing the system.



### 2.7.2.1 Space Segment

The space segment is a constellation of at least 24 satellites in near circular orbits of 26,600 km radius (about 20,200 km above the surface of the Earth). Each of these satellites orbits the Earth in around 12 hours. These satellites are distributed in six orbital planes (with four satellites per plane), and each plane is tilted at angle of 55° relative to the equator to provide polar coverage. This polar coverage ensures that at least four satellites are detectable at all times everywhere on Earth, which is the minimum required for accurate three-dimensional positioning by a receiver. An image of the locations of the orbiting satellites is shown in Figure 2.6.

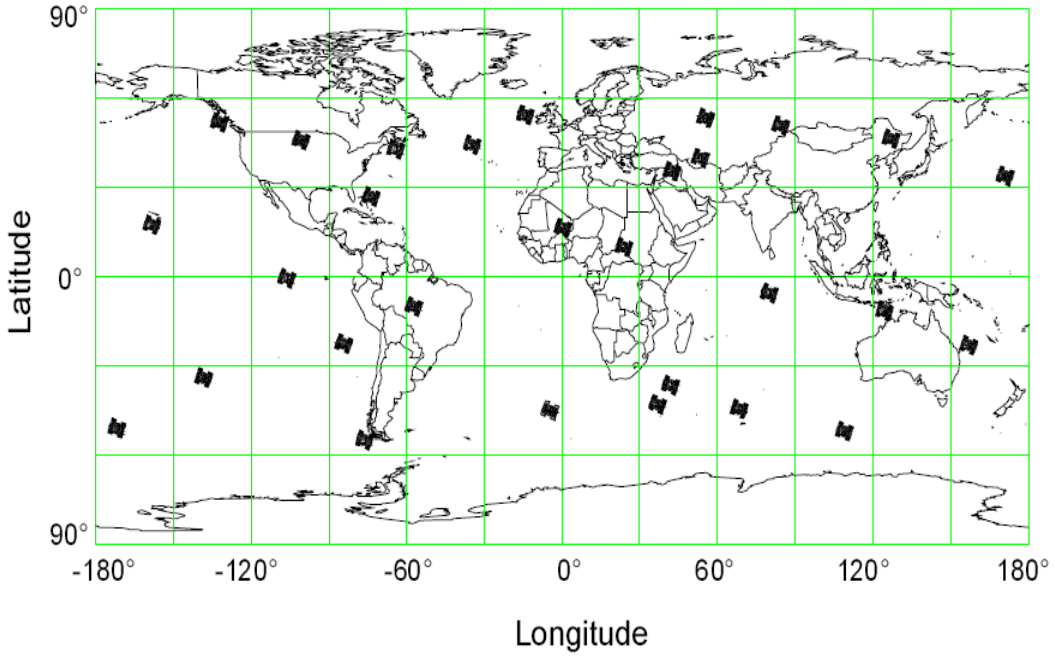


**Figure 2.6:** Position of the 28 GPS satellites at 12.00 hrs UTC on 14th April 2001 (from Zogg, 2002).



Each of these autonomous satellites has four atomic clocks on board, to keep extremely precise time. They each transmit a navigation signal that has a number of components, including sine waves (carrier frequencies of L1 = 1575.42 MHz, L2 = 1227.6 MHz and L5 = 1176.45 MHz), two digital codes and navigation message. The carrier frequencies are modulated by two pseudo-random noise codes and a navigation message. Measured travel times of the signals from the satellites to a receiver on the ground are used to compute the pseudoranges (El-Rabbany, 2002). Course-Acquisition (C/A) code, occasionally called the Standard Positioning Service (SPS), is a PRN code that is modulated onto the L1 carrier. The precision (P) code, occasionally called the Precise Positioning Service (PPS), is modulated onto the L1, L2 and L5 carriers thus allowing the removal of any effects of the ionosphere (Xu, 2007).

### 2.7.2.2 Control Segment

The control segment of GPS is made up of a master control station (MCS), a worldwide network of monitoring stations, a worldwide network of ground stations, and a tracking network to connect them together. The ground stations transmit information to the satellites (uplink) and the monitoring stations receive satellite signals (downlink). All of these stations are geographically spread in longitude around the globe in the vicinity of the equator, belonging to the Operational Control System (OCS). The MCS is situated near Colorado

Springs, Colorado. It is the central processing facility for the control segment and is manned at all times. All of the monitor stations track the navigation signals from all the satellites in orbit and continuously send data to the MCS for processing. Tasks of the MCS are to calculate and predict orbit position projections for each satellite in the constellation and to correct for satellite clock errors based on tracked data.

#### 2.7.2.3 User Segment (GPS receivers)

The User Segment consists of GPS receivers and antennas, providing positioning, velocity and precise timing both for military and civilian use (El-Rabbany, 2002). This service is at present offered to any user anywhere in the world who has a GPS receiver device, at no direct charge.

## 2.7.3 GLONASS

The GLONASS (GLObal Navigation Satellite System) is an all-weather global radio based satellite navigation system developed by Russia for use by the Soviet military. It was launched in 1982. As with GPS, the GLONASS system is also designed to have a full 24 constellation of satellites, but GLONASS only attained a maximum of 21 operational satellites, plus three spares at an altitude of 19,100 km, during the first half of 1996. During the next ten years, considerably fewer operational satellites were in orbit due to budget constraints. Since 2011, Russia has renewed efforts to improve its satellite system.



## 2.7.4 GALILEO

The European Union (EU) and European Space Agency (ESA) are in the process of the development of a GNSS called Galileo, providing highly accurate global positioning service under the civil control (Xu, 2007). Europe's own global navigation satellite system, Galileo provides a highly accurate, guaranteed global positioning service under civilian control. By offering dual frequencies as a standard, Galileo will deliver real-time positioning accuracy down to the meter range. Even in the most risky circumstances, the Galileo system will guarantee availability and inform users within seconds of any satellite failure. The development of this constellation is the EU attempt to offer both an option and a complement to the GPS and GLONASS systems (Mendizabal, et al., 2009). Three different types of constellations were investigated to ensure optimum selection of the Galileo architecture,

namely low Earth orbits (LEO), medium Earth orbits (MEO), and inclined geosynchronous orbits (IGSO) (El-Rabbany, 2002). The Galileo navigation system will act independently and thus will be interoperable with GPS and GLONASS. On the 21st of October 2011, the first two of four operational satellites designed was launched to validate the Galileo concept in both space and on Earth. The following year on the 12th of October 2012, the other two operational satellites followed making it possible to test the Galileo end to end. Once this In-Orbit Validation (IOV) phase has been completed, additional satellites will be launched to reach Initial Operational Capability (IOC) around mid-decade. The complete deployed Galileo system expected by 2019 will consist of 30 satellites (27 operational plus 3 active spares), positioned in three MEO planes at an altitude of 23,222 km above the Earth, at an inclination of the orbital planes of 56 degrees to the equator.

### 2.7.5 COMPASS



The COMPASS system development arose from the decision of the Chinese government to expand their system of Beidou geostationary satellites to cover global navigation. In 2000, China launched two satellites called Beidou 1A and Beidou 1B, located at 140°E and 80°E, respectively and a third one, called Beidou 1C, located at 110°E in 2003 (Prasad and Ruggieri, 2005). The COMPASS system is projected to add as many as 30 medium Earth orbit satellites to several geostationary satellites already maintained over China, for land and marine transportation in the coastal regions of China. These satellites form the first generation of satellite based navigation systems (Beidou Navigation System) that is placed in geostationary orbits at an altitude of approximately 36,000 km above the Earth's surface (El-Rabbany, 2002).

## 2.8 Summary

In this chapter, background theory was presented about the Sun and its activity cycle, the Earth's ionosphere and its structure, disturbances in ionosphere and succeeding effects on propagation of EM waves as connected to this work. A brief description was also presented on the different geomagnetic indices used in space weather physics research. In addition, crucial satellite missions such as GNSS, which consist of GPS, GLONASS, GALILEO and

COMPASS, using the data of the GNSS system as a critical source for this research study were also discussed briefly.

The next chapter will focus on the ionospheric TEC modelling techniques using GNSS used locally and abroad, MAGIC ionospheric modelling, Kalman Filtering Assimilation technique, the physics behind MAGIC in looking at the propagation of radio waves in the ionosphere and finally a concise discussion on MAGIC for TEC calculation and GNSS networks over South Africa.

# Chapter 3

# IONOSPHERIC TOTAL ELECTRON CONTENT MODELLING TECHNIQUES

## 3.1 Introduction

This chapter is devoted to providing a concise description of the MAGIC model which is used as the primary tool in this research study. It starts with a review of ionospheric TEC modelling using the GNSS technique, followed by modern developments and efforts undertaken by South Africa to model the ionosphere using GPS. It then proceeds with a description of the MAGIC ionospheric modelling technique, including a discussion on the Kalman Filtering Assimilation technique which is used in MAGIC to form the estimations of the state of the ionosphere. The chapter continues by discussing the physics behind MAGIC, looking at the propagation of radio waves in the ionosphere amongst other sub topics. Finally the chapter concludes on a concise discussion on MAGIC for TEC calculation and GNSS networks over South Africa.



## 3.2 Review of global and local ionospheric TEC models using GNSS

The existence of the ionosphere was accidentally established in 1901 by G. Marconi, when he transmitted radio signals 3500 km across the Atlantic. The experiment evidently showed that the transmitted radio waves were deflected around the Earth's surface to a superior degree than could be credited to diffraction (Schunk and Nagy, 2009). The history of ionospheric research begins with the pioneering experiments done by Appleton and Barnett (1925) and Breit and Tuve (1926), where frequency change experiments and pulse sounding techniques were used, respectively, to determine from reflected radio signals the height and charge composition of the ionospheric layer (Opperman, 2007a; Schunk and Nagy, 2009). Early observational studies of the ionospheric TEC were done by using data from geostationary radio beacon satellites, with the help of the Doppler shift and Faraday rotation technique (Garriott, et al., 1965). The latter studies used data that were obtained from either single

frequency receivers or a ground network of instruments. In view of the decreasing number of onboard experiments on the Doppler and Faraday satellites, and the introduction of GNSS such as the Russian GLONASS, US GPS, European GNSS and future satellite systems such as China COMPASS, it is now possible to use the GPS technique for a comprehensive study and analysis of the ionosphere.

Since the ionosphere is a dispersive medium (Ratcliffe, 1959), it exerts noteworthy influence on the propagation of EM waves such as GNSS signals and radio waves by inducing transmission time delays and phase advances (Langley, 1996). The scale of these effects depends on the frequency of the EM waves and on the concentration density of the ionized gas (Moldwin, 2008), and this delay needs to be corrected for single frequency users in applications such as GPS positioning, navigation and communication. One of the ionospheric correction models using GPS is the Klobuchar ionospheric delay model, and this model is a global polynomial based model that was developed for correcting a single frequency receiver's signals for ionospheric delay; see Opperman et al. 2007a for further discussions. The model is based on a function fitting approach and is not particularly precise, typically accounting for only 50% of the total ionospheric effects (Gao and Liu, 2002). Additional function based models have been developed, such as polynomial function fitting techniques such as the University of New Brunswick Ionospheric Modelling Technique (UNB-IMT) (Komjathy, 1997); spherical harmonics techniques (Walker, 1989; Schaer, 1999) and Kalman filter techniques (Mannucci, et al., 1993; Spencer, et al., 2004). One example of an ionospheric model that uses Kalman filter techniques is called the Global Assimilation of Ionospheric Measurements (GAIM). This is a physics based data assimilation model of the ionosphere and the neutral atmosphere that uses a global ionosphere-plasmasphere model and a Kalman filter as a basis for assimilating a diverse set of real-time (or near real-time) measurements. The GAIM model provides specifications and forecasts on a spatial grid that can be global, regional, or local (Schunk, et al., 2002, 2005). An additional model called NeQuick is a three dimensional and time dependent electron density model specifically designed for transionospheric propagation applications. It allows calculation of electron concentration values at any position in the ionosphere and the TEC along any ground station to satellite ray path (Nava, et al., 2008). Although the IGS GPS networks gave rise to the development of global ionospheric models, the idea of regional models (e.g. MAGIC model) is also a vital tool for applications such as geodesy (Spencer, et al., 2004).

In past years, efforts were taken to enhance modelling of the ionosphere using tomography techniques (e.g. Fremouw, et al., 1992,1994; Hansen, et al., 1997, 1998; Hernandez, et al., 2000; Howe, et al., 1998; Rius, et al., 1997; Tsai, et al., 2002). These ionospheric tomography models describe the ionospheric field in four-and three dimensional frames instead of the two-dimensional frames used by other ionospheric models, as discussed earlier. Monitoring and studies of the ionosphere with the use of the diverse models, as described above, is possible due to a densely distributed GNSS network, such as in the northern hemisphere. The GNSS network in southern Africa is less well populated, although efforts are constantly in the development to increase the density of the network in this region. Studying the behavior of the ionosphere in South Africa is well researched and efforts has been undertaken to utilize and adapt global and regional ionospheric models to characterize the dynamics and variations of the ionospheric parameters, such as TEC, over the South African region (Habarulema, 2010; Moeketsi, 2007; Okoh, 2009; Opperman, 2007b). Models that have been adapted thus far include: the Multi-Instrument Data Analysis System (MIDAS) algorithm, which is used for ionospheric tomography inversion, and was developed at the University of Bath (Mitchell, et al., 1997; Cilliers, et al., 2004); the spherical harmonic model, now referred to as a variable degree adjusted spherical harmonic (ASHA) model, (Opperman, et al., 2007a;); the UNB-IMT (Komjathy, 1997; Fedrizzi, et al., 2005; Ngcobo, et al., 2005, Moeketsi, et al.; 2007b,c); an information processing system known as Artificial Neural Networks (NNs) (Habarulema, et al., 2007; Habarulema, et al., 2009a,b,; Habarulema, 2010); and the development of an ionospheric TEC map for South Africa by the use of three currently available resources, namely the IRI, South African Bottomside Ionospheric Model (SABIM) and measurements from ionosondes in the South African Ionosonde Network (Okoh, 2009). Lastly, there is the MAGIC model (Spencer, et al., 2004; Araujo-Pradere, et al., 2006, 2007) which was developed and applied over the American sector, and is used as a research tool for this study and is described in the subsequent section. To conclude, the MAGIC model evolved from MIDAS (Opperman, et al., 2007a), where the main difference between the two models is MAGIC's use of the Kalman filter.

## 3.3 The MAGIC Ionospheric Modelling Technique

### 3.3.1 Introduction

The ionospheric modelling technique known as MAGIC is a Kalman filtering based assimilation algorithm used for imaging the Earth's ionosphere in four dimensions through the interpretation of GNSS data. The MAGIC model was developed at the University of Colorado, Boulder, USA, and was initially started and evolved through collaboration between the US Space Weather Prediction Center (SWPC), US National Geodetic Survey (NGS), US National Geophysical Data Center (NGDC) and the US Global Systems Division (GSD). The goal of the MAGIC model is to indicate vertical and slant TEC over the Continental US (CONUS) in near real-time (Fuller-Rowell, 2005; Araujo-Pradere, et al., 2006, 2007). The MAGIC algorithm depends on third party software in the form of the IRI95 ionospheric model. The MAGIC package (Spencer, et al., 2004) was developed as a research tool in order to study diverse approaches to the difficult problem of obtaining an approximation of the ionosphere which is adequately precise to be useful in geodetic positioning applications. Recently, Araujo-Pradere (et al., 2006, 2007) have applied the model to study consistent features of changes in TEC during ionospheric storms using GPS data from the Continuously Operating Reference Stations (CORS) network. Also Minter (et al., 2007) did a comparison of MAGIC and the satellite based Fast Onboard Recording of Transient Events (FORTE) ionospheric measurements.

### 3.3.2 Kalman Filter Assimilation

A Kalman filter (recursive estimator) is a statistical predictor-corrector scheme for iteratively estimating the state of a noisy linear system, given some set of regularly updated measures upon that system. The algorithm, which can be expressed as an efficient recursive scheme, creates the estimate of the state in a way that minimizes the expectation of the squared error. This method is based on two inputs, the estimate for the previous (last time step) state of the system and the (noisy) measurement(s) taken on the present state of the system. Thus the model is a mapping of the previous state of the system to the present state of the system, and explicitly contains the fact that the process is noisy (Kalman, 1960).

The first step of the Kalman filter is called the prediction step, where the Kalman filter predicts the current state of the system based on the previous state as shown in Equation 3.1

$$\tilde{x}_i = A\hat{x}_{i-1}. \tag{3.1}$$

Here, $\tilde{x}_i$ is the prediction of the system state at time step $i$, $\hat{x}_{i-1}$ is the previous state estimate at step $i-1$, $A$ is the matrix that describes the model which relates the state at step $i-1$ to the state of step $i$ in absence of any process noise and $i$ is the index of the time variable.

At the time of the prediction step, the Kalman scheme also projects the error covariance term, $\tilde{P}_i$. This term quantifies the uncertainty of the first prediction of the state, and is shown in Equation 3.2

$$\tilde{P}_i = AP_{i-1}A^T + R_{i-1} \tag{3.2}$$

here, $\tilde{P}_i$ is the *a posteriori* error covariance matrix and $R_{i-1}$ is the process noise covariance.



The next step of the Kalman filtering process is called the correction step, or measurement update step. In this step the Kalman filter updates the first prediction attained at step 1 of the prediction stage, based on the measurement received. At this update stage the optimal Kalman gain is calculated, and can be seen in Equation 3.3

$$K_i = \frac{M\tilde{P}_i M}{Q_i + M\tilde{P}_i M} \tag{3.3}$$

here $K_i$ is the Kalman gain, $M$ is an observation matrix and $Q_i$ is the error covariance.

The optimal Kalman gain is used to create the new estimated state of the system. It can be seen that the new state estimate is in fact the prediction of the state made in the first step, plus a correction factor which is proportional to the difference between the actual measurement and the measurement on the prediction of the state made in the first step.

Thus this is a correction step. The new state estimate can be seen in Equation 3.4

$$\hat{x}_i = \tilde{x}_i + K_i M^{-1}(z_i - M\tilde{x}_i) \tag{3.4}$$

here, $K_i$ is the optimal Kalman gain, $z_i$ is the measurement on the actual system and $M\tilde{x}_i$ is the measurement on the prediction of the system state. The difference between these last terms is called the residual.

The last stage in the correction stage is the update of the *a posteriori* error covariance matrix, and can be seen in Equation 3.5.

$$P_i = (1 - K_i)\tilde{P}_i \tag{3.5}$$

here, $\tilde{P}$ is the error of the prediction of the system state, from Equation 3.2. To summarize, the Kalman filter estimation method consists of two steps, the prediction step and correction step. In the first step, two predictions are made, namely, $\tilde{x}_i$ and $\tilde{P}_i$. In the prediction step, the system state will be predicted based on the model acting on the previous state estimate. In the correction step, the optimal Kalman gain is calculated, and then used to correct the prediction and to give an estimate of the new state of the system, as well as the error covariance of that estimation.

## 3.4 Radio and Electromagnetic Wave Propagation

### 3.4.1 The propagation of radio waves and their effects in the Ionosphere

The understanding and interpretation of EM waves, such as radio waves, that are transmitted through and reflected from the ionosphere is vital for satellite navigation systems, such as GPS as well as radio communications. A GPS receiver position is estimated by calculation of the time delay between radio signals transmitted from space by each satellite and the reception of those signals at the given receiver. Under the assumption that the EM waves are travelling at the speed of light in vacuum, *c*, the delay is transformed to a receiver satellite

distance. By using the distance to multiple satellites of known location, a GPS receiver can determine the three dimensional position of the receiver.

Thus the first thing to consider when studying the propagation of radio waves through the ionosphere is the variation of the index of refraction of a traveling radio wave in an ionized magnetic medium (Gillies, 2006). The derivation of the refractive index of the ionosphere as a magneto-ionic medium was computed by a number of scientists, but in most literature and books the name Sir Edward Appleton is associated with this theory. He was first to point out that a plane polarized wave would be split into two oppositely rotating circularly polarized waves by a magnetized plasma (Hunsucker, 1991; Komjathy, 1997). His result is also known by a number of titles such as the Appleton-Lassen formula (Rawer and Suchy, et al., 1976), Appleton formula (Ratcliffe, 1959) and Appleton-Hartree formula (Budden, 1985). In 1931, Hartree recommended the inclusion of the Lorentz polarization term, and thus the complex index is referred to as the Appleton-Hartree formula (Komjathy, 1997). The Appleton-Hartree magneto-ionic theory applies to a medium which is electrically neutral i.e. which has an equivalent number of electrons and positive ions, and in which a constant magnetic field is present. It is found that the effect of significantly heavier positive ions on the wave is insignificant (e.g. Komjathy, 1997).



In the next subsections to follow are the computations of the phase and group refractive index (Section 3.4.2 and 3.4.4, respectively) as well as the group and phase velocities (Section 3.4.5) of a wave.

The refractive index, $n$ of a substance, describes how light propagates through a medium, and is given in terms of the speed of light in vacuum, $c$ and $v$, the speed of light in the substance as

$$n = \frac{c}{v}.$$

The group velocity of a group of waves is the velocity with which the overall shape of the wave amplitudes through space, and is given in terms of the angular frequency of the wave ($\omega$) and angular wavenumber ($k$) as

$$v_g = \frac{\partial \omega}{\partial k}.$$

The phase velocity of a wave is defined as the rate at which the phase of the wave propagates in space, and is given in terms of the angular frequency ( $\omega$ ) and frequency ( $k$ ) as

$$v_p = \frac{\omega}{k}.$$

### 3.4.2 Computation of Complex Phase Refractive Index

To obtain the refractive index for plane waves in homogenous plasma, one first invokes Maxwell equations and then applies the properties of the medium. The Maxwell equations are used to derive a relationship between the magnetic and electric fields of a propagating EM wave. The interested reader is referred to Gillies (2006) for a complete derivation and to Davies (1990) for a concise derivation of the Appleton - Hartree formula. Consider a plane EM wave traveling in the X direction of an orthogonal system of axes displayed in Figure 3.1.



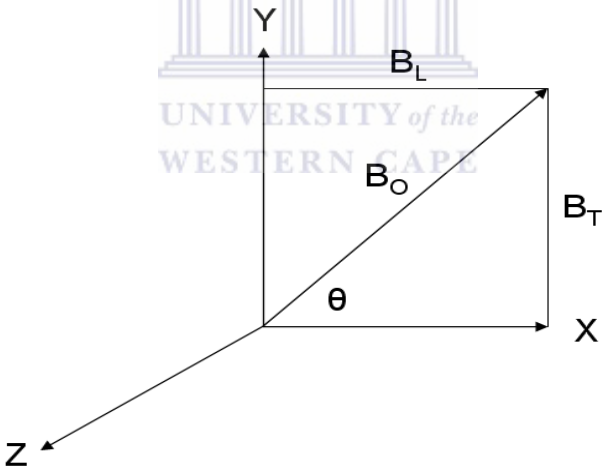


**Figure 3.1:** Geometry showing the system of orthogonal axes X, Y and Z (from Davies, 1990).

In this coordinate frame, the uniform external magnetic field lies in the X-Y plane and makes an angle of θ with the direction of propagation (Davies, 1990; Komjathy, 1997). Thus the final form of the expression describing the complex refractive index $n$ in an ionized magnetic medium (e.g. Davies, 1990; Hunsucker and Hargreaves, 2003) is given by

$$n^2 = 1 - \frac{X}{(1 - iZ) - \left[\frac{Y_T^2}{2(1 - X - iZ)}\right] \pm \left[\frac{Y_T^4}{4(1 - X - iZ)} + Y_L^2\right]^{\frac{1}{2}}} \tag{3.6}$$

Here *n* is the complex refractive index $(\mu - i\chi)$ with $\mu$ as real part and $\chi$ as imaginary part. According to the magneto-ionic theory, a plane polarized EM wave will divide into two characteristic waves. In Equation 3.6 the "+" sign indicates an ordinary wave that approximates the actions of the wave that would propagate in the absence of an imposed magnetic field, whereas the "-" sign indicates an extraordinary wave.

The values of X, Y and Z are dimensionless and each of these is defined as a ratio between the wave frequency and a frequency characteristic of the medium (Hunsucker and Hargreaves, 2003). These dimensionless quantities can also be defined mathematically as

$$X = \frac{\omega_N^2}{\omega^2} = \frac{f_N^2}{f^2} \tag{3.7}$$

$$Y = \frac{\omega_H}{\omega} = \frac{f_H}{f} \tag{3.8}$$

$$Y_L = \frac{\omega_L}{\omega} = Cos\theta \tag{3.9}$$

$$Y_T = \frac{\omega_T}{\omega} = Sin\theta \tag{3.10}$$

where θ is the angle between the direction of propagation and magnetic field. Finally, we have

$$Z = \frac{\omega_C}{\omega} \tag{3.11}$$

The additional symbols in Equations 3.7 to 3.11 are defined as follows: $\omega$ (radian.s$^{-1}$) is the angular frequency of the propagated EM wave $f$ (Hz); $\omega_C$ (radian.s$^{-1}$) is the angular collision frequency between electrons and heavier particles and $\omega_N$ is the angular plasma frequency

with $\omega_N^2 = \frac{Ne^2}{\varepsilon_0 m_e}$ where $N$ is the electron concentration ($m^{-3}$), $\varepsilon_0$ = 8.8542 x $10^{-12}$ $\frac{F}{s}$ is the permittivity of free space, where the electron mass is $m_e$ = 9.11 x $10^{-31}$ kg, and the electron charge is $e$ = 1.6 x$10^{-19}$ Coulomb. Also $\omega_H$ is the angular cyclotron frequency expressed as $\omega_H = \frac{B_0|e|}{m}$ (radian.$s^{-1}$) with EM field strength $B_0$ (Wb.$m^{-2}$), $\omega_L$ is the longitudinal angular frequency given by $\omega_L = \frac{B_0|e|}{m}Cos\theta$ (radian.$s^{-1}$) and also $\omega_T$ is the transverse angular frequency given by $\omega_T = \frac{B_0|e|}{m}Sin\theta$ (radian.$s^{-1}$). When collisions are insignificant (e.g. in the E and F regions), then $Z \approx 0$, and so Equation 3.6 takes the following form:

$$n^2 \cong \mu^2 = 1 - \frac{2X(1-X)}{2(1-X) - Y_T^2 \pm \left[Y_T^4 + 4(1-X)^2 Y_L^2\right]^{\frac{1}{2}}} \tag{3.12}$$

On the other hand, when the magnetic field is negligible (i.e. $Y << 1$) the complex refractive index, $n^2$ takes the form:



$$n^2 = (\mu - i\chi)^2 = 1 - \frac{X}{1 - iZ} \tag{3.13}$$

When both collisions and magnetic field effects are insignificant we have

$$\mu^2 = 1 - X = 1 - \left(\frac{f_N}{f}\right)^2 = 1 - k\frac{N}{f^2} \tag{3.14}$$

where $k$ = 80.5, when $N$ is the electron concentration ($m^{-3}$) as above and $f$ is the frequency (Hz) of the propagating wave.

### 3.4.3 Properties of the Appleton formula

We begin the discussion of the properties of the Appleton formula with Equation (3.14). Since the square of the refractive index is less than unity and seeing as $\mu$ has to be real for the wave to propagate, it can be concluded that $\mu$ must lie between 0 and 1. Following that

first point, it is also worth noting that for a given frequency, the refractive index decreases with increasing electron concentration and that, for a given electron concentration, the refractive index decreases with decreasing frequency. For small electron concentrations, the refractive index is effectively independent of the wave frequency ( $f_N \ll f$ ).

Consider a radio wave which is incident at an angle $\varphi_0$ on a planar layer with increased electron concentration, and then penetrates into that layer. Hence the wave normal (direction of the $\vec{k}$ ) changes according to Snell's Law:

$$\mu Sin\varphi = \mu_0 Sin\varphi_0 \tag{3.15}$$

where $\varphi$ is the angle between the wave normal and the perpendicular to the surfaces of constant refractive index $\mu$, $\mu_0$ and $\varphi_0$ are corresponding values at the base of the layer, that is, $\mu_0 = 1$.

Total reflection will occur for an angle of $\varphi = 90°$:



$$\mu_r = Sin\varphi_0 \text{, where } \mu_r = \frac{\mu}{\mu_0} \text{ .} \tag{3.16a}$$

Hence for reflection in the case of vertical propagation ( $\varphi_0 = 0$) we have:

$$\mu_r = 0 \text{ .} \tag{3.16b}$$

Therefore, from Equations 3.14 to 3.16b, vertical reflection happens when the critical frequency $f_N$ equals the wave frequency $f$ . For this reason, only when the wave frequency exceeds the maximum critical frequency of the layer will the wave penetrate the layer. The expansion of the Appleton-Hartree formula (Equation 3.12, when collisions are negligible) into series up to the 4th inverse power of frequency $\left(\frac{1}{f^4}\right)$ according to e.g. (Bassiri and Hajj, 1993; Brunner and Gu, 1991) yields:

$$n \cong 1 - \frac{1}{2}X \pm \frac{1}{2}XY|Cos\theta| - \frac{1}{8}X^2 - \frac{1}{4}XY^2(1+Cos^2\theta) \quad (3.17)$$

In Equation 3.17 it is obvious that the 2nd and 4th terms are functions involving only the maximum electron density and frequency, unlike the 3rd and 5th terms that are functions of the maximum electron density, the frequency and the magnetic field strength. Komjathy (1997) on the other hand showed that the contribution of the 3rd, 4th and 5th terms to the error budget of determination of the refractive index are 3, 5, and 6 orders of magnitude less than the 2nd term when assuming normal incidence.

Typical values for the F2 layer maximum electron density and magnetic field strength are on the order of $N = 10^{12}\left(\frac{1}{\mathrm{m}^3}\right)$ and $B_0 = 5.0 \times 10^{-5}\left(\frac{\mathrm{Wb}}{\mathrm{m}^2}\right)$ respectively. The interested reader is referred to Komjathy (et al. 1997) for the concise computation of the error budget of the refractive index.



As soon as both collisions and magnetic field are insignificant, then only the 1st and 2nd terms in Equation (3.17) are considered. Nevertheless, to allow the calculation of the phase refractive index of the ionosphere, appropriate for the carrier phase observations, we obtain:

$$n_{ph} \cong 1 - \frac{40.3N}{f^2} \quad (3.18)$$

### 3.4.4 Computation of Group Refractive Index

A pseudo-range observation suitable for the group refractive index is defined according to Langley (1996) as:

$$n_{gr} = n + f\frac{dn}{df} \quad (3.19)$$

Thus invoking the value of phase refractive index $n = n_{ph}$ in Equation (3.18) will lead to:

$$\frac{dn}{df} = \frac{dn_{gr}}{df} = \frac{d}{df}\left(1 - \frac{40.3N}{f^2}\right)$$

$$\frac{dn}{df} = \frac{dn_{gr}}{df} = -40.3N\frac{d}{df}\left(\frac{1}{f^2}\right)$$

$$\frac{dn}{df} = \frac{dn_{gr}}{df} = -2(-40.3N)\left(\frac{1}{f^3}\right) \tag{3.20}$$

After the derivation as seen above, Equation (3.19) takes on a new structure and is known as the group refractive index:

$$n_{gr} = 1 - \frac{40.3N}{f^2} + 2\frac{40.3N}{f^2}$$

$$n_{gr} = 1 + \frac{40.3N}{f^2} \tag{3.21}$$

It can be seen from Equations (3.18 and 3.21) that the group and phase refractive indices deviate from unity with opposite sign.



### 3.4.5 Group and phase velocity

In radar and many other radio experiments, pulses of radio waves are used. These pulses can be considered as a signal from a transmitter that generates a constant frequency and that is switched on for a short time. To study the propagation of these pulses it is helpful to introduce the concept of group and phase velocity (Budden, 1985). Using Equation (3.21), it follows that the group velocity, $v_{gr}(m/s)$, of propagating signals is given by:

$$v_{gr} = \frac{c}{n_{gr}} \cong \frac{c}{1 + \left(\frac{40.3N}{f^2}\right)}$$

$$v_{gr} \cong c\left(1 - \frac{40.3N}{f^2}\right) \tag{3.22}$$

Applying a similar approach (as seen above) to Equation (3.18), it follows that the phase velocity, $v_{ph}(m/s)$, of propagating signals is given by:

$$v_{ph} = \frac{c}{n_{ph}} \cong \frac{c}{1 - \left(\frac{40.3N}{f^2}\right)}$$

$$v_{ph} \cong c\left(1+\frac{40.3N}{f^2}\right) \tag{3.23}$$

Here $c$ is the speed of light in free space ($3.0\times10^8$ m.s$^{-1}$) in both Equations (3.22 and 3.23). The strict requirement of causality means that $n_{gr} > 1$ and $v_{gr} < c$, from which it follows that $N$ is always > 0. As a consequence of the different velocities a group delay and phase advance occurs, and will be discussed in next sub section.

### 3.4.6 Ionospheric group delay and phase advance

In view of the fact that the ionosphere is a dispersive medium (Ratcliffe, 1959) it exerts noteworthy influence on the propagation of EM waves such as GNSS signals. The signals from the satellite experience time delay and phase advance when traversing the ionosphere due to the interaction with the free electrons. The additional time delay introduced by traversing the ionosphere can thus be computed as the difference in the time of flight in the medium, $\Delta t_{ion} = \int_{ion} \frac{ds}{v_{gr}}$, and the time of flight over the same path in the absence of the medium, $\Delta t_0 = \int_{ion} \frac{ds}{c}$. Using the definition of the group index of refraction, $v_{gr} = \frac{c}{n_{gr}}$, then $\delta t_{ion} = \Delta t_{ion} - \Delta t_0 = \frac{1}{c}\int_{ion}[n_{gr} - 1]ds$. Then from Equation (3.21) we have



$$\delta t_{ion} \cong \frac{1}{c}\frac{40.3}{f^2}\int_{ion} N ds \tag{3.24}$$

We define the Total Electron Content as the path integrated electron number density,

$$\text{TEC} \equiv \int_{ion} N ds \tag{3.25}$$

Thus the ionospheric delay is

$$\delta t_{ion} \cong \frac{40.3TEC}{cf^2}$$

Here the acronym TEC stands for Total Electron Content and is measured in TEC Units (TECU), where 1 TECU $= 10^6 \frac{electrons}{m^2}$ along the signal path. It is conventional to measure the delay in distance units, so that $d_{ion} = c\delta t_{ion}$ giving

$$d_{ion} \cong 40.3\frac{TEC}{f^2} \tag{3.26}$$

The phase advance introduced by traversing the ionosphere can be computed similarly as the difference in the phase developed while traversing the medium, $\Delta\phi_{ion} = \int_{ion} \omega dt_{ion} = \int_{ion} \omega \frac{ds}{v_{ph}}$, and the phase developed over the same path in the absence of the medium, $\Delta\phi_0 = \int_{ion} \omega \frac{ds}{c}$. Using the definition of the phase index of refraction, $v_{ph} = \frac{c}{n_{ph}}$, then $\delta\phi_{ion} = \Delta\phi_{ion} - \Delta\phi_0 = \frac{\omega}{c}\int_{ion}[n_{ph} - 1]ds$. Then from Equation (3.18) we have

$$\delta\phi_{ion} \cong -\frac{40.3\omega TEC}{cf^2} \tag{3.27}$$

We have $d_{ion} > 0$, which indicates that the modulated code range shows a delay in time of reception, thus an increase in apparent range. Thus, it is referred to as a group delay. On the other hand we have $\delta\phi_{ion} < 0$, which indicates that phase measurements are shorter than the true range, thus it is advanced by an amount controlled by the signal frequency and electron concentration. Thus, it is referred to as the phase advance. Finally, we note that the phase advance is proportional to the time delay: we have $\delta\varphi_{ion} = -\frac{\omega}{c} d_{ion} = -\omega\delta t_{ion}$.



## 3.5 MAGIC application over South Africa

### 3.5.1 Introduction

The global US_TEC assimilation algorithm using the IRI95 ionospheric model and based on the ionospheric imaging package called MAGIC was used to specify vertical and slant TEC over the Continental US (CONUS) in near real-time (Araujo-Pradere, et al., 2006, 2007). The main sources of data are dual frequency GPS receivers, from the NGS Continuously Operating Reference Stations (CORS) network. The data are provided in Receiver Independent Exchange Format (RINEX), and are used to construct a four-dimensional electron density model of the ionosphere. Due to South Africa's efforts like the HartRAO

Space Geodesy Programme, work is proceeding towards the establishment and increase of GNSS receiver installations across the SADC region (Combrink, 2006) as part of the International GNSS Service (IGS) service. These will be of particular interest for ionospheric and geodynamic studies which focus on a geographically larger area (Combrink, 2006). Other efforts included collaborations between the Geophysics Division of the Council for GeoScience, Council for Scientific Industrial Research (CSIR) and the HartRAO Space Geodesy Programme, for the installation of a new space geodetic observatory (IISGEO) (Fourie, 2007). The new IISGEO will have an enduring differential GNSS receiver network as part of a global network, and data from this will be used for studying ionosphere electron content, crustal deformation and atmosphere water vapour content. Given that the modelling of the ionosphere over South Africa is still in a pioneering phase, it became evident that the effort to develop and investigate the performance of a GPS TEC model such as MAGIC for the region over the Southern African using local GPS data was worthwhile.

Ionospheric studies over South Africa, principally due to data from ionosondes, have been going on for more than several decades now. At present the South African Ionosonde Network consists of four ionosonde stations, all of which are digisondes, spread geographically across South Africa, located at Grahamstown (33.3°S, 26.5°E), Louisvale (28.5°S, 21.2°E), Madimbo (22.4°S, 30.9°E) and Hermanus (34.4°S, 19.2°E). The first three ionosonde stations named above are DPS-4 models, with Grahamstown in service since 1996 and the other two since the year 2000. The Hermanus ionosonde station is the latest DPS-4D model, and installation was concluded in July 2008; this is the first DPS-4D operational in the field anywhere in the world. The foremost area of research for the network has been the modelling of bottomside ionospheric parameters through the use of neural networks (McKinnell and Poole, 2000, 2004; Oyeyemi and Poole, 2004; Oyeyemi, 2005; Oyeyemi, et al., 2007; Habarulema, et al., 2007; Habarulema, et al. 2009a, b; Habarulema, 2010). The South African Ionosonde network operates continuously on a vertical incidence program, with two of the ionosonde stations, namely Grahamstown and Hermanus set at a 15 minute resolution, whereas the other two, Louisvale and Madimbo, are set at a 30 minute resolution.

Of late, the ionospheric scientific community of South Africa has been undertaking efforts to study the dynamics and variations in the ionosphere over Southern Africa, as discussed previously (Cilliers, et al., 2004; Ngcobo et al., 2005; Moeketsi et al., 2007b, c; Opperman, et al., 2007a, McKinnell and Poole, 2000, 2004; Habarulema, et al., 2007; Habarulema, et al.,

2009a, b,; Habarulema, 2010; Okoh, 2009) with the use of the GNSS based studies as a new method. This new method serves as an addition to other techniques used to study the ionosphere, including ionosondes, incoherent scatter radars and satellites. One of the significant ionospheric parameters that can be derived from GNSS data is the TEC, which provides an indication of ionospheric changeability, and can be considered as the measure of ionisation in the ionosphere (Habarulema, et al., 2007). As described in Chapter 2, the propagation of radio signals in the Earth's atmosphere is dominantly affected by the ionosphere due to its dispersive nature (Ratcliffe, 1959).

As outlined earlier in this chapter, there will be the ionosphere delay on the GPS navigation signals of L1 = 1575.42 MHz and L2 = 1227.6 MHz as observed by the global system of ground based dual frequency GPS receivers. The received navigation signals can be then in turn be used to provide input for a technique to determine high resolution spatial and temporal ionospheric TEC at a local and intercontinental level (Mannucci, et al., 1998; Jakowski, et al., 1999; Schaer, 1999; Komjathy and Langley, et al., 1996; Opperman, et al., 2007a; Moeketsi, et al., 2007b, c; Yizengaw, et al., 2005). Advances in local and international space physics research and associated fields of study have the need for ionospheric parameter information with a more enhanced spatial and time resolution than was previously possible with the existing ionosonde network (Opperman, 2007). It is evident after decades of ionospheric research that the properties of this layer (the ionosphere) in the Earth's atmosphere is highly variable and depends on numerous factors such as local time, geographical location, season and solar cycle (Tsurutani, et al., 2005; Fedrizzi, et al., 2005; Moeketsi, et al., 2007b, c). Recently, it was found that monitoring TEC through the use of the GNSS network can be an important addition to space weather monitoring (Jakowski, et al., 2001). Thus, this new method to study the ionosphere has received extensive international attention and is presently widely implemented operationally by numerous institutions and facilities to supply local and international ionospheric maps, with better time and spatial resolution than previously possible with sparingly distributed ionosonde networks (Opperman, et al., 2007a).

### 3.5.2 Used SA GNSS network

In this sub section of Chapter 3 of the thesis, we clarify and give a concise description of South Africa's GNSS network of stations, which are the sources of the date that is used in this study. The following two pages contain the table listing the 43 South African GNSS stations used in this study.

| Station Name | Station Code | Geographical Latitude (◦) | Geographical Longitude (◦) |
|---|---|---|---|
| Aliwal North | ANTH | -30.40 | 26.42 |
| Benoni | BENI | -26.11 | 28.20 |
| Bethlehem | BETH | -28.14 | 28.20 |
| Bisho | BISO | -32.51 | 27.25 |
| Bloemfontein | BFTN | -29.06 | 26.17 |
| Brits | BRIT | -25.38 | 27.46 |
| Bronkhorstspruit | BRNK | -25.48 | 28.43 |
| Beaufort West | BWES | -32.20 | 22.34 |
| Calvinia | CALV | -31.28 | 19.45 |
| Cape Point | CPNT | -34.21 | 18.29 |
| Cape Town | CTWN | -33.57 | 18.28 |
| De Aar | DEAR | -30.39 | 23.59 |
| Durban | DRBN | -29.51 | 31.01 |
| East London | ELDN | -33.02 | 27.49 |
| Ermelo | EMLO | -26.29 | 29.59 |
| Ellisras | ERAS | -23.41 | 27.41 |
| Groblersdal | GDAL | -25.09 | 29.24 |
| George | GEOR | -34.00 | 22.22 |
| Greytown | GREY | -29.04 | 30.34 |



**Table 3.1:** Table lists the geographical coordinates of South Africa's dual frequency GNSS receivers that were used in this thesis.

| Station Name | Station Code | Geographical Latitude (◦) | Geographical Longitude (◦) |
|---|---|---|---|
| Grahamstown | GRHM | -33.19 | 26.30 |
| Graaff Reinet | GRNT | -32.14 | 24.32 |
| Heidelberg | HEID | -26.30 | 28.22 |
| Kuruman | KMAN | -27.27 | 23.25 |
| Krugersdorp | KRUG | -26.04 | 27.45 |
| Kroonstad | KSTD | -27.39 | 27.14 |
| Langebaan | LGBN | -32.58 | 18.09 |
| Ladysmith | LSMH | -28.33 | 29.46 |
| Malmesbury | MALM | -33.27 | 18.43 |
| Middelburg | MBRG | -25.46 | 29.27 |
| Queenstown | QTWN | -31.54 | 26.55 |
| Springbok | SBOK | -29.40 | 17.52 |
| Scottsburgh | SCOT | -30.17 | 30.45 |
| Steelpoort | SPRT | -24.40 | 30.11 |
| Stanger | STAN | -29.20 | 31.17 |
| Stellenbosch | STBS | -33.50 | 18.50 |
| Sutherland | SUTH | -32.22 | 20.48 |
| Thohoyandou | TDOU | -23.04 | 30.23 |
| Temba | TEMB | -25.23 | 28.16 |
| Ulundi | ULDI | -28.17 | 31.25 |
| Umtata | UMTA | -31.32 | 28.40 |
| Upington | UPTA | -28.24 | 21.15 |
| Vereeniging | VERG | -26.39 | 27.54 |
| Worcester | WORC | -33.38 | 19.26 |



**Table 3.1, continued:** Table lists the geographical coordinates of South Africa's dual frequency GNSS receivers that were used in this thesis.

The GNSS network of South Africa is made up of two GPS networks, that is:

i. The SADC GPS network
ii. Trignet Network

The first of the GPS networks named above forms part of the IGS network and is managed locally by HartRAO (http://geodesy.hartrao.ac.za/). The second network is managed by the Chief Directorate of Surveys and Mapping (Combrink, et al., 2004). Due to a growing interest in space weather studies in the last decade in South Africa, efforts have been undertaken by the managers of the SADC and Trignet GPS networks to add more ground based dual frequency GNSS receivers to the existing network throughout South Africa. The information for the stations from which the date which is used for the thesis is given in Table 3.1, which showcases the station name, code and geographical coordinates; a graphical illustration showing the locations of the stations is given in Figure 3.2.



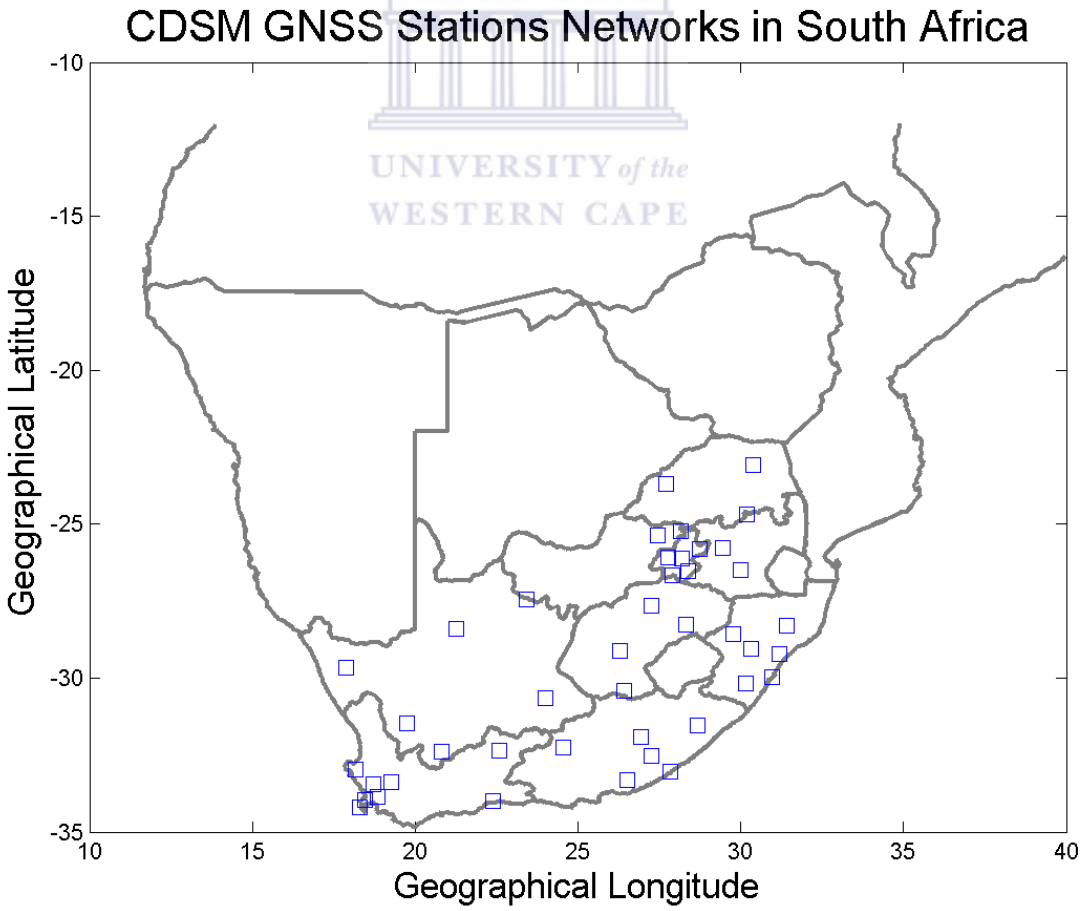


**Figure 3.2:** Geographical map that depicts the locations of South Africa's GNSS network.

The data from the 43 South African dual frequency GNSS receivers, which has a sampling rate of 30s, was used in this thesis study as input to the MAGIC code, as described in this chapter, to compute ionospheric TEC over the South African region. The data used was obtained from the South Africa CDSM Trignet data server (ftp://ftp.trignet.co.za). Figure 3.3 shows an example of a regional TEC map produced using the SA modified version of the MAGIC model with data obtained from the South African GPS networks. This estimation of TEC is for 11:45:00 UT on 29 October 2003, and it shows that TEC values are higher nearer to the equatorial region.

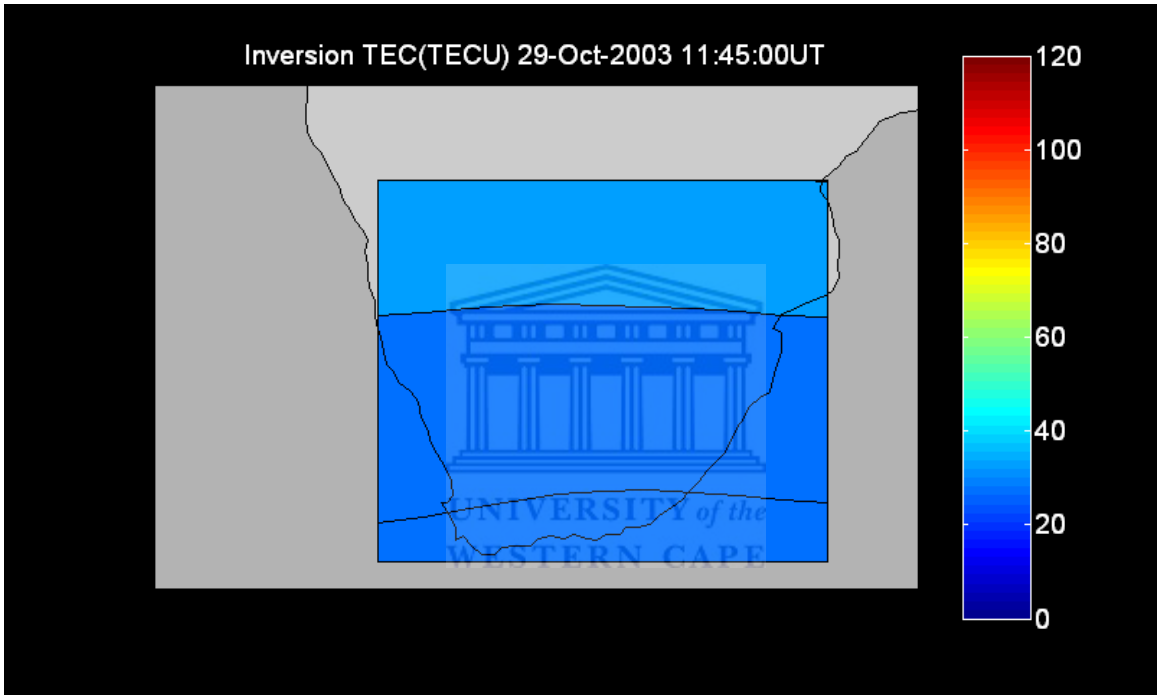


**Figure 3.3:** Depiction of a regional TEC map as at 11:45:00 UT on 29 October 2003 (Halloween Storm) over South Africa, produced using modified Version of the MAGIC.

## 3.6 Summary

This chapter provided a concise description of the ionospheric modelling technique known as MAGIC (Spencer, et al., 2004; Araujo-Pradere, et al., 2006, 2007; Minter, et al., 2007), adopted as the main tool in this study. It started with a concise description of global and local ionospheric TEC models using GNSS. The method behind the MAGIC Ionospheric modelling technique was discussed, together with the Kalman filter assimilation technique. The physics behind the MAGIC package and propagation of radio waves through the ionosphere were amongst other sub topics that were discussed. Finally the chapter concludes

with a discussion on the MAGIC application for TEC calculation over South Africa using data from South Africa's GNSS networks.

The next chapter will focus on the discussions of the observations of TEC patterns during Post Solar Minimum and Maximum periods over South Africa as estimated by the MAGIC package.

# Chapter 4

# ANALYSIS OF MAGNETIC STORMS EFFECTS ON TEC OVER SOUTH AFRICA

## 4.1 Introduction

In this chapter the focus will be on the investigation of the effect of mid-latitude magnetic storms on TEC over South Africa for Solar Cycles 23 and 24. It starts with what is being investigated and how it will be done, as well as the geomagnetic events chosen for this study. The chapter then continues to discuss the description of the pattern of Reference Time Series and Storm Time Series TEC over South Africa during Post Solar Maximum and Post Solar Minimum periods. To conclude the chapter, the difference and similarities among the Reference Time Series and among the Storm Time Series for Post Solar Maximum and Post Solar Minimum periods will be discussed.



## 4.2 Selection of Storm Periods

### 4.2.1 Geomagnetic Index, Dst

Events leading to geomagnetic storms always involve the flow of energy in the Sun-Earth direction, and in analyses of the geoeffectiveness of solar events it is common to continue the chain from Earth back all the way to the Sun (Zhang, et al., 2007). However, forecasts of geomagnetic conditions which are solely based on solar events can lead to false alarms. Consequently, geomagnetic indices such as the Dst and Kp, amongst others, are universally used to determine the level of geomagnetic activity arising from solar events. For this study, we only consider and use the Dst index for the selection of storm events. As discussed previously, the Dst index is a measure of the horizontal component of the Earth's magnetic field at low-to mid-latitude regions. Because it is a representation of the deviation of the horizontal magnetic component at the equator from a magnetically quiet day, it is commonly considered as a measure of the ring current.

Variations within the typical magnetic storm consists of four phases, namely, a sudden storm commencement, an initial (positive) phase, a main (negative) phase and a recovery phase (Davies, 1990). In terms of the Dst index, the storm is represented by magnetic activity that fluctuates from the positive northward horizontal magnetic field component to the negative northward horizontal magnetic field component throughout a given period. More negative values of the index correspond to a more powerful magnetic storm. Therefore magnetic storms can be classified from the various Dst index values (Pirog, et al., 2006), as can be seen in Table 4.1.

| Dst Index | Storm Type |
|---|---|
| -50 nT < Dst < -30 nT | Weak |
| -100 nT < Dst < -50 nT | Moderate |
| -200 nT < Dst < -100 nT | Intense |
| Dst < -200 nT | Super |

**Table 4.1:** Table listing the categorization of magnetic storms based on the Dst geomagnetic index.

In the selection process for the Post Solar Maximum and Post Solar Minimum period storms, an effort was made to choose clearly isolated geomagnetic storm events. Two criteria were thus applied for the selection of storm events. First, there had to be at least seven days before the storm event when the Dst index was relatively quiet. Second, the threshold for a storm event was chosen somewhat arbitrarily to be a minimum value of Dst ≤ -50 nT. Thus we only consider isolated events with minimum Dst ≤ -50 nT for this study. A given storm was followed until Dst returned to the pre-storm level. Thus, a single storm can in fact encompass several periods of Dst ≤ −50 nT, mainly throughout high solar activity events (Uwamahoro, 2011).

The Dst index data were obtained from the World Data Centre for Geomagnetism, Kyoto (http://wdc.kugi.kyoto-u.ac.jp/index.html). The entire span of Dst data from January 2003 to October 2012 was examined for events that fit the criteria given above. For this research study intervals were selected for periods in years 2003 (October), 2005 (April and May), 2007 (November), 2008 (March), 2009 (July), 2010 (March and April), 2011 (September)

and 2012 (March). These storms cover Post Solar Maximum period for solar cycle 23 and the Post Solar Minimum period of solar cycle 24.

### 4.2.2 Statistical and Mathematical Models

It is observed that there is a strong diurnal cycle in the TEC measured over South Africa, which dominates all other effects on TEC. This daily pattern, which is notably constant, is driven by solar photoionization processes during the day, and by the subsequent relaxation pattern after direct insolation ceases as well. Thus, in order to observe the effect of magnetic storms on TEC, a reference is required.

It will be recalled that the first criteria for the selection of storm events was a period of at least seven days before the storm event when the Dst index was relatively quiet. For each storm event, the TEC values for the seven days preceding the storm event were used to construct the TEC Reference Time Series for that storm. Then each storm event was followed from the day of the initial strong southward bay until the day

i) at which the Dst index returned to the level of baseline Dst activity
ii) and was relatively quiet thereafter.



Table 4.2, gives a summary of the geomagnetic events chosen for this study, including relevant information such as year, month, Reference Time Series interval, Storm Time Series interval, and the phase within the Solar Cycle.

| Event | Year | Reference Interval | Storm Interval | Solar Cycle |
|---|---|---|---|---|
| 1 | 2003 | 22-28 Oct | 29-31 Oct | Post Solar Max |
| 2 | 2005 | 21-28 Apr | 07-16 May | Post Solar Max |
| 3 | 2007 | 12-18 Nov | 19-23 Nov | Post Solar Max |
| 4 | 2008 | 01-07 Mar | 08-10 Mar | Solar Min |
| 5 | 2009 | 15-21 Jul | 22-24 Jul | Post Solar Min |
| 6 | 2010 | 29 Mar-04 Apr | 05-10 Apr | Post Solar Min |
| 7 | 2011 | 02-08 Sept | 09-14 Sept | Post Solar Min |
| 8 | 2012 | 01-08 Mar | 09-11 Mar | Post Solar Min |

**Table 4.2:** Summary of geomagnetic events chosen for this study, specifying the year, month, Reference Time Series interval, Storm Time Series interval and phase within the Solar Cycle.

In this subsection, statistical and mathematical methods were used to construct the three types of time series needed for this research study. For each of the events listed in Table 4.2 above a TEC Reference Time Series (RTEC) was created. The RTEC time series is just the average over the seven days (and eight days for events 2 and 8) of the reference period preceding the storm event, and thus is one day in length. We have already used MAGIC to compute the TEC map, $TEC(yr, DOY, t_k)_{ij}$ on a given day of year, $DOY$ at a time of day given by $t_k = k-1 \ast 15\min$, at the location $ij$ , where $i$ labels the longitudinal coordinate and $j$ labels the latitudinal coordinate. Consequently RTEC time series for year $yr$ is given by Equation 4.1 as

$$RTEC(yr, t_k)_{ij} = \frac{1}{n} \sum_{day_l=1}^{n} TEC(day_l, t_k)_{ij} \tag{4.1}$$

here the index $day_l$ runs over the number of days of the reference period.

At the same time that the daylong RTEC time series is being calculated, the Root Mean Squared (RMS) variation of the reference days about that series is also computed. This deviation time series DEVTEC will be used to assess the significance of features on the storm

event TEC map, as discussed below. The description above can be mathematically expressed and is shown in Equation 4.2

$$DEVTEC(yr,t_k)_{ij} = \sqrt{\frac{1}{n-1}\sum_{day_l=1}^{n} TEC(day_l,t_k)_{ij} - RTEC(yr,t_k)_{ij}^{\,2}} \tag{4.2}$$

here all the other symbols in Equation 4.2 have been previously defined.

With the reference TEC time series RTEC in hand; we can now determine the effect of the storm on TEC by comparing the TEC time series during the storm with the reference TEC time series RTEC. The Storm Time Series is constructed as the difference between the TEC time series and the RTEC time series. We define the Difference TEC Time Series, ΔTEC, in Equation 4.3, where $TEC(yr,DOY,t_k)_{ij}$ is defined on page 51

$$\Delta TEC(yr,DOY,t_k)_{ij} = TEC(yr,DOY,t_k)_{ij} - RTEC(yr,t_k)_{ij}. \tag{4.3}$$

The primary goal of the thesis is the description and comparison of the ΔTEC time series. Because of the statistical nature of the reference time series RTEC, it is meaningful to ask: Is the difference time series $\Delta TEC(yr,DOY,t_k)_{ij}$ significant? To answer this question, we compare ΔTEC to $DEVTEC(yr,t_k)_{ij}$ by constructing the ratio of those two series, which we term the Ratio TEC time series, as can be seen in Equation 4.4

$$Ratio(yr,DOY,t_k)_{ij} = \frac{\Delta TEC(yr,DOY,t_k)_{ij}}{DEVTEC(yr,t_k)_{ij}}. \tag{4.4}$$

Values of $Ratio(yr,DOY,t_k)_{ij} \le 1$ suggest that the storm effect $\Delta TEC(yr,DOY,t_k)_{ij}$ is not significant, whereas if $Ratio(yr,DOY,t_k)_{ij} > 1$ the implied storm effect is more likely to be significant. Analysis of the effect of magnetic storms on TEC using the $\Delta TEC(yr,DOY,t_k)_{ij}$ and $Ratio(yr,DOY,t_k)_{ij}$ time series will be discussed in the subsequent section of this thesis.

## 4.3 Variations of Reference TEC patterns over South Africa

The previously discussed MAGIC package was used to compute maps of spatiotemporal TEC density over South Africa from the input GPS data for the reference and storm time intervals. These maps, which cover approximately 15° of latitude and approximately 20° of longitude, with spacing of 2° in longitude and 3° in latitude, are made at 15 minute time intervals. From these maps we construct the RTEC, ΔTEC and Ratio time series as described above. It is important to note that each of these time series are three-dimensional, having also extent in latitude and longitude. Subsequent subsections will discuss the spatiotemporal ionospheric TEC maps over South Africa.

### 4.3.1 TEC over South Africa during Post Solar Maximum for 2003 Reference Day



In order to properly describe the effects of mid-latitude magnetic storms on RTEC over South Africa, it is necessary to provide the context for those effects by describing the pattern of RTEC in the absence of mid-latitude magnetic storms. The Dst index for seven days, 22-28 October 2003, shown in the left of Figure 4.1, was relatively quiet; based on the Dst index for those days, no magnetic storms took place. Hence, those days were used to form the October 2003 Reference Day, by the process previously described. Note that the 2003 Reference Day and 2003 Storm fall within the Post Solar Maximum phase of solar cycle 23.

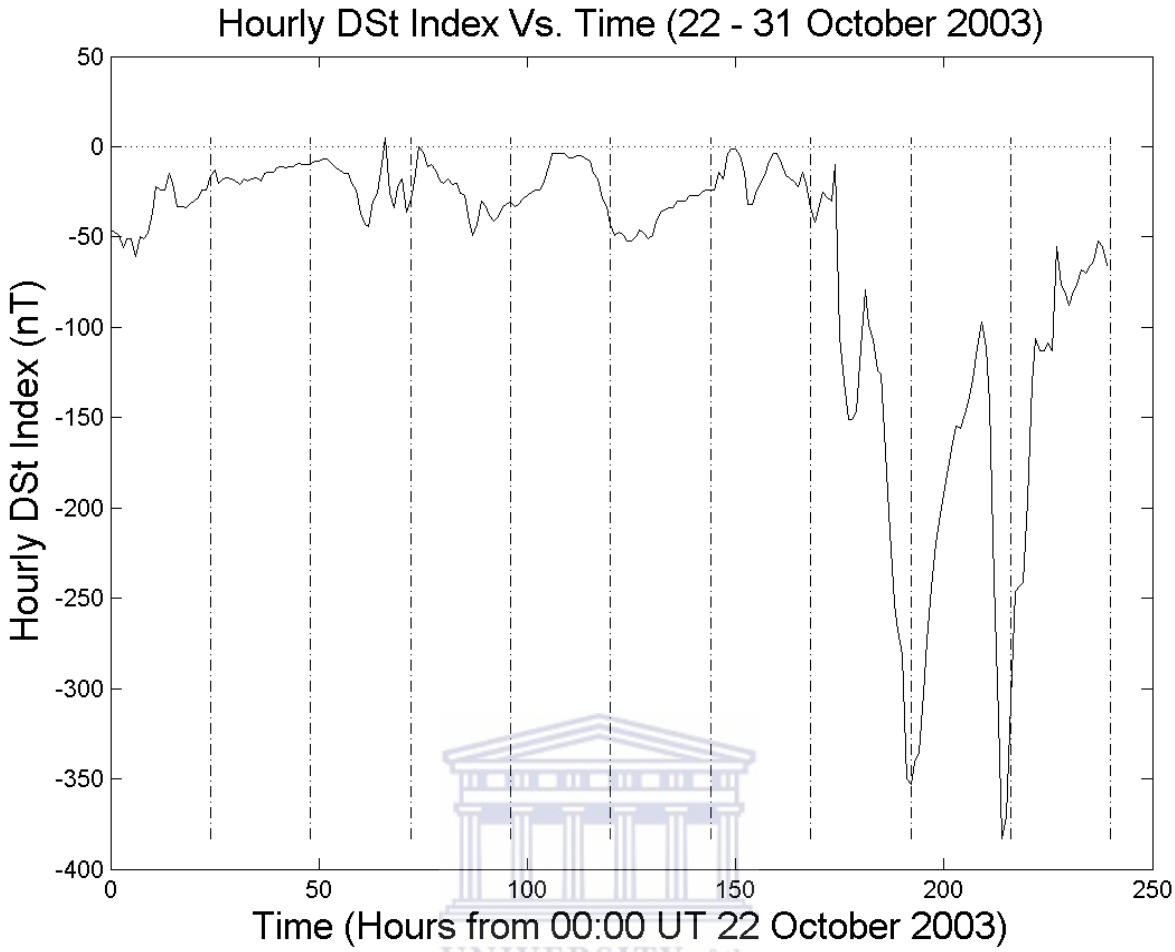




**Figure 4.1:** Graphical representation of the 2003 magnetic storm (Halloween Storm) in terms of Dst geomagnetic index. The 2003 Storm also experienced two successive negative pulses. The dash line marker represents a 24 hour day (data sourced from http://wdc.kugi.kyoto-u.ac.jp/index.html).

What follows is an introductory discussion of the RTEC maps that form the basis for this thesis. Figure 4.2 with panels a)-d) is a graphical representation that visualizes how RTEC fluctuates spatially and temporally over South Africa's ionosphere for the 2003 Reference Day. The four panels each show one of the 96 maps from the 2003 Reference Day. The UT times in Figure 4.2 are 03:45 UT (~ sunrise; panel a), 10:15 UT (~ solar noon; panel b), 16:30 UT (~ sunset; panel c) and 22:00 UT (~ solar midnight; panel d).

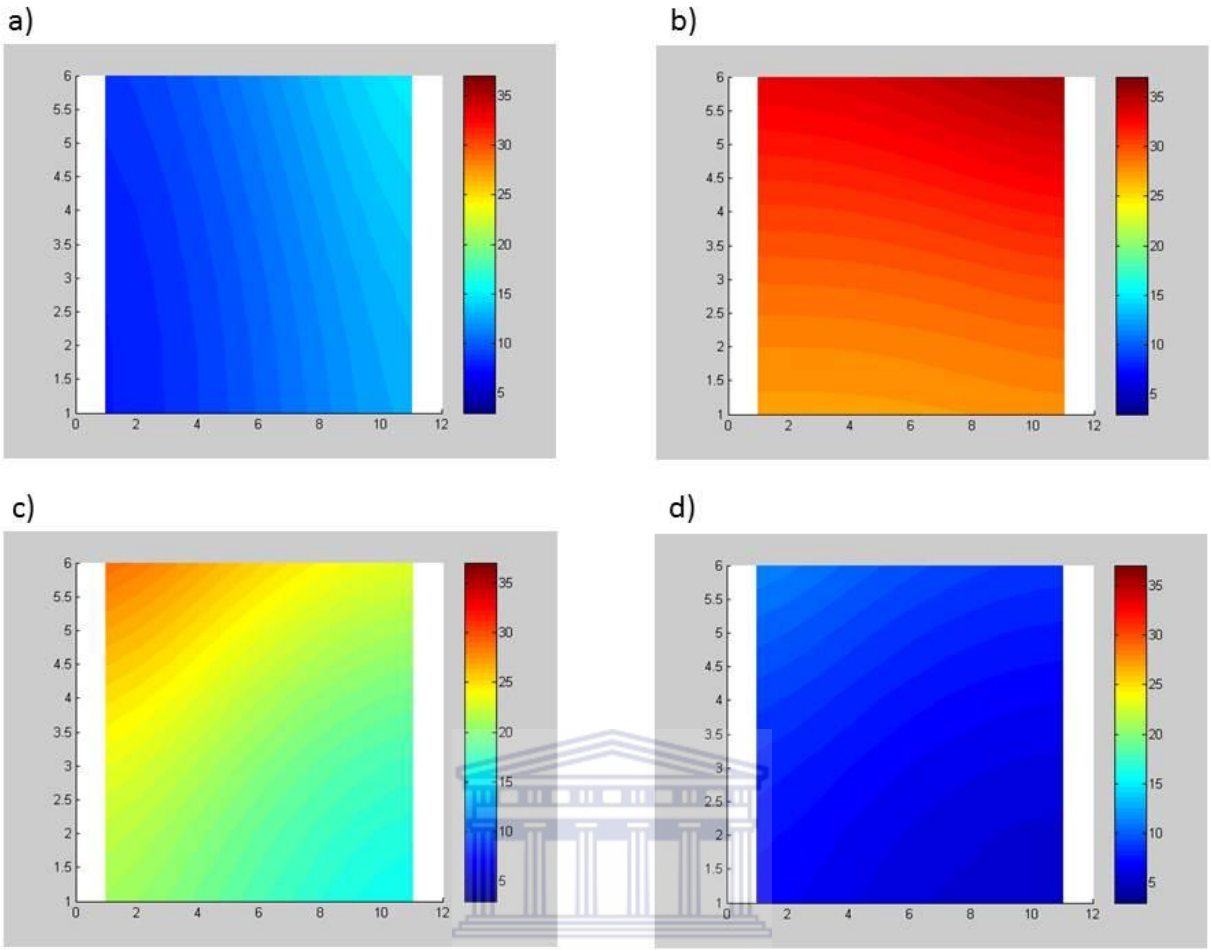




**Figure 4.2:** A graphical visualization that illustrates TEC spatiotemporal maps over the ionosphere of South Africa for the 2003 Reference Day. The UT times for panels a)-d) are 03:45 UT (~ sunrise), 10:15 UT (~ solar noon), 16:30 UT (~sunset) and 22:00 UT (~ solar midnight), respectively.

The 2003 Reference Day starts at midnight UT, near the end of the night-time interval which is dominated by recombination. At this time, the undisturbed level of RTEC for the Reference Day was relatively low because no photoionization has occurred since sunset. The RTEC over South Africa is relatively uniformly distributed, but is slightly higher in the northwest as that is the region that last received insolation, and thus most recently had the creation of free electrons by the photoionization process. With the onset of sunrise at 03:45 UT (05:45 South Africa Standard Time [SAST]) the solar driven photoionization process will begin to dominate, which will in turn cause an increase in RTEC. Now the spatial pattern of RTEC shifts, with higher values in the northeast. As the day continues and the subsolar point moves across the map window from east to west, the peak RTEC values on the map track the subsolar point with little lag. Solar noon occurs at about 10:15 UT (12:15 SAST). At that time, the values of RTEC reach their maximums, as photoionization overwhelms

recombination during the daytime since the Sun's ultraviolet light is the main source of ionization in the ionosphere, particularly in the low altitude ionospheric layers (D and E region) over the entire dayside. After solar noon, the Sun will begin its descent to sunset at a time of 16:30 UT (18:30 SAST). The peak values of RTEC on the map shift to the northwest, and as the solar zenith angle increases there is a resultant decrease in RTEC over the entire map. After sunset, photoionization ceases to be a factor and recombination again becomes dominant as the time approaches solar midnight.

A useful measure of the net pattern can be formed by constructing the time series of the average of RTEC values over the map. The minimum and maximum average RTEC values for the October 2003 reference period are 3 and 37 TECU respectively. The trend of this average RTEC time series for the 2003 Reference Day is shown in Figure 4.3; the error bars indicate the standard deviation at a given time of the RTEC values across the map from the average value. We see that the average RTEC time series is characterized by four broad intervals: an interval when average RTEC has a roughly constant minimum value, an interval when average RTEC has a high rate of increase, an interval when average RTEC has a roughly constant maximum value, and an interval when average RTEC is decreasing. The intervals of maximum and minimum RTEC for the 2003 Reference Day have durations of about 4 hours and about 3 hours respectively. The rates of increase and decrease of average RTEC for the 2003 Reference Day are about 4.0 and about 3.0 TECU per hour, respectively.

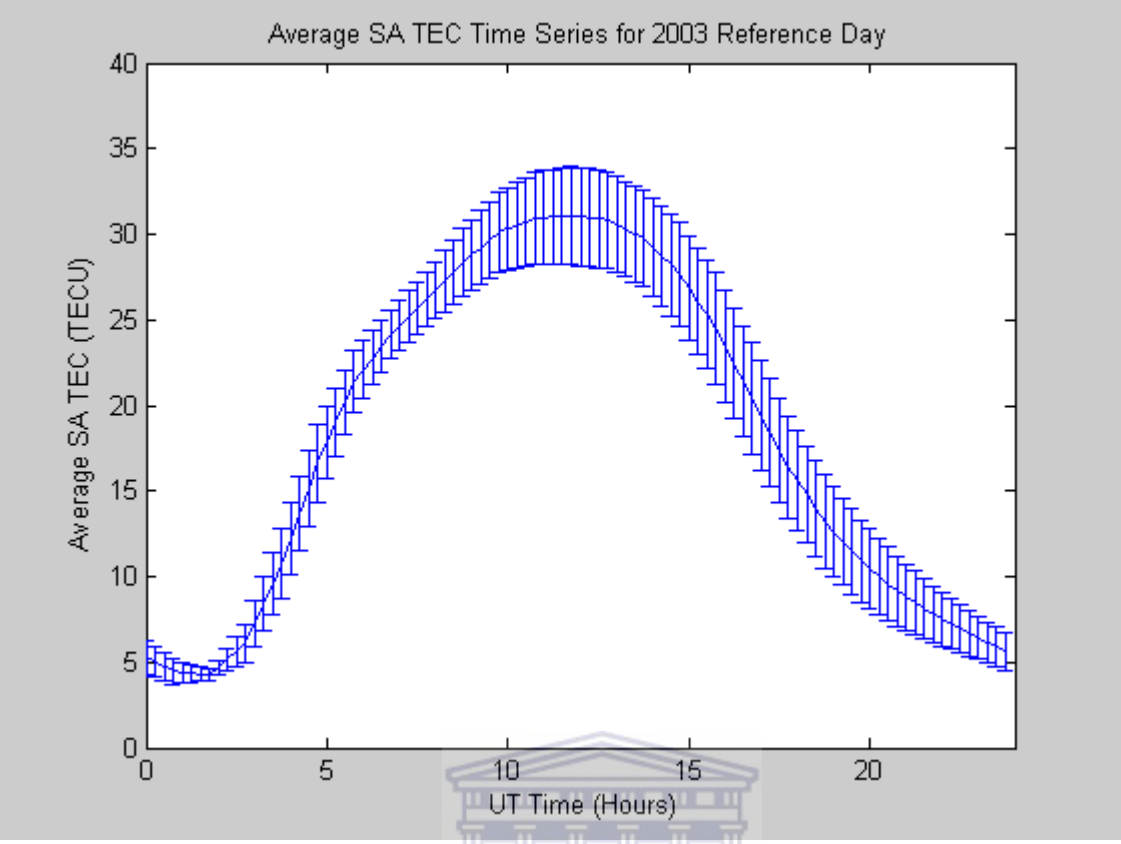


**Figure 4.3:** Depiction of the average South African RTEC Time Series for 2003 Reference Day, where the average value is of the 66 values of RTEC, and the error bars which give the RMS deviation of those 66 values about the mean.



Three other Reference Days chosen for this study also fall within the Post Solar Maximum phase of solar cycle 23, namely for 2005, 2007 and 2008; we note here that 2008 falls during the Solar Minimum, and a 2008 analysis will follow after the 2012 analysis. The Reference Days for those years all follow the same daytime and night-time spatial pattern over South Africa as has been described for the 2003 Reference Day, with low RTEC initially and then progressive increases in RTEC due to solar radiation's energetic photons (sunlight) as solar noon approaches, followed by a return to lower RTEC as solar midnight approaches. The only difference is the amplitude of the RTEC values; the average RTEC values (maximum and minimum RTEC) vary between the Reference Days, as will be discussed in next subsequent section.

### 4.3.2 TEC over South Africa during Post Solar Minimum for 2012 Reference Day

As noted above, in order to properly describe the effects of mid-latitude magnetic storms on RTEC over South Africa, it is necessary to provide the context for those effects by describing the pattern of RTEC in the absence of mid-latitude magnetic storms. The eight days 01-08 March 2012 were relatively calm; based on the Dst index for those days, no storms took place. Hence, those days were used to form the 2012 Reference Day by the process previously described and the graphical representation can be seen in Figure 4.4. The 2012 Reference Day falls within the solar cycle period of Post Solar Minimum. The following description gives the spatiotemporal development of RTEC activity over South Africa during the 2012 Reference Day.

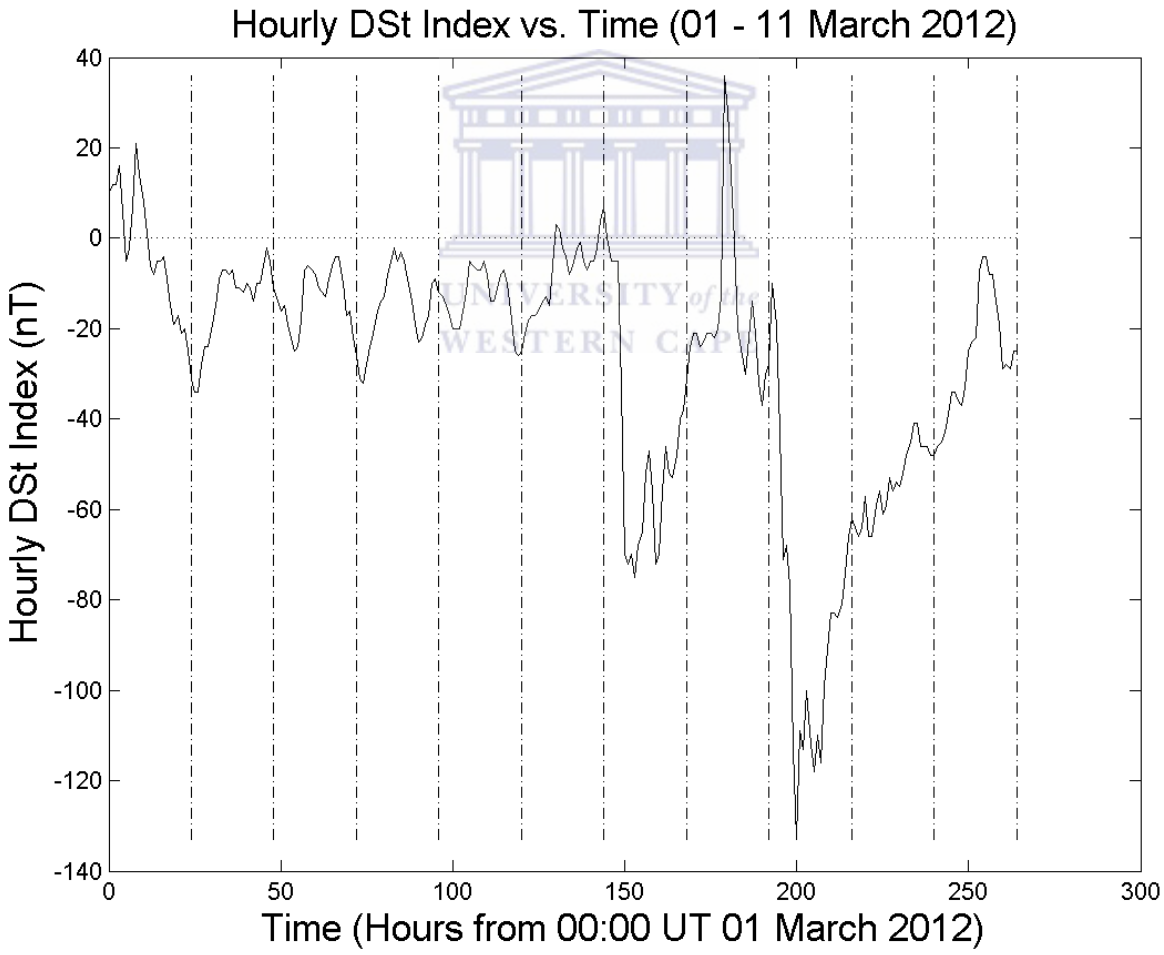


**Figure 4.4:** Graphical representation of the 2012 magnetic storm in terms of Dst geomagnetic index. The 2012 Storm has a tripolar structure. The dash line marker represents a 24 hour day (data sourced from http://wdc.kugi.kyoto-u.ac.jp/index.html).

Figure 4.5 with panels a)-d) depicts four of the spatiotemporal maps for RTEC over South Africa's ionosphere for the 2012 Reference Day. The UT times in Figure 4.5 for the visualization is 04:15 UT (~ sunrise; panel a), 10:30 UT (~ solar noon; panel b), 16:45 UT (~ sunset; panel c) and 22:00 UT (~ solar midnight; panel d). The following description gives the spatiotemporal development of RTEC over South Africa during the 2012 Reference Day.

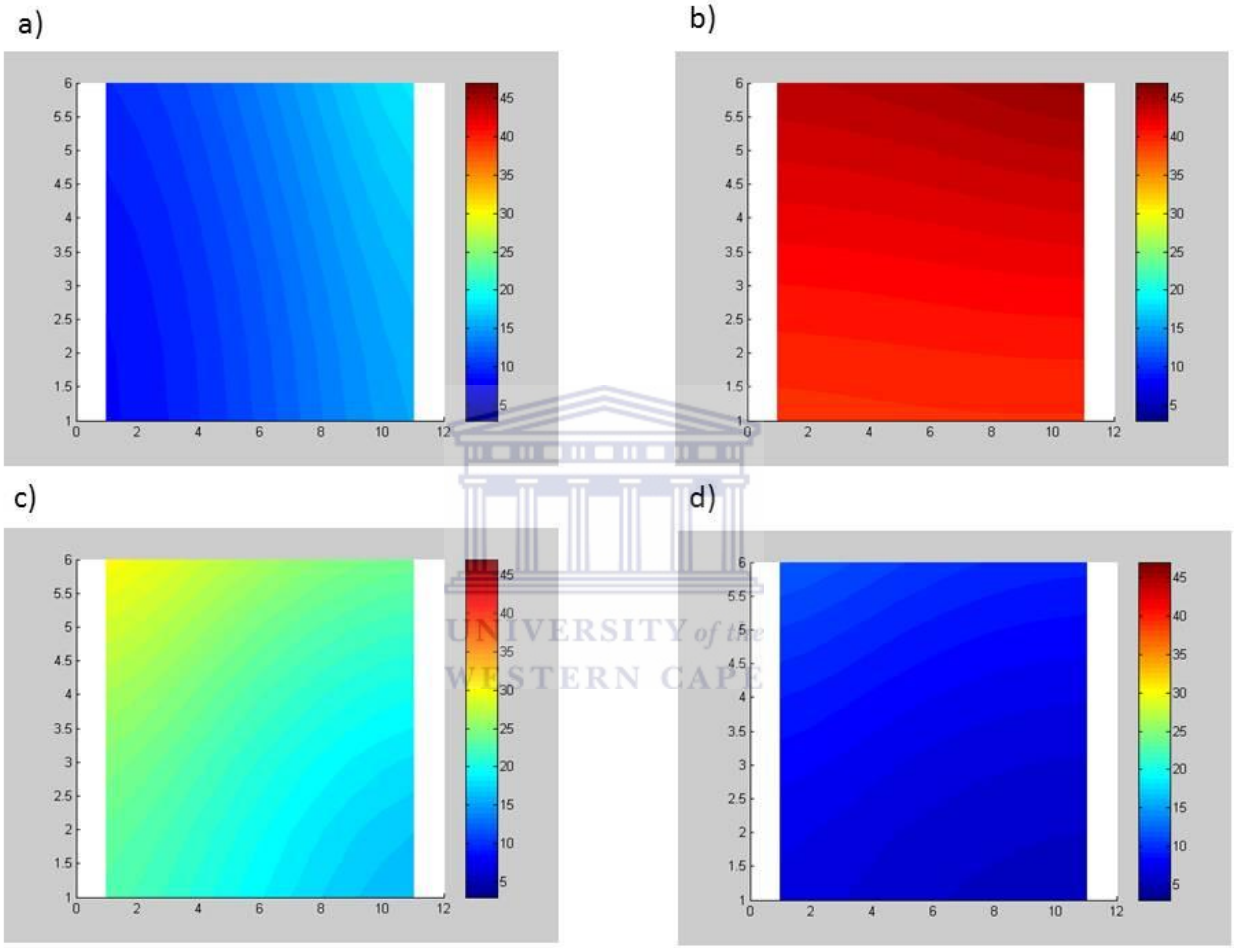


**Figure 4.5:** A graphical visualization that illustrates RTEC spatiotemporal maps over the ionosphere of South Africa for 2012 Reference Day. The UT times for panels a)-d) are 04:15 UT (~ sunrise), 10:30 UT (~ solar noon), 16:45 UT (~sunset) and 22:00 UT (~ solar midnight), respectively.

The 2012 Reference Day description starts at midnight, near the end of the night-time interval which is dominated by recombination. At this time the undisturbed level of RTEC for the Reference Day was relative low because of recombination still at a very high. RTEC over South Africa will be uniformly distributed, but with the onset of sunrise at 04:20 UT (06:20 SAST, during early morning) the solar driven photoionization process will overwhelm recombination, which will in turn causes an increase in RTEC, the same as was observed for

the 2003 Reference Day. As mentioned above, at sunrise RTEC begins to increase with greatest values in the northeast; the region of heightened RTEC values then moves across South Africa. At solar noon (about 10:30 UT, about 12:30 SAST), RTEC reaches its maximum since the solar zenith angle is smallest and thus there are the greatest rates of photoionization. After solar noon, the solar zenith angle begins to increase as the Sun begins its descent to sunset at a time of 16:45 UT (18:45 SAST) and with it we observe a decrease in RTEC over South Africa. After sunset, as solar midnight approaches, recombination causes decreases in the RTEC values, again as observed in the 2003 Reference Day. The minimum and maximum average RTEC values for the 2012 Reference was recorded to be 3 and 47 TECU respectively. The trend of average RTEC for the 2012 Reference Day can be viewed in Figure 4.6. This graph is constructed in the same way as was Figure 4.3.

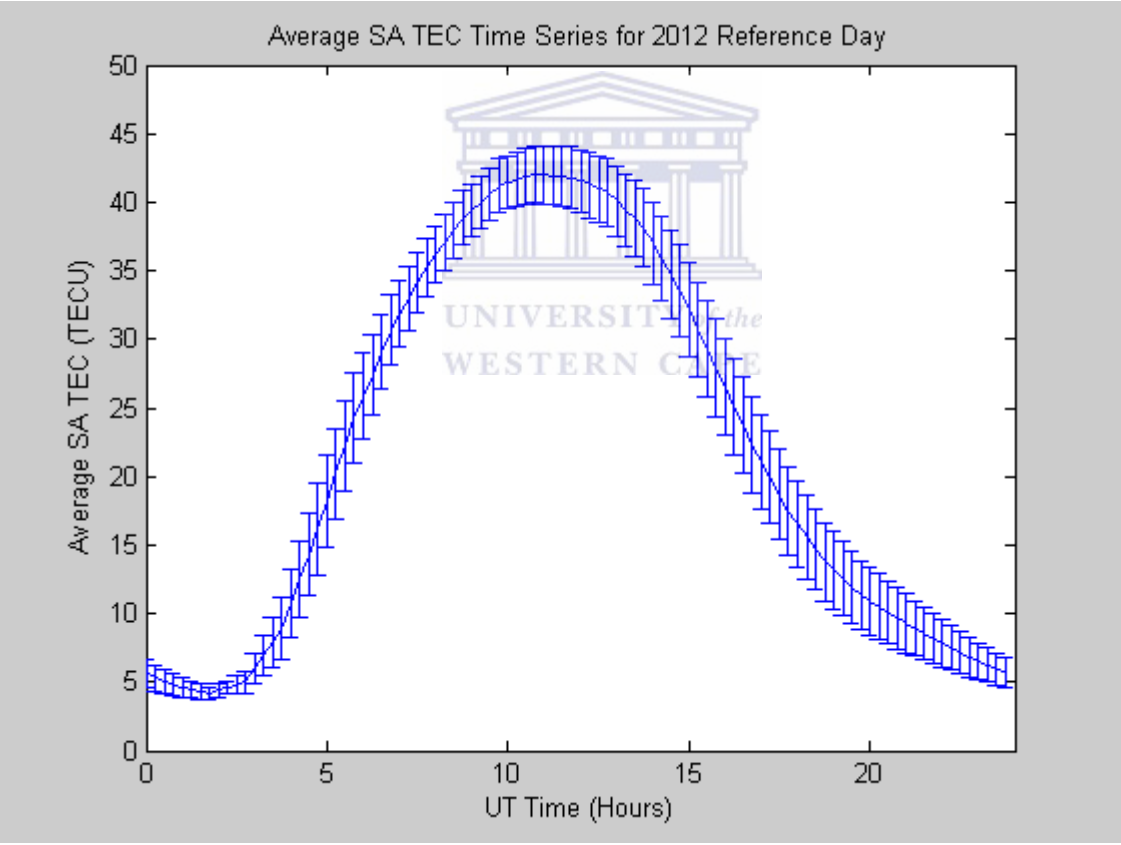


**Figure 4.6:** Depiction of the average South African RTEC time series for 2012 Reference Day, where the average value is of the 66 values of RTEC, and the error bars which give the RMS deviation of those 66 values about the mean.

We see that, as for the 2003 Reference Day average RTEC time series, the average RTEC time series for the 2012 Reference Day is characterized by four broad intervals: an interval when average RTEC has a roughly constant minimum value, an interval when average RTEC

has a high rate of increase, an interval when average RTEC has a roughly constant maximum value, and an interval when average RTEC is decreasing. The intervals of maximum and minimum RTEC for the 2012 Reference Day have durations of 4 hours for both. The rates of increase and decrease of average RTEC for the 2003 Reference Day are about 5.3 and about 4.0 TECU per hour, respectively.

The Reference Days for 2009, 2010 and 2011, which years also fall within the Post Solar Minimum solar cycle phase, all follow the same daytime and night-time cycle over South Africa's ionosphere as the 2012 Reference Day. The only difference is that average TEC amplitudes (e.g. maximum and minimum RTEC) that will vary between the Reference Days. We discuss the variation of the average TEC time series across the years of this study in the following subsection.

### 4.3.3 TEC over South Africa during Solar Minimum for 2008 Reference Day

As discussed above for the 2003 Reference Day and the 2012 Reference Day, in order to properly describe the effects of mid-latitude magnetic storms on RTEC over South Africa, it is necessary to provide the context for those effects by describing the pattern of RTEC in the absence of mid-latitude magnetic storms. The seven days 01-07 March 2008 were relatively calm; based on the Dst index for those days, no storms took place. Hence, those days were used to form the 2008 Reference Day by the process previously described. The graphical representation of the Dst index for the period 01-10 March 2008 can be seen in Figure 4.7. The 2008 Reference Day and 2008 Storm fall during Solar Minimum. The following description gives the spatiotemporal development of RTEC activity over South Africa during the 2008 Reference Day.

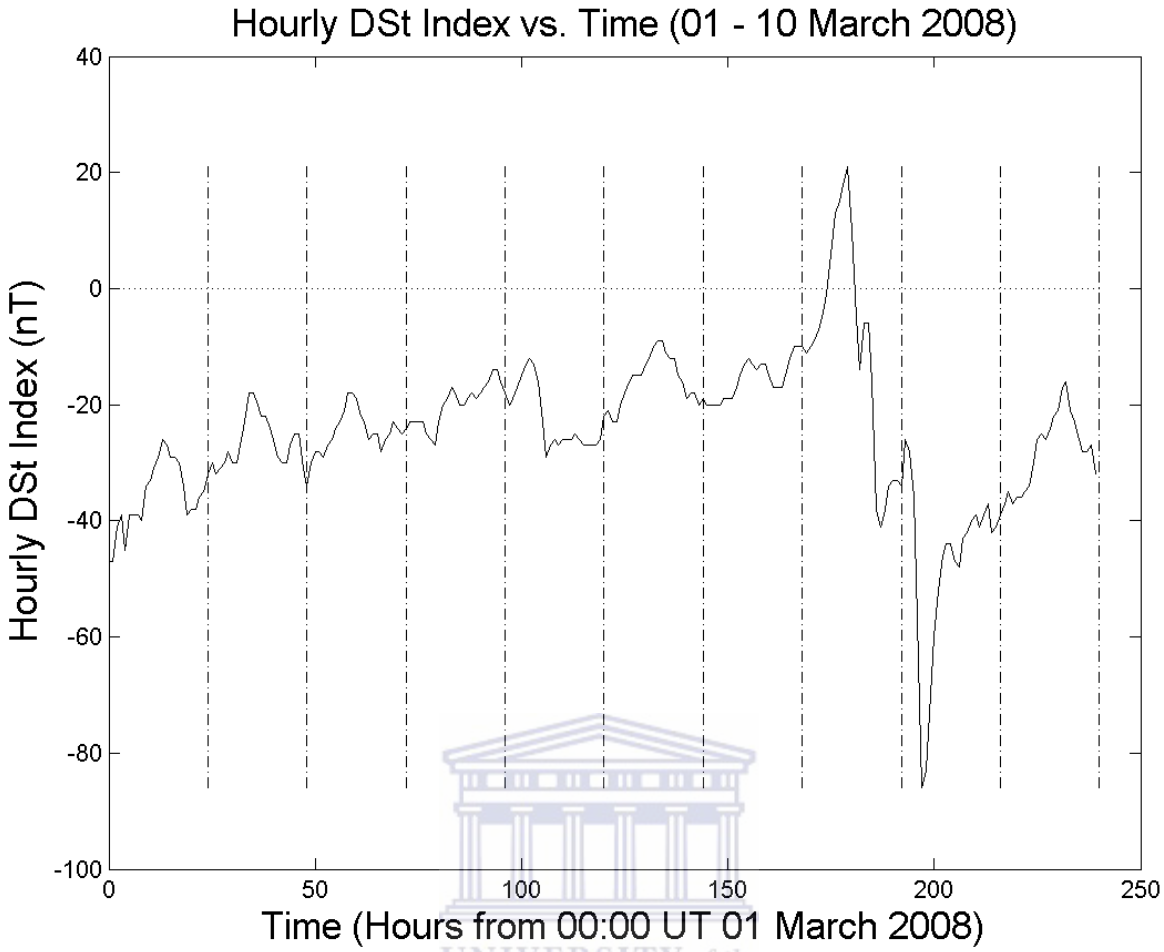




**Figure 4.7:** Graphical representation of the 2008 magnetic storm in terms of Dst geomagnetic index. The 2008 Storm has a dipolar structure. The dash line marker represents a 24 hour day (data sourced from http://wdc.kugi.kyoto-u.ac.jp/index.html).

Figure 4.8 with panels a)-d) depicts four of the spatiotemporal maps of TEC for South Africa's ionosphere for the 2008 Reference Day. The UT times in Figure 4.8 are 04:15 UT (~ sunrise; panel a), 10:30 UT (~ solar noon; panel b), 16:45 UT (~ sunset; panel c) and 22:00 UT (~ solar midnight; panel d). The following description gives the spatiotemporal development of TEC over South Africa during the 2008 Reference Day.

The 2008 Reference Day analysis starts at midnight, which is near the end of the night-time interval dominated by recombination. During this time the undisturbed level of TEC for the 2008 Reference Day was relatively low due to the fact that recombination is the dominant process, and because it has been many hours since there has been any photoionization. RTEC over South Africa is nearly uniform. With the onset of sunrise at 04:20 UT (06:20 SAST, during early morning), solar insolation driven photoionization overwhelms recombination,

which leads to an increase in RTEC, the same as was observed for the 2003 Reference Day (Figure 4.2) and the 2012 Reference Day (Figure 4.5). As mentioned above, with the onset of sunrise the RTEC begins to increase with maximum values in the northeast; as time proceeds the region of heightened RTEC values moves southwestward across South Africa. At solar noon (about10:30 UT, about 12:30 SAST), RTEC over South Africa will have reached a maximum since the solar zenith angle is at a minimum and as a result there are the greatest rates of photoionization for this period. After solar noon, the solar zenith angle begins to escalate as the Sun begins its descent to sunset at a time of 16:45 UT (18:45 SAST) and as it does so we observe decreased RTEC over South Africa. After sunset, as solar midnight approaches, recombination causes decreases in the RTEC values, again as observed in the 2003 Reference Day and 2012 Reference Day.

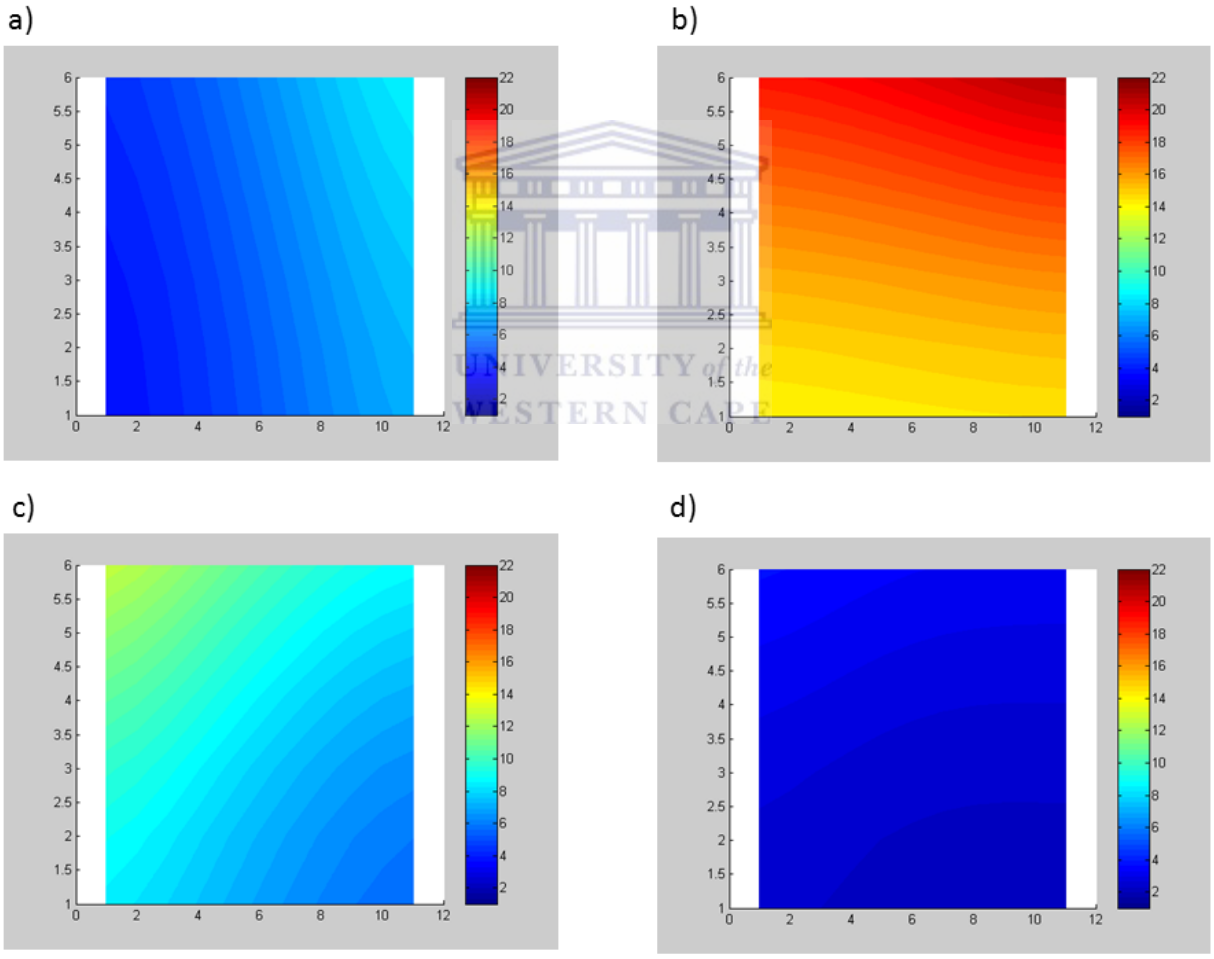


**Figure 4.8:** A graphical visualization that illustrates TEC spatiotemporal maps over the ionosphere of South Africa for 2008 Reference Day. The UT times for panels a)-d) are 04:15 UT (~ sunrise), 10:30 UT (~ solar noon), 16:45 UT (~sunset) and 22:00 UT (~ solar midnight), respectively.

The minimum and maximum average RTEC values for the 2008 Reference Day were recorded to be 1 and 22 TECU respectively. The trend of average RTEC for the 2008 Reference Day can be viewed in Figure 4.9, which is constructed in the same way as was Figure 4.3 and 4.6.

We see that, as for the 2003 Reference Day and the 2012 Reference Day average RTEC time series, the average RTEC time series for the 2008 Reference Day is characterized by four broad intervals: an interval when average RTEC has a roughly constant minimum value, an interval when average RTEC has a high rate of increase, an interval when average RTEC has a roughly constant maximum value, and an interval when average RTEC is decreasing. The intervals of maximum and minimum RTEC for the 2008 Reference Day have durations of about 3 hours and about 5 hours respectively. The rates of increase and decrease of average RTEC for the 2008 Reference Day are about 2.3 and about 3.0 TECU per hour, respectively.

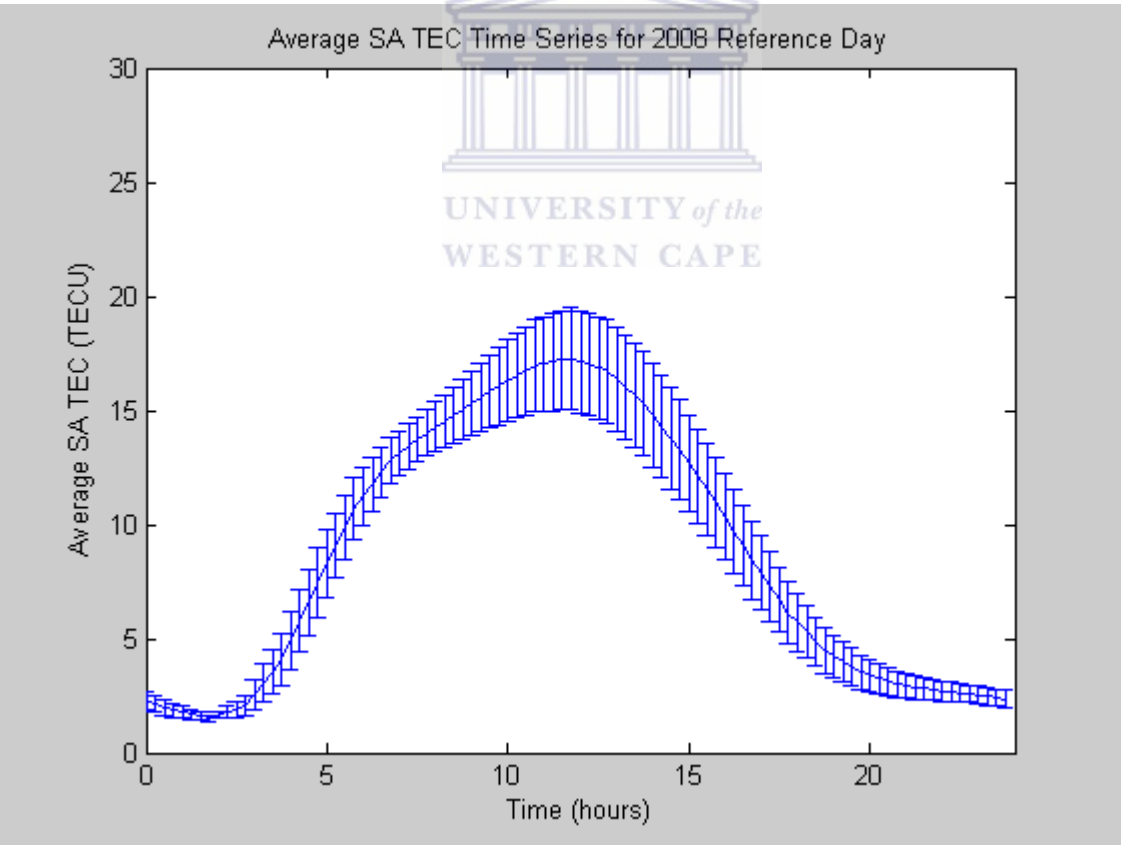


**Figure 4.9:** Depiction of the average South African RTEC time series for 2008 Reference Day, where the average value is of the 66 values of RTEC, and the error bars which give the RMS deviation of those 66 values about the mean.

### 4.3.4 Average Reference Day TEC over South Africa across the years of this study

Figure 4.10, displays a stacked plot of the average South African Reference Day RTEC Time Series for all eight Reference Days. As seen from the Figure, all of the eight Reference Days have roughly the same general diurnal pattern for average RTEC, but have different amplitudes (maximum and minimum RTEC). As explained previously, the reason for this is that the dominant process is the diurnal cycle of illumination and darkness of the ionosphere.

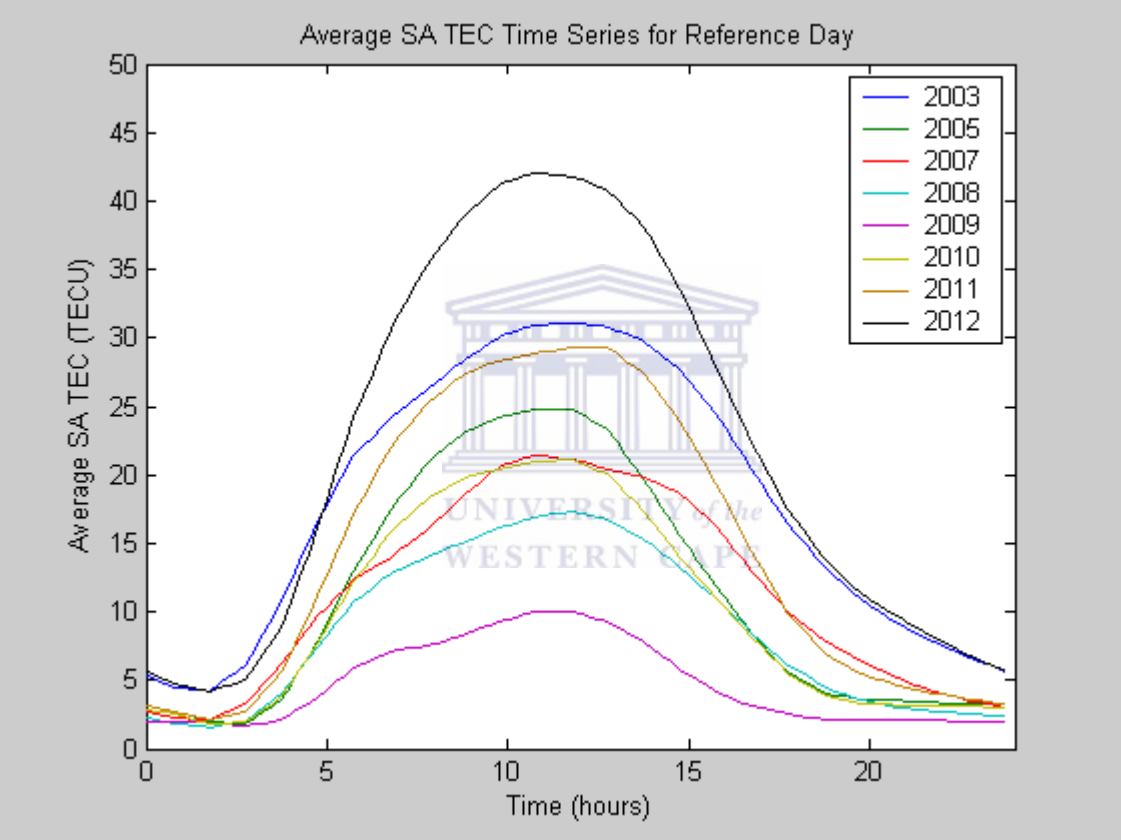


**Figure 4.10:** Illustration of the average SA Reference Day TEC Time Series for all eight Reference Days.

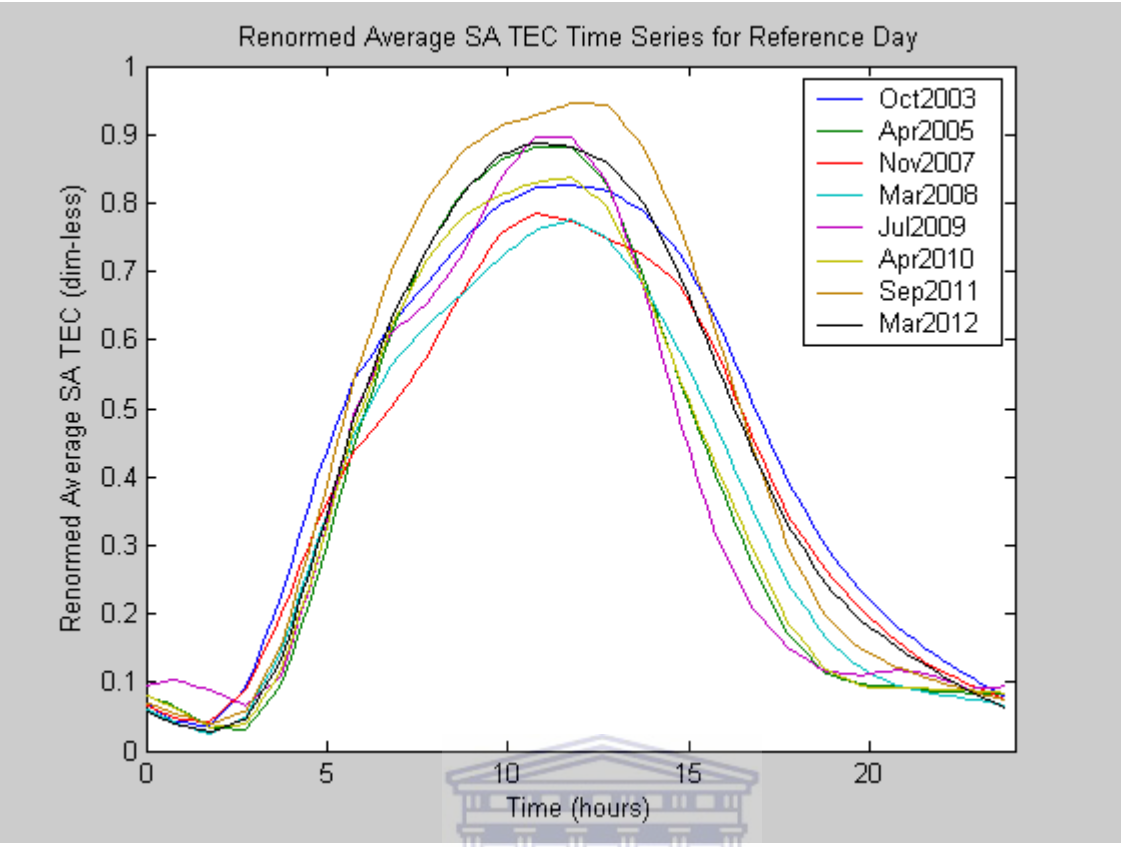


**Figure 4.11:** Illustration of the renormed average SA Reference Day TEC Time Series for all eight Reference Days.



Figure 4.11 depict the average TEC time series after renormalization, which was done by dividing each Reference Day average TEC time series by the maximum value at any location within the SA map during the Reference Day. Figure 4.11 depicts the seasonal dependence of the average TEC during Reference Days. This seasonal effect follows since daytime periods, when RTEC is greater, last longer during the summer season than for winter, since the tilt of the Earth's rotational axis in relation to the orbital plane is tied to the Earth's revolution round the Sun and in turn gives rise to the seasons. Therefore in summer, a hemisphere is tilted to the Sun and thus will experience superior solar radiation than in winter when the same hemisphere will be tilted away from the Sun's solar radiation. Since South Africa is in the southern hemisphere, days in November, December and January will be longer, leading to longer daily intervals of photoionization, and days in May, June and July will be shorter, leading to shorter daily intervals of photoionization.

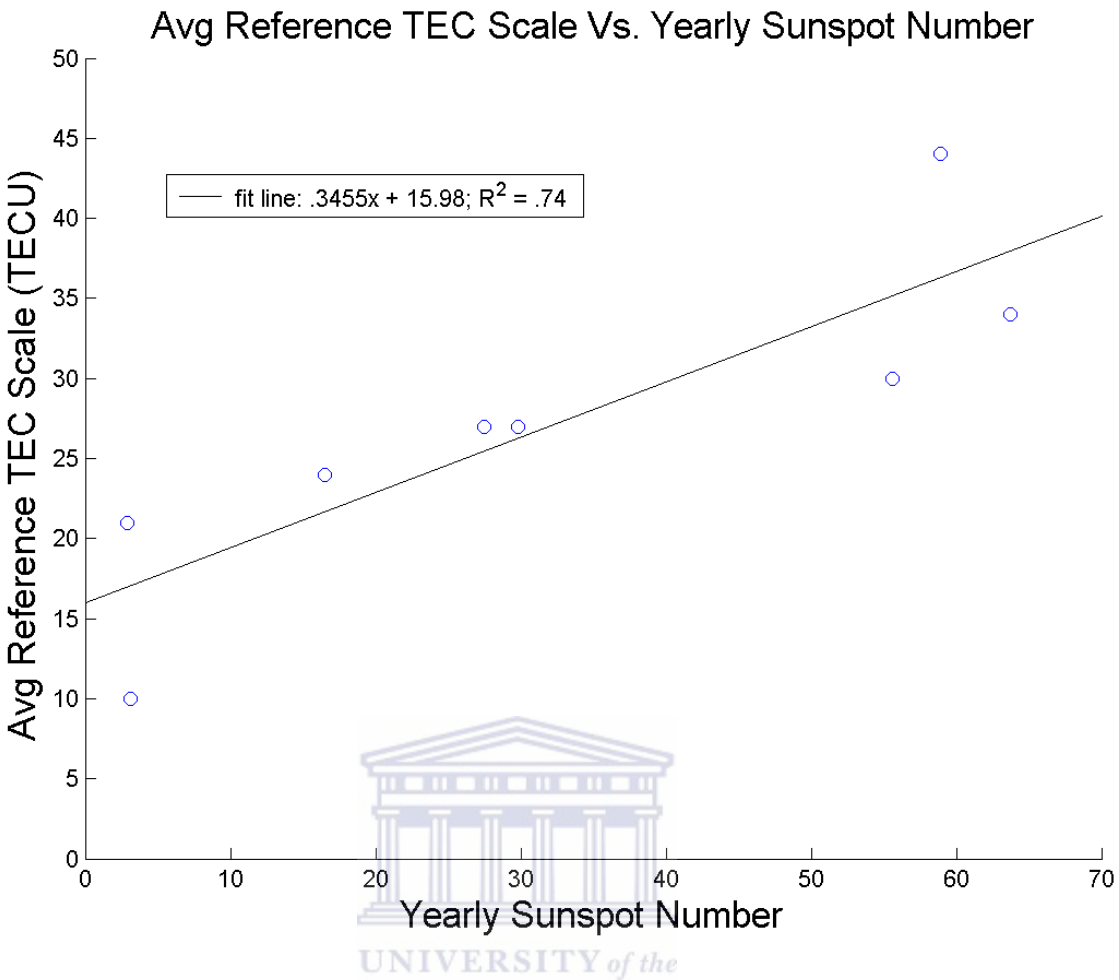


**Figure 4.12:** Illustration of the renormed average SA Reference Day TEC Time Series for all eight Reference Days.

Figure 4.12 depict the scale of variation of average Reference Day TEC versus the annual sunspot number (Wolf number). The sunspot number, as previously discussed in Chapter 2, is a measure of the solar activity. The scale of variation for a given Reference Day is simply the maximum value of average Reference Day TEC minus the minimum value of average Reference Day TEC. As can clearly be seen from the plot, there is significant dependence of the average Reference Day TEC scale of variation on the annual sunspot number, and hence on the phase within a solar cycle. If solar activity is high, as when the sunspot number is high, e.g. near to solar maximum, more radiation is emitted by the Sun. In turn, this leads to greater rates of photoionization in the ionosphere and consequently an increase in TEC. When the Sun is less active, e.g. near to solar minimum, less radiation will be emitted from the Sun, consequently this will lead to less ionization in the ionosphere and lower values of TEC. The same variation can be observed in Figure 4.10 for both the maximum values of average Reference Day TEC and for the minimum values of average Reference Day TEC,

although the trend is slightly less obvious for the minimum values of average Reference Day TEC.

Dissimilarity of the ionosphere is affected by the amount of radiation coming from the Sun and during high solar activity more radiation is produced from the Sun and vice versa for low solar activity (McNamara, 1991). Accordingly, the layers of the ionosphere become more ionized due to the greater intensity of the solar emitted particles reaching the layer, during high solar activity. Thus TEC density in the layer during high solar activity will be greater as the TEC density during low solar activity.

## 4.4 Variations of Storm TEC patterns over South Africa

### 4.4.1 TEC over South Africa during Post Solar Maximum for 2003 Storm

With a thorough understanding of the spatiotemporal pattern of RTEC over South Africa during the Reference Days selected for this study, we are now in a position to discuss the effect of magnetic storms on TEC over South Africa. We begin with a discussion of the well-studied 'Halloween Storm' of 2003 (Basu, et al., 2005; Mannucci, et al., 2005; Tsurutani, et al., 2005; Yizengaw, et al., 2006; Becker-Guedes, et al., 2007; Manju, et al., 2009). This storm occurs during the Post Solar Maximum phase of the solar cycle. During the storm period of 29-31 October 2003, Earth experienced moderate to intense Dst storms (classification as seen in Table 4.1 above), which are taken as a signal of major geomagnetic storm activity during those dates. In the following, we describe the spatiotemporal development of storm TEC activity over South Africa during the multi-day duration of the October 2003 geomagnetic storm, with the objective of trying to determine the extent to which the geomagnetic storm is a driver of variations in TEC during that storm. As presented earlier (in Section 4.2.2), the storm TEC activity is quantified by the ΔTEC time series. Since the figures presented (Figure 4.13) show just ΔTEC values, it is worth noting that ΔTEC is typically a small fraction of the total TEC value. It is also noteworthy that ΔTEC can take on negative values because of the differencing method used in its generation. The following will discuss day one-three (29-31 October 2003) of the 2003 Storm (Figure 4.1).

#### 4.4.1.1 29 October 2003

At 0000UT (UT midnight) on the first day of the 2003 Storm, when South Africa is near the end of the recombination dominated night-time interval, ΔTEC is positive across the entire map, with a Southeasterly gradient. As time advances, the gradient gets shallower and rotates to a Southwesterly direction, and then becomes steeper. That gradient continues to steepen as ΔTEC decreases in the Northeast corner of the map. As that minimum value continues to decrease, the centre of the minimum shifts to the centre of the Northern edge of the map and the gradient is Southward; there is a slight positive ΔTEC in the Southwest corner but otherwise ΔTEC is negative across the entire map. By 07:00 UT, which is after sunrise, ΔTEC is negative across the entire map and the minimum ΔTEC location has moved Southward to the middle of the map. Subsequently, that minimum in ΔTEC drifts to the Southwest, becomes even more negative, and broadens longitudinally to cover nearly the full width of the map. By 09:00 UT, ΔTEC has begun to increase in the Northeast corner, giving a Northeasterly gradient. That trend continues until 10:30 UT, when the location of the maximum of ΔTEC spreads across the entire Eastern edge of the map and the gradient is now Easterly. By 11:30 UT, the location of the maximum ΔTEC has shifted to the Southeast. During the last 3 hours, ΔTEC is negative over more than half of the map. During the next hour, another trough in ΔTEC appears in the middle of the Western edge of the map, and ΔTEC becomes negative across nearly the entire map. By 14:00 UT, the location of the minimum has shifted to the Southwest corner of the map and simultaneously ΔTEC becomes slightly positive in the Northeast corner of the map, leading to a very steep Northeasterly gradient. Over the next hour, ΔTEC increases to positive values throughout the map, lowering the gradient almost completely.

At 16:00 UT, the map shows a band of slightly positive ΔTEC running from the Southeast corner to the Northwest corner, and dropping to nearly zero away from that band. For the next two-and-a-half hours, ΔTEC continues to increase significantly on the Western edge of the map, leading to positive values of ΔTEC throughout the map. The zone of increases shifts Southward; by 19:30 UT, ΔTEC is strongly positive across the entire map, with a band of elevated ΔTEC running from the Northeast corner to the Southwest corner. During the next hour, the maximum ΔTEC increases slightly and moves Eastward across the Southern edge of the map. During the remainder of the 24 hour day, the maximum location of ΔTEC is both fairly constant and sits in the Southeastern corner of the map, and the Southeasterly gradient gradually steepens as ΔTEC decreases close to zero in the Northwest corner of the map. We

note that during the second half of this data, the Dst index has steadily declined by about 25 nT/hr, to a value of about -375 nT at the end of the day.

#### 4.4.1.2 30 October 2003

Comparing the ΔTEC of the first day of the 2003 Storm at UT midnight to the 2nd day (30 October 2003) of the 2003 Storm at the same time, the ΔTEC for the 2nd day was higher than the ΔTEC than the first day. The high ΔTEC situated at the South East is unusual due to the fact that the Sun has already set, but still ΔTEC is at a high compared to a normal undisturbed Reference Day. Although the Dst index increased from about -353nT (00:00 UT) to about -156nT (10:30 UT) and during this time (roughly solar midnight to solar noon), the ionosphere of South Africa still experiences immense geomagnetic activity over the Southern part of the country with the pattern of the gradient between UT midnight and solar noon the same as the first day of 2003 Storm, with exception of the locations of statistically negligible storm effect, which increased to about 20% in area of the map compared to about 10% on the first day. Another difference between the first two days of the 2003 Storm is that the intensity of the ΔTEC is not the same, with the second day of the 2003 Storm containing higher ΔTEC across the map compared with the first day of the 2003 Storm.



A few hours after sunrise the gradient takes on an Easterly longitudinal direction, moving across the map with appearances of locations of statistically negligible storm effect about 15% in total area of map. This gradient also brings along a shortage of electrons as it moves across the map, with the shortage situated in the West and greatest ΔTEC located at East, but with the conclusion of the gradient, locations of statistically negligible storm effects of size about 15% moves out as well. Approaching sunset, a North East gradient comes in over the map, with greatest ΔTEC in the North East and shortage of electrons in South West, but also containing statistically negligible storm effect locations of about 35% in total area of map. In addition to this gradient, the level of ΔTEC rises over the entire map, leading a surplus of electrons everywhere on the map. After sunset an Easterly gradient takes effect, with greatest ΔTEC situated at East location on map, and with least located ΔTEC at the West, with no shortage of electrons across the whole map. The gradient continues to move outward (South East) with North West mostly differential electron concentrated than the South East. The latter gradient movement is unusual in the sense that the Sun has already set over South Africa; hence ΔTEC should be less than it was in the afternoon, but as this gradient is moving across the country the North West increases with differential electron concentration.

Eventually the gradient moves outward (South East), with a blob of ΔTEC of magnitude of 0.40 TECU moving from the West, to South West, to South and eventually outwards in South East direction on the map, as the gradient moved across South Africa. Ultimately this gradient will move outward with the onset of solar midnight and will have the greatest ΔTEC situated in the South East, with the least located in the North West at the end of the second day of the 2003 Storm. With the aid of the Dst plot (See Figure 4.1), it can be seen that at about solar midnight there is a strong outward bay, with a Dst index of about -371nT, where this index value indicates super storm status, hence the unusual ΔTEC across the map.

#### 4.4.1.3 31 October 2003

The 3rd and final day of the 2003 Storm (31st October 2003) experienced a similar pattern of gradient and ΔTEC over South Africa for the same times. The differences between the final day and the first two days of the storm is that the Dst index is in recovery phase, whereas the Dst index for the other two days experienced mild to superstorms geomagnetic activity and the intensity of the ΔTEC is greater than the first two days of the 2003 Storm. With regard to the statistically negligible storm effect locations for the last day of 2003 Storm, the area for the total map is about 20% for the same times as the first two days. As seen from the description of the 2003 Storm, ΔTEC has a latitudinal and longitudinal variation over the ionosphere of South Africa. For some locations the Sun is regularly directly overhead at locations on or very near to the equator, consequently the Sun's release of its solar radiation is more overhead over locations such as these. Subsequently the net effect is that more ionospheric photoionization will take place and therefore greater ΔTEC for these locations over South Africa. In Figure 4.13 is a visualization of how ΔTEC varies over South Africa with the gradients over a 24 hour day for the 2003 Storm.

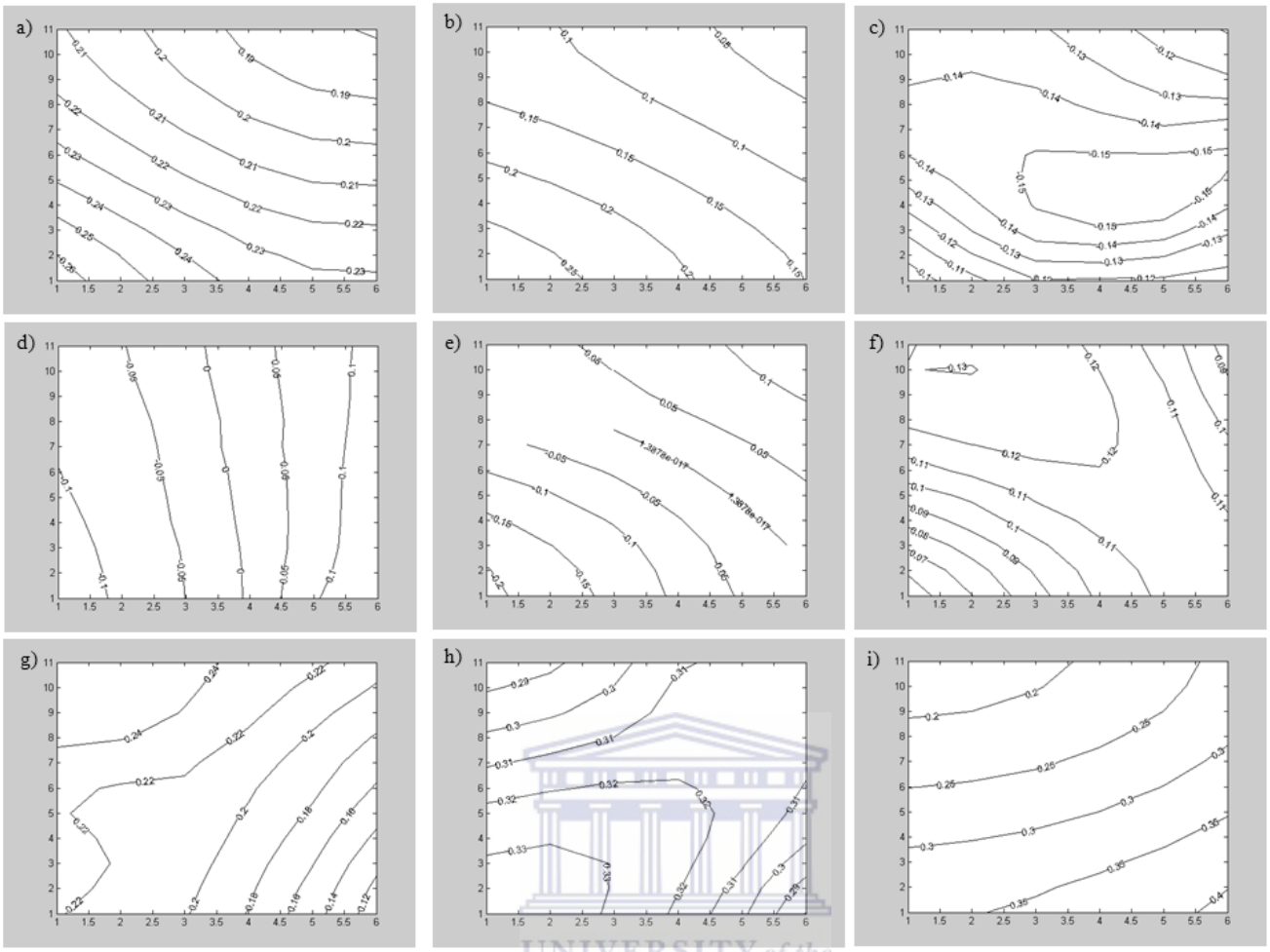


**Figure 4.13**: Contour plots of ΔTEC illustrating the variation of ΔTEC over South Africa during the 2003 Storm. All panels are for 29 October 2003. The times shown are in UT and are a) 02:00, b) 04:15, c) 07:00, d) 10:30, e) 13:45, f) 16:00, g) 18:00, h) 19:30, and i) 22:00.

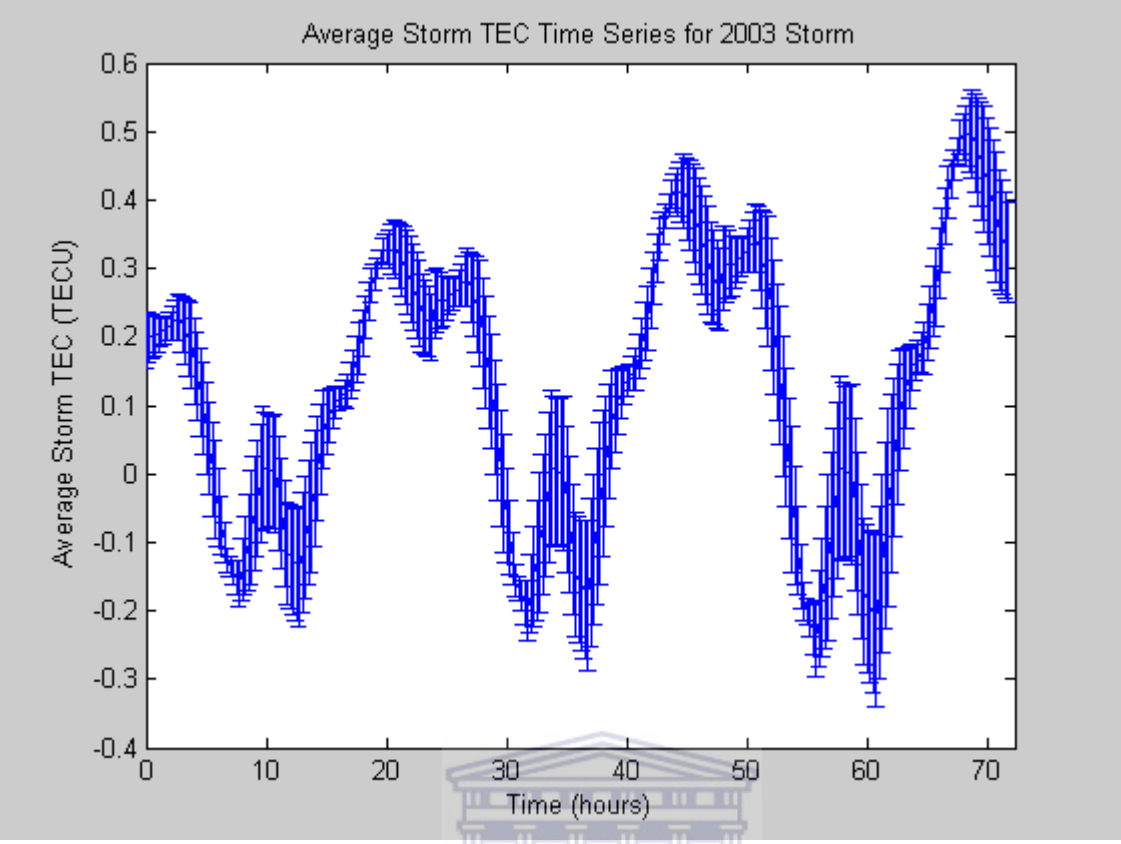


**Figure 4.14:** Graphical display showcasing the average Storm TEC Time Series for the 2003 Storm (29-31 October 2003), where the x label represents the time in hours from 00:00 UT 29 October 2003. The average Storm TEC Time Series follows a modulated linear period. The average value is of the 66 values of TEC, where the error bars is just the RMS deviation of the 66 values about the mean.



Above in Figure 4.14 is a graphical display illustrating the presence of a diurnal pattern for the average ΔTEC for the 2003 Storm. The diurnal pattern of the average ΔTEC follows the same trends at the typical Reference Day diurnal pattern, indicating that there is a strong modulation of the storm driven ΔTEC by the diurnal photoionization cycle, regardless of the level of storm activity.

### 4.4.2 TEC over South Africa during Post Solar Maximum for 2012 Storm

With a thorough understanding of the spatiotemporal pattern of TEC over South Africa during the 2012 Reference Day, we are now able to discuss the effects on TEC over South Africa during a Post Solar Minimum period in the presence of mid-latitude magnetic storms. The storm as mentioned above occurs during the period of 09-12 March 2012 (see Figure 4.4) and throughout this time Earth experienced moderate to super Dst storms (classification as seen in Table 4.1), thus this serves as a signal that the 2012 Storm was a major geomagnetic

storm. As stated earlier for the 2003 Storm analysis, the storm TEC activity is quantified by the ΔTEC time series, and thus for the subsequent sub section, we will describe the ΔTEC spatiotemporal maps over South Africa for day one-three (09-11 March 2012) of the 2012 Storm. We are looking at the history (see Section 4.2) of ΔTEC to determine the type and extent to which the geomagnetic storm is a driver of variations in ΔTEC for the March 2012 Storm. Since the figures presented (Figure 4.15) show only ΔTEC values, it is worth noting that ΔTEC is typically a small fraction of the total TEC value. It is also of note that ΔTEC can take on negative values for the reason that the differencing method used in its generation. The following will discuss day one-three (09-11 March 2012) of the 2012 Storm.

#### 4.4.2.1 09 March 2012

We begin at midnight UT on the first day (09 March) of the 2012 Storm, when the night-time interval, which is mostly dominated by recombination, is nearing an end. An hour after solar midnight, there is a location situated over the central right half of map, with an area size of about 10% of the total map size that contains ΔTEC that is statistically negligible to a storm effect. During the hours before sunrise, the size of these locations increases by a factor of 1-2 and they wander over the map at speeds on the order of 1000 km/hr. It is also noted that ΔTEC is small and positive throughout the map, with values on the order of low negative TECU values during the period before sunrise. We note that coincidentally, this is before the onset of the magnetic storm. The values are certainly comparable to the variations observed in creating the 2012 Reference Day.

Just before sunrise at 03:45 UT, a gradient with a Northeasterly direction gets shallower and rotates to a Northwesterly direction. As time advances after sunrise, the gradient gets steeper and rotates to the North, as ΔTEC increases in the top half of the map. After sunrise at 07:00 UT, this latitudinal gradient remains steady and ΔTEC remains positive across the map, with the Southwest containing the minimum ΔTEC. As time passes by, the gradient now rotates to a Northwesterly direction with a shallow pattern across the map. The gradient continues in the same direction and gets shallower, as ΔTEC increases across the entire map but more rapidly in the East than in the West. Gradually, a localized region of maximum ΔTEC is found on the Western edge of the map. Suddenly, over 30 minutes or less, the localized maximum moves Southward with a velocity of about 1000 km/hr. Approximately two hours before sunset (at about 14:45 UT), the gradient now shifts to a Southerly direction and becomes more shallow. The pattern as mentioned above continues for the two hours before

sunset, but as the gradient moves to the Southeast, ΔTEC is tending to values near zero over the majority of the map.

Just after sunset, at 17:45 UT, locations of statistically negligible storm effect of area about 25% of the total map are located over the top half of the map. The locations of these statistically negligible storm effect increases by a factor of 1-2 for the next hour. After an hour these locations shrink in area size by a factor of 1, while the maximum ΔTEC over the map shifts to a Northeasterly direction, with the majority of the map with low negative values to near zero ΔTEC values. For the remainder of the 24 hour day the minimum ΔTEC values are located in the Southwest and maximum ΔTEC (which is still near zero) at the Northeast; the shallow Northeasterly gradient slowly rotates to the North. With the use of Figure 4.4 above, it can be seen that during the 24 hour day of the first day of the 2012 Storm, the Dst index first decreased by about 15 nT/hr until about 0800 UT, then the southward bay persisted for about ten hours, and then the index began to recover at about about 5 nT/hr, to an index value of -66 nT at the end of the first day.

#### 4.4.2.2 10 March 2012

There are differences and similarities between the second day of the 2012 Storm (10 March 2012) and the first day of the storm (09 March 2012) with regard to the spatiotemporal variation of ΔTEC across the map. It was noted that during the second day of the storm the gradients are steeper compared to the first day of the storm. Also noted was that ΔTEC increased across the map by a factor of about 1.0 TECU between 06:00 UT (few hours after sunrise) and 14:45 UT (few hours before sunset). After sunset the ΔTEC has generally the same pattern as the first day of the 2012 Storm just after sunset, with slightly negative ΔTEC located over the majority of the map, but later the location of the minimum shifts to the Southwest and the maximum (still low) ΔTEC is located at the Northeast, with a Northeasterly gradient across the map. Also, there are locations of statistically negligible storm effect of about 20% of the area of the total map scattered over the top half of the map as solar midnight approaches. It is noted from Figure 4.4 above that on the second day of the 2012 Storm, that the Dst index makes a steady recovery to undisturbed conditions, to end the day with a value of -46 nT. The latter serves as an indication that the storm went from moderate to weak during the second day of the storm.

#### 4.4.2.3 11 March 2012

The third day of the 2012 Storm (11 March 2012) has similar features and differences compared to day one and two of the 2012 Storm. For day three of the storm, a few hours after solar midnight the statistically negligible storm effect locations compared to the day one -and two are small by a factor of about 1.0. Another difference is that for day three, a few hours before sunrise, at about 03:30 UT the map contains more minimum ΔTEC spread over the majority of the map, as compared to day one -and two, which had less low ΔTEC. With regard to the concentration of ΔTEC across the map, ΔTEC is more concentrated by a factor of about 1.0-1.5 TECU for day one -and two, respectively. The gradient direction follows the same directional rotation but magnitude of the gradient varies, being either steeper or more shallow; in general the gradient is steeper compared to the first two days of the 2012 Storm. Just after sunset, the sector areas of excess electrons for day three are about the same as for day one and day two of storm, with the statistically negligible storm effect locations spread all over the map. Also during the same time and in comparison, the maximum ΔTEC is situated at Northeast and minimum ΔTEC situated at Southwest as the Northeast gradient moves across the map for the rest of the 24 hour day, as solar midnight is looming. With aid from Figure 4.4 above, it can be seen that on the third day of the 2012 Storm the Dst index continues to recover to undisturbed conditions, and ends the day with an index value of -25 nT. The latter serves as an indication that the third day of the 2012 Storm experienced a weak storm type. Figure 4.15 is a visualization of how ΔTEC varies over South Africa with the gradients over a 24 hour day for 2012 Storm.

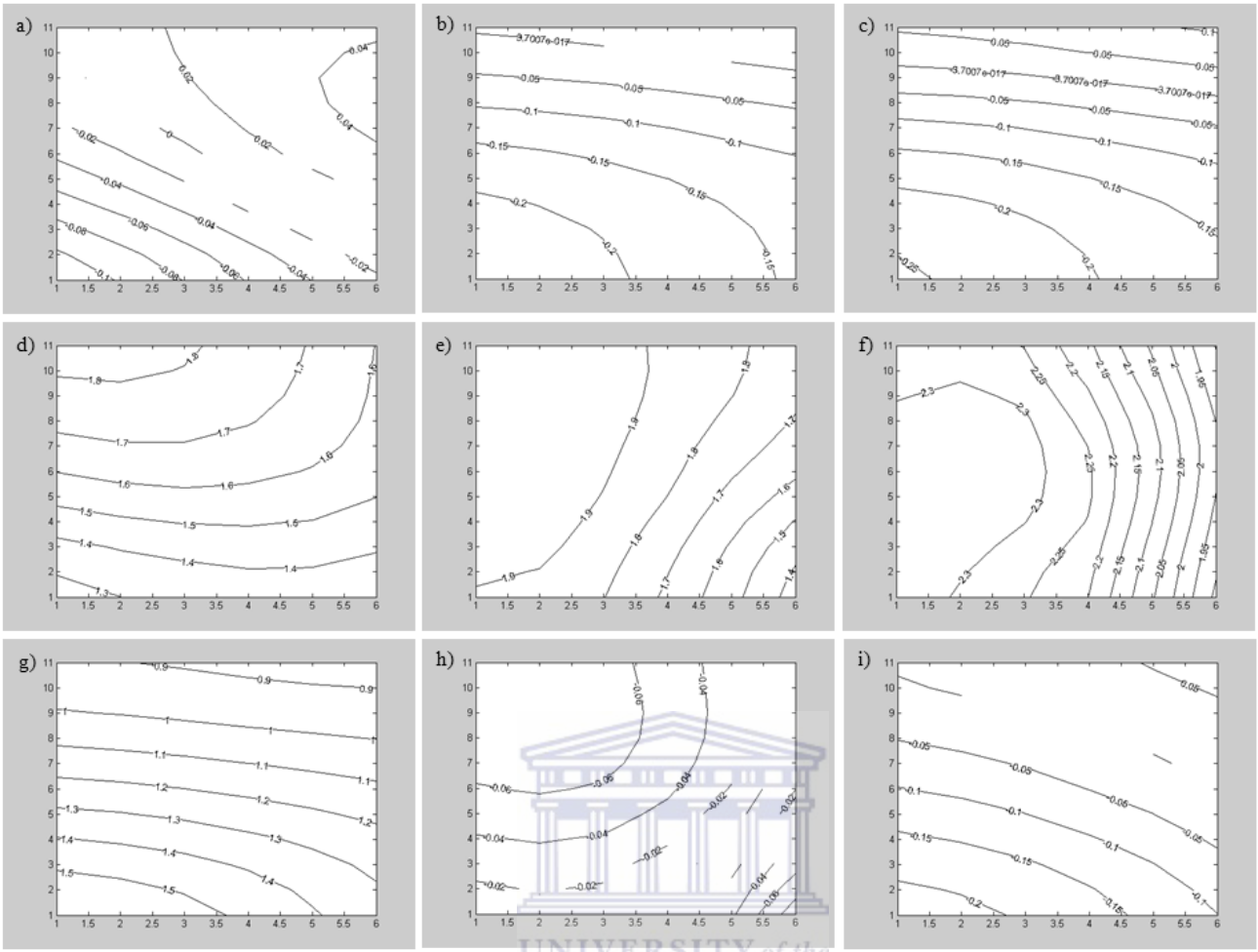


**Figure 4.15**: Contour plots of ΔTEC illustrating the variation of ΔTEC over South Africa during the 2012 Storm. All panels are for 09 March 2012. The times shown are in UT and are a) 00:45, b) 03:30, c) 03:45, d) 07:15, e) 09:30, f) 11:30, g) 14:45, h) 18:15, and i) 22:00.

Figure 4.16 is a graphical display illustrating the presence of a diurnal pattern for the average ΔTEC for the 2012 Storm. The diurnal pattern of the average ΔTEC follows the same trends at the typical Reference Day diurnal pattern, indicating that there is a strong modulation of the storm driven ΔTEC by the diurnal photoionization cycle, regardless of the level of storm activity.

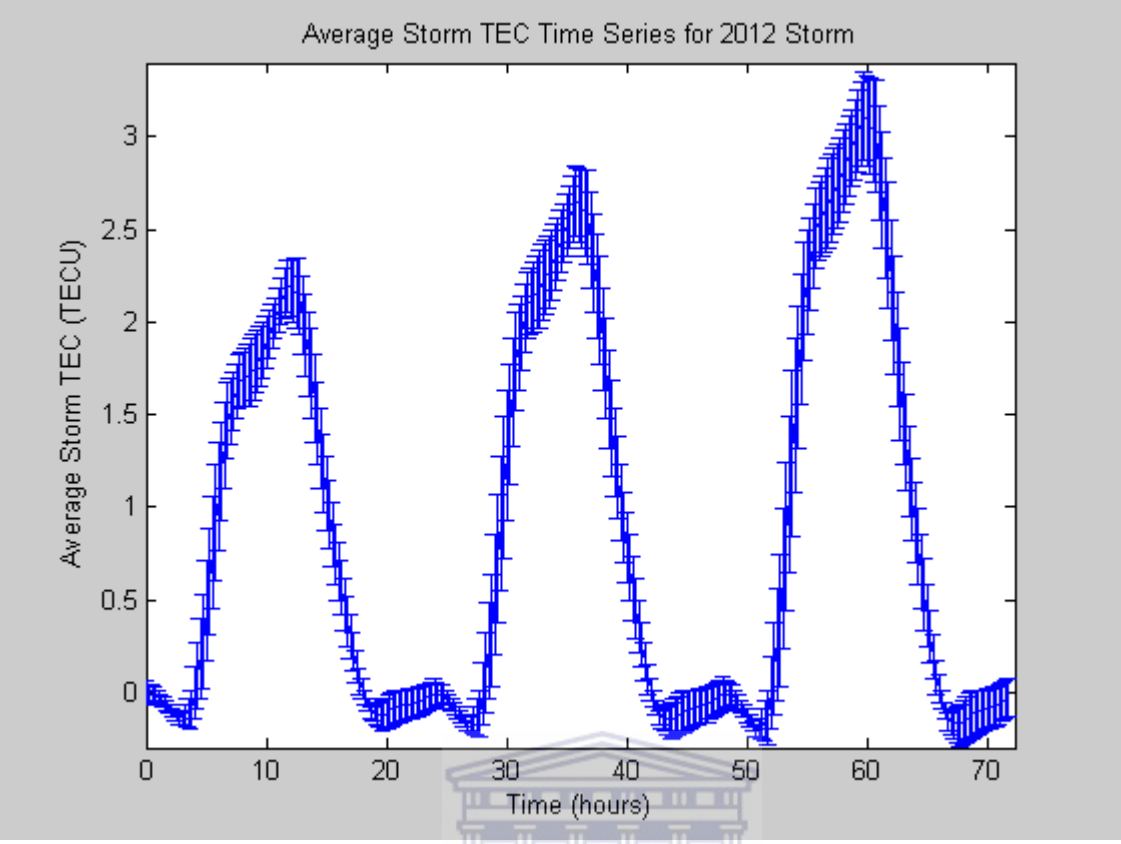


**Figure 4.16:** Graphical display showcasing the average Storm TEC Time Series for the 2012 Storm (09-11 March 2012), where the x label represents the time in hours from 00:00 UT 09 March 2012. The average Storm TEC Time Series follows a modulated linear period. The average value is of the 66 values of TEC, where the error bars is just the RMS deviation of the 66 values about the mean.



### 4.4.3 TEC over South Africa during Solar Minimum for 2008 Storm

As discussed for the 2003 Storm and the 2012 Storm, we established a very good understanding of the spatiotemporal pattern of TEC over South Africa during the Reference Days chosen for this study. Consequently we are now in a suitable position to discuss the effect of mid-latitude magnetic storms on TEC during a Solar Minimum period over South Africa for the 2008 Storm as well. The 2008 Storm occurs during a period of low sunspot number (March monthly average sunspot number = 9.3) compared to the 2003 Storm (October monthly average sunspot number = 65.5) and 2012 Storm (March monthly average sunspot number = 64.3), and thus a discussion for the 2008 Storm is essential for this thesis study. The storm as mentioned above happens during the Solar Minimum period, 08-10 March 2008. During this storm period, Earth experienced weak to moderate Dst storms (classification as seen in Table 4.1 above), where this serves as an indication that the 2008 Storm experienced geomagnetic activity during the storm period. As stated previously for

both the 2003 Storm and the 2012 Storm, the storm TEC activity is quantified by the ΔTEC time series, and thus for the following sub section, a description of the 2008 Storm ΔTEC spatiotemporal maps over South Africa for day one-three (08-10 March 2008) will be done. The history of ΔTEC will be looked at as well, to determine the type and extent to which the geomagnetic storm is a driver of variations in ΔTEC for the March 2008 Storm. Since the figures presented (Figure 4.17) show only ΔTEC values, it is worth noting that ΔTEC is typically a small fraction of the total TEC value. It is also of note that ΔTEC can take on negative values for the reason that of the differencing method used in its generation. The following will discuss days one through three (08-10 March 2008) of the 2008 Storm.

#### 4.4.3.1 08 March 2008

At 0000UT (UT midnight) on the first day of the 2008 Storm, South Africa is nearing the end of the recombination process that dominates night-time interval, it is observed that ΔTEC is positive across the entire map, with a Northeasterly gradient. As time advances, the gradient gets shallower and rotates to a Southeasterly direction, and this trend continues for another hour, with ΔTEC still positive across the entire map. For the next two hours ΔTEC is negative (small values) across the majority of the map. At about sunrise, the gradient steepens and rotates to a Northerly direction and the minimum ΔTEC shifts to the East of map. The trend mentioned above continues for another hour. Just after the hour, the gradient steepens a bit and rotates to a Northwesterly direction, with minimum ΔTEC shifting to the Southeast of map. By 07:45 UT, the gradient becomes shallower and now rotates to a Southwesterly direction, but as this trend continues for another hour or so, ΔTEC is negative (small values) in the Northeast of the map. The Southwesterly gradient continues across the map, with negative ΔTEC moving towards Southwest of map; as time elapsed for another two hours, ΔTEC is negative (small values) across the whole map. At about solar noon the gradient mentioned above continues with the Southwesterly trend for another three hours, with small negative ΔTEC values, spread over the whole map. At 13:15 UT, the gradient becomes very shallow, but still has a Southeasterly direction and negatively ΔTEC spread over the entire map. For about another two hours until 15:00 UT, the gradient becomes shallower than at 13:15 UT, but still with the Southeasterly gradient. Immediately at 15:15 UT, the gradient becomes steeper and half an hour later, takes on a Westerly gradient for 1.5 hours. At 17:30 UT, the gradient now rotates to a Northwesterly direction and for the next 3.5 hours becomes steeper and steeper, also to note that ΔTEC is negative across the whole map. At 21:00 UT, the gradient still has a Northwesterly direction and is becoming shallower, with the area of

negative ΔTEC getting smaller and shifting to the Southeast. The trend mentioned above continues for about two hours with the majority of the map containing positive ΔTEC values. At about 22:30 UT, the gradient becomes steeper and now rotates to a Northerly direction for the remainder of the 24 hour day.

#### 4.4.3.2 09 March 2008

There are differences and similarities between the second day of the 2008 Storm (09 March 2008) and the first day of the storm (08 March 2008) with regard to the spatiotemporal variation of ΔTEC across the map. It was noted that during the second day of the storm the gradients are steeper compared to the first day of the 2008 Storm. An increased factor of between 0.5-1.0 TECU for ΔTEC was experienced all over the map for the second day of the storm. It is noteworthy to note that the storm type is moderate for the second day of storm, compared to the first day of storm which experienced weak storm activity (See Figure 4.7). Gradients for the second day, compared to the first day were steeper at most times of the 24 hour day. These gradients followed the same directional pattern as compared to the first day. Lastly it was observed that the spread of the negative and positive ΔTEC values was consistent in space and time for day one and day two of the 2008 Storm.



#### 4.4.3.3 10 March 2008

The third and final day of the 2008 Storm (10 March 2008) experienced a similar pattern of gradient and ΔTEC over South Africa for the same times. It was also noted that the gradients for the last day of the storm were much steeper, compared to the gradients for the first two days of the storm, and also much shallow at certain times during the 24 hour day. The differences between the final day and the first two days of the storm is that the Dst index is in recovery phase, whereas the Dst index for the first day experienced weak activity, whereas the second day of the storm experienced moderate activity (See Figure 4.7). The ΔTEC increased by a factor of about 0.5-1.0 TECU, compared to ΔTEC for day one -and two of storm. For the three days of the storm at times of 02:15 UT, 04:30 UT (just after sunrise) and 09:30 UT, there were locations where ΔTEC was statistically negligible, in area of 5%, 10% and 15% of total map size, respectively.

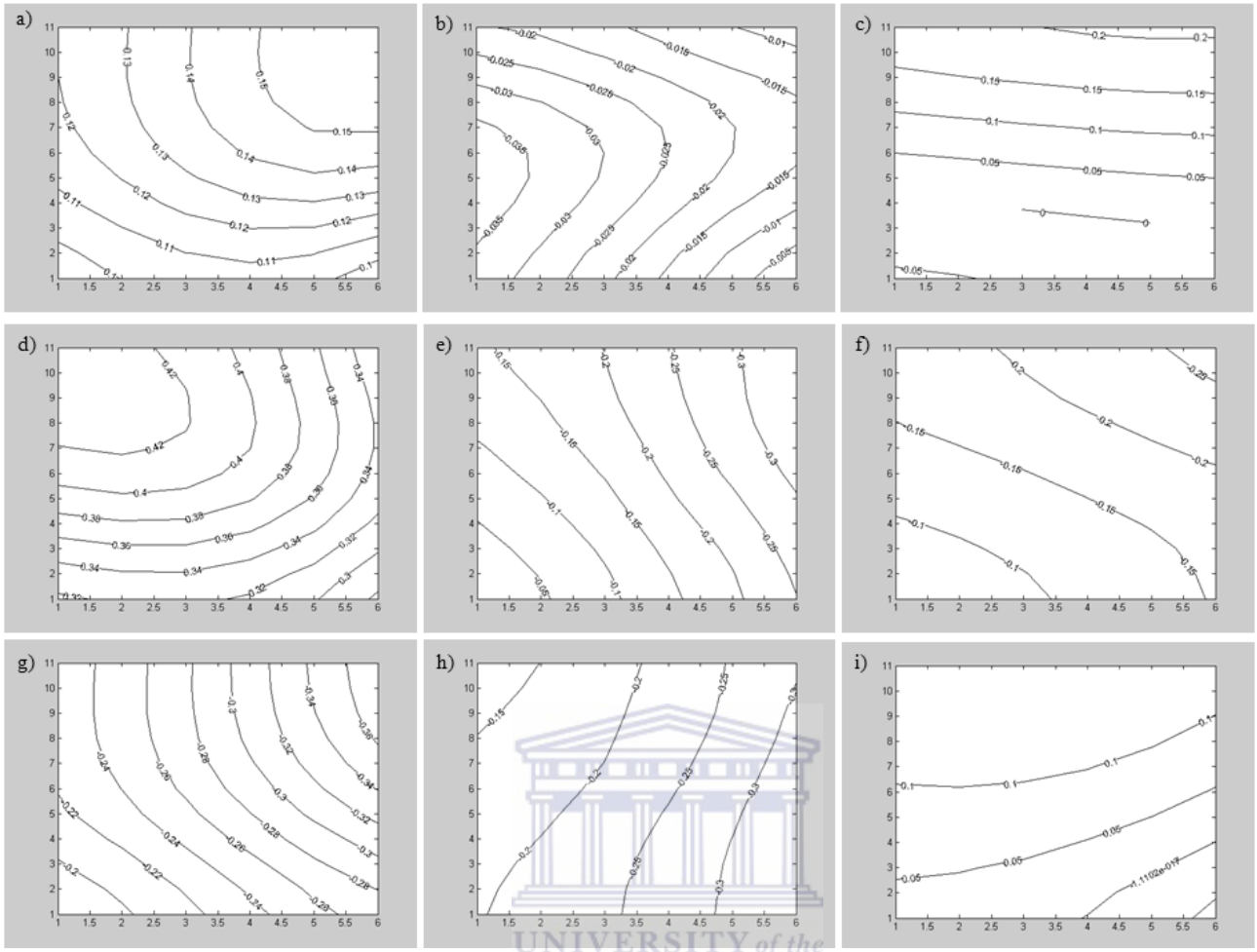


**Figure 4.17**: Contour plots of ΔTEC illustrating the variation of ΔTEC over South Africa during the 2008 Storm. All panels are for 08 March 2008. The times shown are in UT and are a) 00:00, b) 03:00, c) 04:45, d) 06:45, e) 10:45, f) 13:15, g) 15:15, h) 17:30, and i) 22:30.

Figure 4.17 is a visualization of how ΔTEC varies over South Africa with the gradients over a 24 hour day for 2008 Storm. Figure 4.18 is a graphical display illustrating the presence of a diurnal pattern for the average ΔTEC for the 2008 Storm. The diurnal pattern of the average ΔTEC follows the same trends at the typical Reference Day diurnal pattern, indicating that there is a strong modulation of the storm driven ΔTEC by the diurnal photoionization cycle, regardless of the level of storm activity.

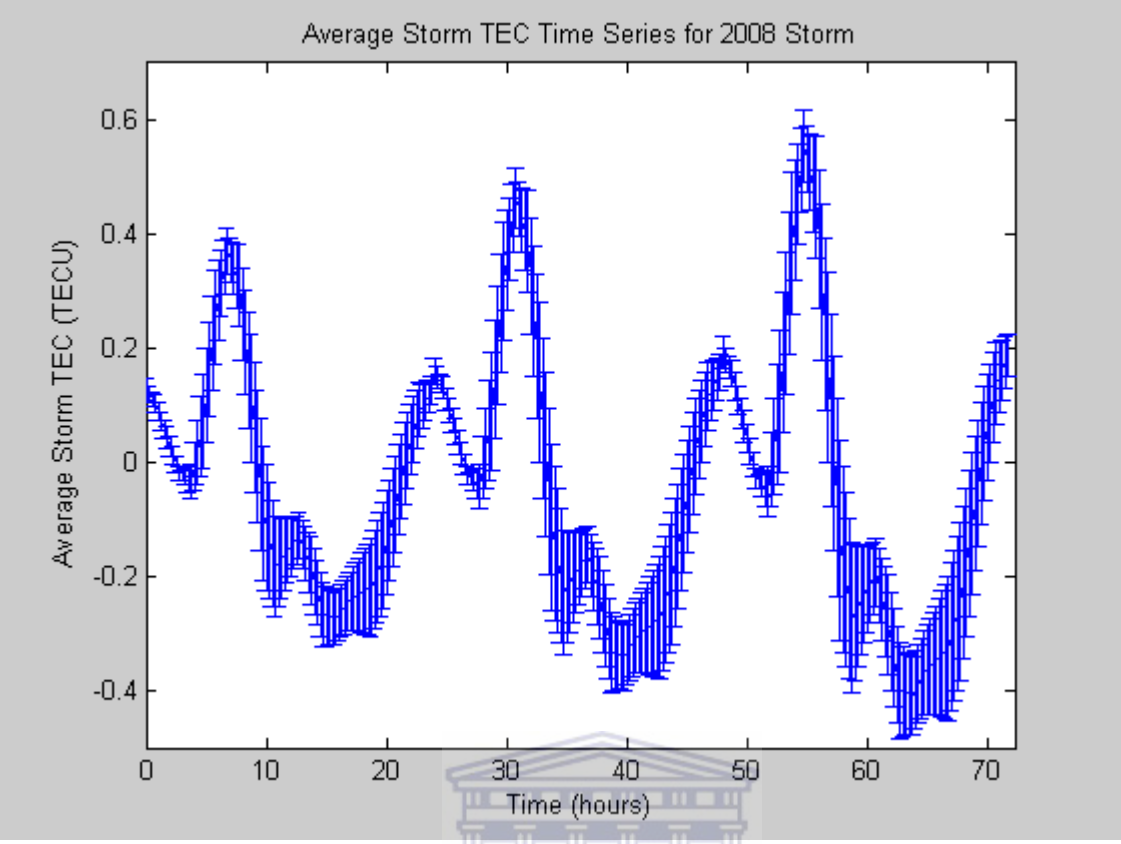


**Figure 4.18:** Graphical display showcasing the average Storm TEC Time Series for the 2008 Storm (08-10 March 2008), where the x label represents the time in hours from 00:00UT 08 March 2008. The average Storm TEC Time Series follows a modulated linear period. The average value is of the 66 values of TEC, where the error bars is the RMS deviation of the 66 values about the mean.



## 4.5 Comparisons between the Reference TEC Time Series

Comparing the three Reference Days (2003: Post Solar Maximum; 2008: Solar Minimum; and 2012: Post Solar Minimum), it was observed that all the three Reference Days follow essentially the same diurnal pattern. The magnitude of TEC density is dependent on numerous factors, for instance, the local time, the geographical location within the TEC study region, the season of the year (summer, autumn, winter, spring) and the solar activity cycle of the Sun (Jakowski, 1996; Jakowski, et al., 1999). The spatiotemporal maps portrayed in this thesis illustrated that RTEC is larger in the early afternoon than for other times a given Reference Day. This is expected due to the fact that during most of the day, the rate of production via photoionization is greater than the rate of recombination.

In the early hours of the three Reference Days, when the Sun has yet to rise, RTEC is relatively low, compared to RTEC during the early afternoon. This is due to the fact that during night time there is an absence of solar radiation and recombination dominates, producing lower RTEC densities. The spatiotemporal maps also portrays that during the morning (Figures 4.2a, 4.5a and 4.8a), the RTEC density values are greater at the Northeastern corner of the map, during the midday (Figures 4.2b, 4.5b and 4.8b), the location of greatest RTEC density values shifts towards the centre of the Northern edge of the map, and during the afternoon (Figures 4.2c, 4.5c and 4.8c), the RTEC density will shift to the Southwest corner of the map. During the evening, there is a long-term signature of the last location of insolation generated photoionization in the Northwest corner of the map which persists until the sun rises the next morning. Longitudinal dependences are connected to local time variations and thus for a set area, the intensity of the Sun's solar radiation increases as the Sun rises (TEC increases), peaks at about solar noon (TEC at maximum), and decreases as the Sun sets in the horizon (TEC decreases). The spatiotemporal maps from this work in general reveal these tendencies as described above and agree with the fact that the Sun's solar radiation (energy) is the chief contributor to the ionization of the ionosphere.

## 4.6 Comparisons between Storm Induced TEC Time Series

All three storms, namely the 2003 Storm, 2008 Storm and 2012 Storm that were extensively studied in this thesis experienced different magnitudes and patterns of geomagnetic activity for their respective storm periods. From the various Dst plots (See Figures 4.1, 4.4 and 4.7), we can see that the storm activity varied from weak to superstorm. It is observed that the response of ΔTEC to variations in magnetic activity, as indicated by the Dst index, is relatively immediate. Further, stronger magnetic storm activity leads to larger values of ΔTEC, although this connection is less strongly correlated.

It was also observed that for all three storms, there is solar cycle (as quantified by the sunspot number) dependence for both the magnetic storm activity (since for all three years, the storm that was studied was the largest storm of the year), and for the ΔTEC associated with that magnetic storm activity.




## 4.7 Summary

This chapter provided an in-depth discussion of the method of analysis, and of the observations, related to the investigation of the effect of mid-latitude magnetic storms on TEC over South Africa for Solar Cycle 23 and 24. We looked at TEC patterns over South Africa during Post Solar Maximum, Solar Minimum, and Post Solar Minimum periods as estimated by the MAGIC package, which was used as a primary research tool. It starts with what is being investigated and how it will be, as well as the description of the geomagnetic events chosen for this research study. It continues with the description of the pattern of Reference Day TEC Time Series and Storm TEC Time Series over South Africa during Post Solar Maximum, Solar Minimum, and Post Solar Minimum periods for years 2003, 2008 and 2012. In the conclusion, a comparison between the various Reference Day TEC Time Series and Storm TEC Time Series was made.

# Chapter 5

# SUMMARY, CONCLUSIONS, AND FUTURE WORK

## 5.1 Introduction

This final chapter of the thesis summarizes the main conclusions drawn from this research study as well as proposes possible future work using the MAGIC package as a research tool based on the outcome of this research study.

## 5.2 Summary and Conclusions



The main aim of this thesis was to investigate the effect of mid-latitude magnetic storms on TEC over South Africa for portions of Solar Cycles 23 and 24. For this purpose, the MAGIC package was used as a primary research tool, which converts GPS data (available from Trignet Network) into maps of TEC. Subsequently, the ionospheric TEC maps which show the spatiotemporal representations of TEC over South Africa were analyzed during Post Solar Maximum, Solar Minimum, and Post Solar Minimum periods, using the greatest storm from the years 2003, 2008 and 2012, respectively. The results of the analysis in this research study showed some definite trends and patterns for the Reference Day Time Series and Storm Time Series, namely:

1) All three Reference Days (2003: Post Solar Maximum; 2008: Solar Minimum; and 2012: Post Solar Minimum) follow the same general diurnal pattern, namely, photoionization driven by solar insolation during local day, followed by recombination during the local nighttime period when there is no illumination. The magnitude of RTEC shows dependence on the phase of the solar cycle (specifically, the Wolf sunspot number), with greater values of maximum RTEC when the sunspot is higher, and lower values of maximum RTEC when the sunspot is lower.

2) It was inferred from the spatiotemporal maps, that RTEC showed larger values in the early afternoon than for other times during a given Reference Day, as expected since during the day, the rate of production via photoionization is greater than the rate of recombination.
3) A few hours after solar midnight for the three Reference Days, when the Sun is yet to rise, RTEC was observed to be relatively low, compared to RTEC during the early afternoon, as expected. The latter is caused by the absence of solar radiation during night time, where recombination dominates, hence lower RTEC.
4) It was inferred from the spatiotemporal maps that during the morning, the RTEC are greater at the Northeastern corner of the map, shifting to the Southwest of the map as the day advances, tracking the subsolar point which has the least zenith angle and consequently the greatest contribution towards photoionization.
5) It was inferred from the spatiotemporal maps that during the evening, RTEC is highest at the Northwest corner of the map, due to the fact that there is a long-term signature of the last location of insolation generated photoionization in the Northwest corner of the map which persists until the sun rises the next morning.
6) Using the Dst index, storm time periods were selected. For the Storm Time Series off all three storms (2003 Storm, 2008 Storm, and 2012 Storm) used in this research study, different magnitudes and patterns of geomagnetic activity were present. In particular, the 2003 Storm (Post Solar Maximum) was much stronger than the 2008 Storm (Solar Minimum). We observed that the response of ΔTEC to the variations in the magnetic activity as indicated by the Dst index is moderately immediate. It was noted that the strong magnetic activity leads to greater ΔTEC, even though this connection is not as strongly correlated.
7) It was observed that even during the most intense magnetic storm, the associated differential electron concentration (ΔTEC) is a small fraction – no more than a few percent – of the background electron concentration (RTEC). This has important ramifications for applications where it is important to correct for the effect of the ionosphere on signal propagation, since a standard TEC model based on day of year, local time of day, and latitude will account for virtually all of the effect.
8) In addition, all three storms showed a solar cycle (quantified by the sunspot number) dependence for both magnetic storm activity (since for all three years, the storm that was studied was the largest storm of the year), and for ΔTEC associated with that

magnetic storm activity. It is presumed that ΔTEC follows from the magnetic storm activity, rather than directly from the solar activity.

To conclude, this research study adds to the understanding of solar cycle variations of South Africa's ionosphere, and will be valuable for future local and international space weather studies.

## 5.3 Proposed Future Work

For proposed future work using the MAGIC package as an applied research tool, the following topics can be addressed;

a) Expansion of the MAGIC model over Africa, when the GNSS capacity increases over Africa in the near future.
b) Investigating the effect of geomagnetic storms over South Africa and Africa for Solar Cycle 24 and subsequent solar cycles.
c) Comparison of the MAGIC package versus other local ionospheric TEC models.

# REFERENCES

Ahrens, C.D. Essentials of Meteorology: An Invitation to the Atmosphere. Brooks/Cole/Thomson Learning, United States of America, 2008.

Appleton, E.V., Barnett, M.A.F. On Some Direct Evidence for Downward Atmospheric Reflection of Electric Rays. The Royal Society., 109, 621-641, 1925.

Appleton, E.V., Barnett, M.A.F. On Wireless Interference Phenomena between Ground Waves and Waves Deviated by the Upper Atmosphere. The Royal Society., 113, 450-458, 1926.

Araujo-Pradere, E.A., Fuller-Rowell, T.J., Spencer, P.S.J. Consistent features of TEC changes during ionospheric storms. J. Atmos. Sol-Terr. Phy., 68, 1834-1842, 2006.

Araujo-Pradere, E.A., Fuller-Rowell, T.J., Spencer, P.S.J., Minter, C.F. Differential validation of the US-TEC model. Radio Sci., 42, RS3016, doi:10.1029/2006RS003459, 2007.



Bartels, J., Heck, N.H., Johnston, H.F. The three-hour-range index measuring geomagnetic activity. J. Geophys. Res., 44, 411, 1939.

Bassiri, S., Hajj, G. A. Higher order ionospheric effects on the Global Positioning System observables and means of modeling them. Manuscripta geodaetica, 18, 280-289, 1993.

Basu, Su., Basu, S., Makela, J.J., Sheehan, R.E., MacKenzie, E., Doherty, P., Wright, J.W., Keskinen, M.J., Pallamraju, D., Paxton, L.J., Berkey, F.T. Two components of ionospheric plasma structuring at midlatitudes observed during the large magnetic storm of October 30, 2003. Geophys. Res. Lett, 32, L12S06, doi:10.1029/2004GL021669, 2005.

Becker-Guedes, F., Sahai, Y., Fagundes, P.R., Espinoza, E.S., Pillat, V.G., Lima, W.L.C., Basu, Su., Basu, Sa., Otsuka, Y., Shiokawa, K., MacKenzie, E.M., Pi, X., Bittencourt, J.A. The ionospheric response in the Brazilian sector during the super geomagnetic storm on 20 November 2003. Ann.Geophys., 25, 863-873, 2007.

Biermann, L. The solar wind and the interplanetary media. In Space Astrophys., edited by W. Liller, McGrawHill, NewYork, pp.150, 1961.

Bilitza, D. The E- and D-region in IRI. Adv. Space Res., 21, 871-874, 1998.

Brunner, F.K., Gu, M. An improved model for the dual frequency ionospheric correction of GPS observations, Manuscripta Geodaetica, 16, 205-214, 1991.

Breit, G., Tuve, M.A. A Test of the Existence of the Conducting Layer. Phys. Rev., 28, 554-575, 1926.

Brekke, A. Physics of the Upper Polar Atmosphere. John Wiley & Sons Ltd, New York, 1997.

Budden, K.G. The propagation of radio waves: The theory of radio waves of low power in the ionosphere and magnetosphere. Cambridge University Press, 1985.

Cravens, T.E. Physics of solar system plasmas. Cambridge University Press, Cambridge, 1997.

Cilliers, P.J., Opperman, B.D.L., Mitchell, C.N., Spencer, P.J. Electron density profiles determined from tomographic reconstruction of total electron content obtained from GPS dual frequency data: first results from South African network of dual frequency GPS receiver stations. Adv. Space Res., 34, 2049-2055, 2004.

Combrink, A.Z.A., Combrinck, W.L., Moraal, H. Near real-time detection of atmospheric water vapour using SADC GPS network. S. Afr. J. Sci., 100, 436-442, 2004.

Combrink, A.Z.A. Sensing atmospheric water vapour using the Global Positioning System. Ph. D. Thesis, University of Cape Town, South Africa, pp1-127, 2006.

Davies, K. Recent progress in Satellite Radio Beacon Studies with particular emphasis on the ATS-6 Radio Beacon Experiment. Space Sci. Rev., 25, 357-430, 1980.

Davies, K. Ionospheric Radio. Peter Peregrinus Ltd, London (UK), 1990.

El-Rabbany, A. Introduction to GPS: The Global Positioning System. Artech House, Inc, United States of America, 2002.

Fedrizzi, M., Langley, R.B., Komjathy, A., Santos, M.C., de Paula, E.R., Kantor, I.J. The low-latitude Ionosphere: Monitoring its behaviour with GPS. Institute of Navigation. Proceedings of ION GPS-2001, Salt lake City, 2468-2475, 2001.

Fedrizzi, M., de Paula, E.R., Kantor, I. J., Langley, R.B., Komjathy, A., Batista, I. S. Study of the March 31, 2001 magnetic storm effects on the ionospheric GPS data. Adv. Space Res., 36, 534-545, 2005.

Fernández, M.G. Contributions to the 3D ionospheric sounding with GPS data. Ph.D. Thesis, Universitat Politècnica de Catalunya, Spain, pp 1-58, 2004.

Fourie, C.S.J., Combrinck, L., Croukamp, L., Saunders, I. A Proposed Space Geodesy Observatory Near Matjiesfontein: A Geotechnical Site Investigation. Proceedings of the 5th Inkaba yeAfrica Workshop, Wild Coast Sun, KZN, South Africa, 22-23 October 2007.

Fremouw, E.J., Secan, J.A., Howe, B.M. Application of stochastic inverse theory to ionospheric tomography. Radio Sci., 27, 721-732, 1992.

Fremouw, E.J., Secan, J.A., Bussey, R.M., Howe, B.M. A Status Report on Applying Discrete Inverse Theory to Ionospheric Tomogrpahy. Int. J. Imag. Syst. Tech., 5, 97-105, 1994.

Fuller-Rowell, T. USTEC: a new product from the Space Environment Center characterizing the ionospheric total electron content. GPS Solut., 9, 236-239, 2005.

Gao, Y., Liu, Z.Z. Precise ionosphere modelling using regional GPS Network data. J. of GPS., 1, 18-24, 2002.

Garriot, O.K., Little, C.G. The use of Geostationary Satellites for the study of Ionospheric Electron Content and Radio-Wave Propagation. J. Geophys. Res., 65, 2025, 1960.

Garriot, O.K., Smith, F.L., Yuen, P.C. Observations of ionospheric electron content using a geo stationary satellite. Plan. Space Sci., 13, 829, 1965.

Gillies, R.G. Modelling of Transionospheric HF Radio Wave Propagation for the ISIS II and Epop Satellites. Ms.C. Thesis, University of Saskatchewan, Canada, pp 1-126, 2006.

Goodman, J.M. Space Weather & Telecommunications. Springer Science + Business Media, Inc, New York, 2005.

Gleeson, S. and Gebre-Egziabher, D. GNSS Applications and Methods. Artech House, Inc, United States of America, 2009.

Habarulema, J.B., McKinnell, L.A., Cilliers, P.J. Prediction of global positioning system total electron content using Neural Networks over South Africa. J. Atmos. Sol-Terr. Phy., 69, 1842-1850, 2007.



Habarulema, J.B., McKinnell, L.A., Opperman, B.D.L. Towards a GPS-based TEC prediction model for Southern Africa with feed forward networks. Adv. Space Res., 44, 82-92, 2009 (a).

Habarulema, J.B., McKinnell, L.A., Cilliers, P.J., Opperman, B.D.L. Application of neural networks to South African GPS TEC modelling. Adv. Space Res., 43, 1777-1720, 2009 (b).

Habarulema, J.B. A contribution to TEC modeling over Southern Africa using GPS data. Ph.D. Thesis, Rhodes University, South Africa, pp 1-151, 2010.

Hansen, A.J., Walter, T., Enge, P. Ionospheric Correction Using Tomography. Proceedings of the ION GPS-97, Nashville Tennessee, United States of America, pp. A3-A5, 15-18 September 1997.

Hansen, A.J. Real-time Ionospheric Tomography Using Terrestrial GPS Sensors. Proceedings of the ION GPS-98, Kansas City, United States of America, pp. 249-257, September 1998.

Hanslmeier, A. The Sun and Space Weather. Springer, The Netherlands, 2007.

Hernández-Pajares, M., Juan, J.M., Sanz, J. Application of ionospheric tomography to real-time GPS carrier-phase ambiguities resolution, at scales of 400-1000 km and with high geomagnetic activity. Geophys. Res. Lett., 27, 2009-2012, 2000.

Hewitt, F.J., Hewitt, J., Wadley, T.L. A frequency prediction service for South Africa, Trans. SAIEE, 38, 180-197, July 1947.

Howe, B.M., Runciman, K., Seca, J.A. Tomography of the ionosphere: Four-dimensional simulations. Radio Sci., 33, 109-128, 1998.

Hunsucker, R.D. and Hargreaves, J.K. The high-latitude ionosphere and its effects on radio propagation. Cambridge University Press, New York, 2003.



Jakowski, N. TEC monitoring by Using Satellite Positioning Systems. in: Kohl, H., Rüster, R., Schlegel, K. (Eds.), Modern Ionospheric Science. Max-Planck-Intitut für Aeronomie, 371-390, 1996.

Jakowski, N., Schlüter, S., Sardón, E. Total electron content of the ionosphere during the geomagnetic storm on 10 January 1997. J. Atmos. Sol. Terr. Phys., 61, 299-307, 1999.

Jakowski, N., Heise, S., Wehrenpfenning, S., Schlüter, S. TEC Monitoring by GPS-A possible contribution to space weather monitoring. Phys. Chem. Earth (C), 26, 609-613, 2001.

Jakowski, N., Heise, S., Wehrenpfenning, S., Schlüter, S., Reimer, R. GPS/GLONASS-based TEC measurements as a contributor for space weather forecast. J. Atmos. and Sol. Terr. Phys., 64, 729-735, 2002.

Kalman, R.E. A New Approach to Linear Filtering and Prediction Problems. Transaction of the ASME-Journal of Basic Engineering, 82 (Series D), 35-45, 1960.

Kelly, M.C. The Earth's Ionosphere Plasma Physics & Electrodynamics. Elsevier, United States of America, 2009.

Klobuchar, J.A. Ionospheric effects on GPS. GPS World, 2, 48-51, 1991.

Kitner, P.M. GPS and ionospheric scintillations. Space Weather., 5, 2007.

Knight, M.F. Ionospheric Scintillation Effects on Global Positioning System Receivers. Ph.D. Thesis, The University of Adelaide, South Australia, pp 1-336, 2000.

Komjathy, A., Langley, R.B. An assessment of predicted and measured ionospheric total electron content using a regional GPS Network. The proceedings of the National Technical Meeting of the Institute of Navigation., pp. 615-624, 1996.

Komjathy, A. Global Ionospheric Total Electron Content Mapping using the Global Positioning System. Ph.D. Thesis, University of New Brunswick, Canada, pp 1-265, 1997.

Lang, K.R. The Sun from Space. Springer-Verlag Berlin Heidelberg, 2009.

Langley, R.B. Propagation of GPS signals. In GPS for Geodesy. International School, Delft, The Netherland, 26 March-1 April, 1995, Springerverlag, NewYork, 1996.

Manju, G., Kumar Pant, T., Ravindran, S., Sridharan, R. On the response of the equatorial and low latitude ionospheric regions in the Indian sector to the large magnetic disturbance of 29 October 2003. Ann.Geophys., 27, 2539-2544, 2009.

Mannucci, A.J., Wilson, B.D., Edwards, C.D. A new method for monitoring the Earth's Ionospheric total electron content using the GPS global network. Proceedings of the ION GPS-93, 6th International Technical Meeting of the Satellite division of the Institute of Navigation, Salt Lake, Utah, United States of America, VII, 1323-1332, 1993.

Mannucci, A.J., Wilson, B.D., Yuan, D.N., Ho, C.M., Lindqwister, U.J., Runge, T.F.A global mapping Technique for GPS-derived ionospheric total electron content measurements, Radio Sci., 33, 565-582, 1998.

Mannucci, A.J., Tsurutani, B.T., Iijima, B.A., Komjathy, A., Saito, A., Gonzalez, W.D., Guarnieri, F.L., Kozyra, J.U., Skoug, R. Dayside global ionospheric response to the major interplanetary events of October 29-30, 2003 ‘‘Halloween Storms’’. Geophys. Res. Lett, 32, L12S02, doi:10.1029/2004GL021467, 2005.

McKinnell, L.A., Poole, A.V.W. The development of a neural network based short-term foF2 forecast program. Phys. Chem. Earth, 24, 287-290, 2000.

McKinnell, L.A., Poole, A.V.W. Neural Network-based ionospheric modelling over the South African region, S. Afr. J. Sci., 100, 519-523, 2004.

McKinnell, L.A., Opperman, B., Cilliers, P.J. GPS TEC and Ionosonde TEC over Grahamstown, South Africa: First Comparisons. Adv. Space Res., 39, 816-820, 2007.



McNamara, L.F. The ionosphere Communications, Surveillance, and Direction Finding. Krieger Publishing Company, Malabar, FL, 1991.

McNamara, L.F. Radio amateur guide to the ionosphere. Krieger publishing Company, Malabar, FL, 1994.

Meggs, R.W., Mitchel, C.N., Spencer, S.J. A comparison of techniques for mapping total electron content over Europe using GPS signal. Radio Sci., 39, RS1S10, doi:10.1079/2002RS002846, 2004.

Mendizabal, J., Berenguer, R., Melendez, J. GPS and Galileo: Dual RF Front-end Receiver Design, Fabrication, and Test. McGraw-Hill, 2009.

Minter, C.F. Robertson, D.S., Spencer P.S.J., Jacobson, A.R., Fuller-Rowell, T.J., Araujo-Pradere, E.A., Moses R.W. A Comparison of MAGIC and FORTE Ionosphere Measurements. Radio Sci., 42, RS3026, doi:10.1029/2006RS003460, 2007.

Mitchell, C.N., Kersley, L., Heaton, J.A.T., Pryse, S.E. Determination of the vertical electron density profile in ionospheric tomography: experimental results. Ann. Geophys., 15, 747-752, 1997.

Mitchell, C.N., Spencer, P.S.J. A three-dimensional time-dependent algorithm for ionospheric imaging using GPS. Ann. Geophys., 46, 687-696, 2003.

Moeketsi, D.M. Solar Cycle Effects on GNSS-Derived Ionospheric Total Electron Content Observed over Southern Africa. Ph.D. Thesis, Rhodes University, South Africa, pp 1-141, 2007 (a).

Moeketsi, D.M., Combrinck, W.L., McKinnell, L.A., Combrink, A.Z.A. Comparison of ionospheric Total Electron Content derived from collocated GNSS receivers over HartRAO during Solar X-ray flares. S. Afr. J. Geol., 110, 219-224, 2007 (b).

Moeketsi, D.M., Combrinck, W.L., McKinnell, L.A., Fedrizzi, M. Mapping GPS derived ionospheric Total Electron Content over Southern Africa during different epochs of Solar Cycle 23. Adv. Space Res., 39, 821-829, 2007 (c).

Moldwin, M. An Introduction to Space Weather. Cambridge University Press, New York, 2008.

Nava, B., Coïsson, P., Radicella, S.M. A new version of the NeQuick ionosphere electron density model. J. Atmos. Sol-Terr. Phy., 70, 1856-1862, 2008.

Ngcobo, S., Moeketsi, D. M., Combrink, A.Z.A., Combrinck, W.L. Ionospheric total electron Content observed using the southern African GPS networks. S. Afr. J. Sci., 101, 537-539, 2005.

Okoh, D.I. Developing an Ionospheric Map for South Africa. Ms.C. Thesis, Rhodes University, South Africa, pp 1-74, 2009.

Opperman, B.D.L., Cilliers, P.J., McKinnel, L.A., Haggard, R. Development of a regional GPS-based ionospheric TEC model for South Africa. Adv. Space Res., 39, 808-815, 2007 (a).

Opperman, B.D.L. Reconstructing Ionospheric TEC over South Africa using signals from a regional GPS network. Ph.D. Thesis, Rhodes University, South Africa, pp 1-179, 2007 (b).

Otto, A. The Magnetosphere. Lect. Notes., Springer Verlag, Berlin, Heidenberg, (Edited by K. Scherer, H. Fichtner, B. Heber, U. Mall: Space Weather, The Physics behind the slogan), 656, 133-192, 2005.

Oyeyemi, E., Poole, A.W.V. On the development of a global foF2 empirical model using neural networks. Adv. Space Res., 34, 1966-1972, 2004.

Oyeyemi, E.O. A global ionospheric F2 region peak electron density model using neural networks and extended geophysically relevant inputs. PhD thesis, Rhodes University, South Africa, pp. 1-183, 2005.

Oyeyemi, E.O., McKinnell, L.A., Poole, A.W.V. Neural network-based prediction techniques for global modeling of M(3000) F2 ionospheric parameter. Adv. Space Res., 39, 643-650, 2007.

Parker, E. N. Cosmic ray modulation by the solar wind. Phys. Rev., 110, 1445, 1958.

Parker, E. N. Interplanetary dynamical processes, Interscience, NewYork, 1963.

Pirog, O.M., Polekh, N.M., Voeykov, S.V., Zherebtsov, G.A., Tatarinov, P.V. Ionospheric disturbances in the East-Asian region during geomagnetic storm in November, 2004. Adv. Space Res., 39, 1335-1341, 2007.

Parks, G.K. Physics of space plasmas: An Introduction. Westview Press, Boulder, CO, 2004.

Prasad, R. and Ruggieri, M. Applied Satellite Navigation using GPS, GALILEO and Augmentation Systems. Artech House, Inc, United States of America, 2005.

Ratcliffe, J.A. Magneto-ionic theory and its application to the ionosphere. Cambridge University Press, Cambridge, 1959.

Ratcliffe, J.A. An introduction to the ionosphere and magnetosphere. Cambridge University Press, London, 1972.

Ratcliffe, J.A. The early days of ionospheric research: The early ionosphere investigations by Appleton and his colleagues. Phil. Trans. R. Soc. London. A., 280, 3-9, 1975.\

Rawer, K. and Suchy, K. Remarks concerning the dispersion equation of electromagnetic waves in a magnetized cold plasma, J. Atmos. Terr. Phys, 38, 395-398, 1976.

Rostoker, G. Geomagnetic indices. Rev. Geophys., 10, 935-950, 1972.

Schaer, S. Mapping and predicting the Earth's ionosphere using the global positioning system. Ph.D. Thesis, University of Bern, Bern, Switzerland, 1999.

Schunk, R.W., Scherliess, L., Sojka, J.J., Thompson, D.C. Global Assimilation of Ionospheric Measurements (GAIM). Proceedings of 2002 Ionospheric Effects Symposium. Ed. J.M. Goodman, JMG Associates, Alexandria, VA, 2002.

Schunk, R.W., Scherliess, L., Sojka, J.J., Thompson, D.C., Zhu, L. An Operational Data Assimilation Model of the Global Ionosphere. In: Proceedings of 2005 Ionospheric Effects Symposium. Ed. J.M. Goodman, JMG Associates, Alexandria, VA, 2005.

Schunk, R.W., et al. Global Assimilation of Ionospheric Measurements (GAIM), Radio Sci., 39, RS1S02, doi:10.1029/2002RS002794, 2004.

Schunk, R.W. and Nagy, A.F. Ionospheres Physics, Plasma Physics and Chemistry. Cambridge University Press, New York, 2009.

Skone, S., de Jong, M. The impact of geomagnetic substorms on GPS receiver performance. Earth Planets Space, 52, 1067-1071, 2000.

Skone, S., Knudsen, K., de Jong, M. Limitations in GPS Receiver Tracking Performance Under Ionospheric Scintillation Conditions. Phys. Chem. Earth (A), 26, 613-621, 2001.

Spencer, P.S.J., Robertson, D.S., Mader, G.L. Ionospheric data assimilation methods for geodetic applications. Paper presented at IEEE PLANS 2004, Inst. Of Electron. And Electr. Eng., Montery, Calif., 510-517, 26-29 Apr. 2004.

Tascione, T.F. Introduction to Space Enviroment. Orbit Book Company, Malibar, Florida, 1988.

Titheridge, J.E. The electron content of the southern mid-latitude ionosphere: 1965-1971, J. Atmos. Terr. Phys., 35, 981, 1973.

Tsai, L.C., Liu, C.H., Tsai, W.H., Liu, C.T. Tomographic imaging of the ionosphere using the GPS/MET and NNSS data. J. Atmos. Sol-Terr. Phy., 64, 2003-2011, 2002.

Tsurutani, B.T., Judge, D.L., Guarnieri, F.L., Gangopadhyay, P., Jones, A.R., Nuttall, J., Zambon, G.A., Didkovsky, L. , Mannucci, A.J., Iijima, B., Meier, R.R., Immel, T.J., Woods, T.N., Prasad, S., Floyd, L., Huba, J., Solomon, S.C., Straus, P., Viereck, R. The October 28, 2003 extreme EUV solar flare and resultant extreme ionospheric effects: Comparison to other Halloween events and the Bastille Day event. Geophys. Res. Lett, 32, L03S09, doi:10.1029/2004GL021475, 2005.

Uwamahoro, J. An analysis of sources and prendictability of geomagnetic storms. Ph.D. Thesis, Rhodes University, South Africa, pp 1-132, 2011.

Vita-Finzi, C. The Sun A User's Manual. Springer Science + Business Media B.V., London (UK), 2008.

Wadley, T.L. A single-band 0-20-Mc/s ionosphere recorder embodying some new techniques, Proc. Instn. Elect. Engrs., Pt. III, 96, 483-486. 1949.

Walker, J.K. Spherical cap harmonic modelling of high latitude magnetic activity and equivalent sources with sparse observations. J. Atmos. Terr. Phys., 51 (2), 67-80, 1989.

Wernik, A.W. Scintillation modelling using in situ data. Radio Sci., 42, 2007.

Wernik, A.W., Alfonsi, L., Materassi, M. Scintillation modeling using in situ data. Radio Sci., 42, RS1002, doi:10.1029/2006RS003512, 2007.

Xu, G. GPS Theory, Algorithms and Applications. Springer-Verlag Berlin Heidelberg, New York, 2007.

Yizengaw, E., Dyson, P.L., Essex, E.A., Moldwin, M.B. Ionosphere dynamics over the Southern Hemisphere during the 31 March 2001 severe magnetic storm using multi-instrument measurement data. Ann. Geophys., 23, 707-721, 2005.

Yizengaw, E., Moldwin, M.B., Komjathy, A., Mannucci, A.J. Unusual topside ionospheric density response to the November 2003 superstorm. J.Geophys.Res., 111, A02308, doi:10.1029/2005JA011433, 2006.

Zhang, J., Richardson, I.G., Webb, D.F., Gopalswamy, N., Huttunen, E., Kasper, J.C., Nitta, N.V., Poomvises, W., Thompson, B. J., Wu, C.C., Yashiro, S. and Zhukov, A.N., Solar and interplanetary sources of major geomagnetic storms (Dst $\leq -50$ nT) during 1996-2005. J.Geophys.Res., 112(A10102), 2007.

Zogg, J.M. (2002, March 26). GPS Basics Introduction to the System Application Overview. Retrieved June 28, 2011, from http://faculty.ksu.edu.sa/hbilani/SE412books/GPS_basics_u_blox_en.pdf